MODELING HUMAN BRAIN DEVLEOPMENT AND DISEASES USING HUMAN INDUCED-PLURIPOTENT STEM CELL-DERIVED ORGANOIDS

by

XUYU QIAN

A dissertation submitted to Johns Hopkins University
In conformity with the requirements for the degree of Doctor of Philosophy

Baltimore, Maryland

December 2019

Abstract

Brain organoids, three-dimensional cultures that model organogenesis, provide a new platform to investigate brain development. High cost, variability and heterogeneity currently limit the broad application of existing brain organoid technologies. My thesis work focuses on developing methods to generate forebrain organoids from human induced pluripotent stem cells (hiPSCs) using a custom-designed spinning bioreactor. Forebrain organoids recapitulate key features of human cortical development, including progenitor zone organization, neurogenesis, gene expression, and, notably, a well-defined outer radial glial cell (RGCs) layer resembling the human outer subventricular zone.

An immediate application for brain organoids is to address the global health emergency of Zika virus (ZIKV)-induced microcephaly. Exposure of ZIKV to forebrain organoids revealed preferential, productive infection of RGCs. ZIKV infection leads to increased cell death and reduced proliferation, resulting in decreased neuronal cell layer volume and reduced overall organoid size, resembling microcephaly. Our forebrain organoids and SpinΩ bioreactor provide an accessible and versatile platform for modeling human brain development and disease, and for compound testing, including potential ZIKV antiviral drugs. Results from our ZIKV experiments reveal cellular mechanisms of ZIKV-induced microcephaly and have implications for therapeutic development.

Another limitation of current organoid methods is interior hypoxia and cell death due to insufficient surface diffusion, preventing generation of architecture representative of late developmental stages. In order to generate more mature organoids, we developed the sliced neocortical organoid (SNO) method, which bypasses the diffusion limit to prevent cell death over long-term cultures. This method leads to sustains neurogenesis and formation of an expanded cortical plate that establishes distinct upper and deep cortical layers for neurons and astrocytes, resembling the third-trimester embryonic human neocortex. Using the SNO system, we further identify a critical role of WNT/β-Catenin signaling in regulating cortical neuron fate specification, which is disrupted by a psychiatric disorder-associated genetic mutation in patient iPSC-derived SNOs. These results demonstrate the utility of SNOs as a model for investigating previously inaccessible human-specific late-stage cortical development and disease-relevant mechanisms.

Together, my work has tremendously advanced brain organoid technologies, and provided a novel platform to elucidate the underlying mechanisms and potential therapeutic strategies for neurodevelopmental diseases.

Ph.D. Dissertation Referees

Hongjun Song, Ph.D. (Faculty Sponsor): Perelman Professor, Department of Neuroscience, University of Pennsylvania; Adjunct Professor, Department of Neuroscience, the Johns Hopkins University, School of Medicine

Ulrich Mueller, Ph.D.: Bloomberg Distinguished Professor, Department of Neuroscience, the Johns Hopkins University, School of Medicine

Dedication

This thesis is dedicated to my parents,

Wei Qian and Ming Xu,

who brought me to this world and taught me what is most precious in life.

Preface

First, I thank my parents, Wei Qian and Ming Xu, for their unyielding love and trust. I cannot imagine accomplishing anything without them at my back. Ever since I was a kid, they have always given me the liberty to choose my own path. They taught me I am born free, and I am born unique. Therefore, I've decided that the meaning of my life can only be fulfilled by the pursuit of freedom for all humanity. As one aspect of this pursuit, the biomedical research that I conduct is ultimately aimed at unshackling humanity from the fear of disease and death.

I am grateful to my mentor, Prof. Hongjun Song, for his legendary guidance and mentorship. His dedication in creating a lab environment for every member to succeed is admirable. Hongjun is my role model and constantly inspires me with the qualities and skillsets that I need to become a righteous and productive scientist. His insatiable passion for discoveries and drive for accomplishments urges me to never be contented with what I have achieved. His mystic sixth-sense for what is the next big question to pursue compels me to never stop thinking, even in my sleep. He is not only a giant whose shoulder I stand on, but also a mountain that I aspire to surpass. I also thank Prof. Guo-Li Ming, whose partnership with Hongjun is indispensable to the success of my thesis project. Guo-Li is in every aspect as brilliant as Hongjun and is a champion for equality and diversity in scientific community. Together, Hongjun and Guo-Li also taught me how to achieve balance between a lovely family and devotion in science.

Many lab members have offered tremendous help throughout my PhD. First, I thank Ha Nam Nguyen, a big brother who taught me not only countless knowledge and techniques, but also scientific rigid, integrity and responsibility. I also thank Fadi Jacob and Ce Zhang as my great buddies in the organoid group. I thank collaborators both inside and outside the Ming-Song lab that have contributed to my thesis project, Mingxi M Song, Christopher Hadiono, Sarah C Ogden, Christy Hammack, Bing Yao, Gregory R Hamersky, Chun Zhong, Ki-jun Yoon, William Jeang, Li Lin, Yujing Li, Jai Thakor, Daniel A Berg, Eunchai Kang, David Nauen, Zhexing Wen, Kimberly M Christian, Pei-Yong Shi, Brady J Maher, Hao Wu, Peng Jin, Hengli Tang, Yijing Su, Christopher D. Adam, Andre U. Deutschmann, Sarshan R. Pather, Ethan M. Goldberg, Kenong Su, Shiying Li, Lu Lu, Phuong Nguyen, Christopher Pierce, Lisa A. Briand, H. Issac Chen, and John A. Wolf.

I also thank my thesis committee, Professors Alex Kolodkin, Feilim Mac Gabhann, Hai-Quan Mao and Ulrich Mueller for providing helpful feedback on my projects and supporting me in the back throughout my graduate career. I am very grateful for the Biomedical Engineering PhD program at Johns Hopkins, for giving me the dream-come-true opportunity to come to Johns Hopkins University School of Medicine, the birthplace of many legends.

I would also like to take the opportunity to appreciate my previous research mentors. Prof. Qi Wen at Worcester Polytechnic Institute was the first person to introduce me to scientific research and gave me the incredible opportunity to work independently on my own project as an undergraduate volunteer. Prof. Douglas Robinson and his postdoc Tianzhi Luo mentored me for my first lab rotation, which opened my eyes to cutting-edge scientific research that I hadn't experienced in undergraduate time. The late Prof. David Yue mentored me for my second lab rotation. His genuine passion in science remains an inspiration for me. I remember the conversation we had one evening after he sat down with me for 2 hours to analyze my live-cell imaging data - "You may learn to enjoy this even if the experiment is not working". Yes, I have learned to enjoy science, rain or shine.

I also want to thank my dear friends since middle school and high school, Zhiyang Lu, Zhongrun Zhu, Zijin Zhang, Hantian Gao, Siyuan Chen, Huang Huang, Peichong Shen, Yue Chang, and many others, with whom I play online video games, chat about anime and send meme pictures. Although we are physically spread all around the globe, our connections via the internet always make me feel at home.

Lastly, I would like to thank Director Anno Hideaki, who created the anime series *Neon Genesis Evangelion* and *The Rebuild of Evangelion*. I have never met Director Hideaki personally and I doubt if he would ever see what I wrote, but his work has the most profound impact on my career choice and view of life. The story of *Evangelion* is set in a post-apocalyptic world, where humanity's last hope for salvation from certain extinction resides in "Eva" units, giant robot-like humanoids created by bioengineering. It was when I first watched *Evangelion* that I realized biology and biotechnology have the power to reshape the world, which has led to my career choice. Within a mind-boggling Sci-Fi world are the characters that in drastic contrast are depicted so real and relatable. Shinji Ikari, the main protagonist of the series, seldom acts like a "hero" in fiction. When his hands are shaky and eyes filled with fear, he would repeatedly mumble to himself "Mustn't run away! Mustn't run away!", as if he is speaking to me from the other side of the TV. Rei Ayanami, the heroine of the series, struggled to find a meaning for existence, but would eventually give everything to protect her bonds with the people she holds dear. Rei's unworldly beauty radiates into my heart and becomes my guiding moonlight in the darkest of nights. To summarize the message of *Evangelion* series in one quote from the final episode-

> *"Anywhere can be paradise as long as you have the will to live."*

Table of Contents

List of Figures

1- General Introduction

Human induced pluripotent stem cells (iPSCs) can generate virtually any cell type in the body and are being used to model human development and diseases, to screen for drugs, and to develop new cell replacement therapies. Significant progress has been made in developing methodologies for targeted differentiation of human iPSCs into various cell types, including cells in the nervous system (Liu and Zhang, 2011; Petros et al., 2011). Traditionally, monolayer 2D cultures are used for better external control and to produce more uniform cell populations; however, they lack properties of 3D cell assembly that define endogenous biological systems. Structures resembling whole developing organs, named organoids, have recently been generated from human iPSCs via 3D cultures and include intestinal, kidney, retinal, and cerebral organoids (Lancaster and Knoblich, 2014b; Sasai, 2013; Sato and Clevers, 2013; Yin et al., 2016). Organoid technology evolved from cultures of embryoid bodies, which are 3D aggregates of stem cells that self-organize to develop disparate tissues in vitro, similar to teratoma formation in vivo. Organoids provide a unique opportunity to model organ development in a culture system that is remarkably similar to human organogenesis in vivo, which is not accessible to experimentation. One example would be using cerebral organoids to address the current global public health emergency concerning a suspected link between Zika virus (ZIKV) infection and microcephaly (Heymann et al., 2016).

One recent major advance in cerebral organoid technology was the use of a spinning bioreactor to facilitate nutrient and oxygen absorption, which enables formation of longer continuous neuroepithelial-like zones and growth of large, complex organoids that more closely resemble the human brain than previous studies (Lancaster et al., 2013). Derived from the early NASA-designed rotating wall vessel bioreactor to simulate microgravity, this technology potentially offers two additional benefits: low fluid shear stress to promote cell-cell interactions and initiation of differentiation signaling (Goodwin et al., 1993); and randomized gravitational vectors that affect intracellular signal transduction and gene expression (Jessup et al., 1993). This and other pioneering human cerebral organoid technologies (Kadoshima et al., 2013a; Lancaster et al., 2013; Mariani et al., 2015; Muguruma et al., 2015; Pasca et al., 2015) have generated substantial excitement for using organoids to model human brain development and disorders (Bae and Walsh, 2013; Bershteyn and Kriegstein, 2013; Chambers et al., 2013; Lancaster and Knoblich, 2014b).

2 – General Methods

2.1 - Maintenance of Human iPSCs

Human iPSC lines used in the current study were previously fully characterized (Wen et al., 2014; Yoon et al., 2014). They were cultured in stem cell medium consisting of DMEM:F12 (Invitrogen) supplemented with 20% Knockout Serum Replacer (Gibco), 1X Non-essential Amino Acids (Invitrogen), 1X Penicillin/Streptomycin, 1X 2-Mercaptoenthanol (Millipore), 1X Glutamax (Invitrogen), and 10 ng/mL FGF-2 as previously described (Yoon et al., 2014). Culture medium was changed every day. iPSCs were passaged every week onto a new plate pre-seeded with irradiated CF1 mouse embryonic fibroblasts (Charles River). iPSCs were detached from the plate by treatment of 1 mg/mL Collagenase Type IV (Invitrogen) for 1 hr. iPSC colonies were further dissociated into smaller pieces by manual pipetting. All studies were performed with approved protocols of Johns Hopkins University School of Medicine.

2.2 - Tissue Preparation and Immunohistochemistry

Whole organoids were fixed in 4% Paraformaldehyde in Phosphate Buffered Saline (BPS) for 30-60 min at room temperature. Organoids were washed 3 times with PBS and then incubated in 30% sucrose solution overnight. Organoids were embedded in freezing medium and sectioned with a cryostat (Leica). For immunostaining, freezing medium was washed with PBS before permeabilization with 0.2% Triton-X in PBS for 1 hr. Tissues were blocked with blocking medium consisting of 10% donkey serum in PBS with 0.1% Tween-20 (PBST) for 30 min. Primary antibodies diluted in blocking solution were applied to the sections overnight at 4ºC. After washing with PBST, secondary antibodies diluted in blocking solution were applied to the sections for 1 hr at room temperature. Finally, the sections were washed with PBST and stained with DAPI. All images were captured by a confocal microscope (Zeiss LSM 700). For paraffin-embedded human samples, slides were first deparaffinized and retrieved using sodium citrate heated to boil in a microwave oven and immunostained as above.

3 - Establishing the brain region-specific organoid systems as models for human brain development

(This chapter was published(Qian et al., 2016). I am the first author and was involved in all aspects of the study.)

3.1 – Introduction

The rapidly advancing field of stem cell biology continually provides new insights into basic biology and human disorders and drives innovation for new patient treatments. In the past 10 years, human induced pluripotent stem cells (iPSCs) have emerged as an invaluable tool in modeling human disorders, especially those with complex genetic origins that are challenging to model in animals (Takahashi et al., 2007; Wen et al., 2016). IPSCs are somatic cells that have been reprogrammed into a pluripotent stem cell state, similar to embryonic stem cells. Under specific cues and favorable conditions, iPSCs can theoretically be differentiated into any cell or tissue types found in the human body. A new frontier of stem cell research is to generate three-dimensional (3D) tissue structures to model organogenesis and developmental disorders. Brain organoids are human pluripotent stem cell-derived 3D tissues that self-assemble into organized structures resembling the fetal human brain (Jo et al., 2016; Kadoshima et al., 2013a; Lancaster et al., 2013; Mariani et al., 2015; Pasca et al., 2015; Qian et al., 2016). Unlike conventional 2D cell cultures, organoids recapitulate human organogenesis not only at the cellular level, but also in architecture and developmental trajectory, therefore providing a unique opportunity to model human organogenesis, which is not accessible to direct experimentation.

Despite the promise inherent in these pioneering organoid technologies, we are at the very beginning of an era to engineer human brain models. First, currently available spinning bioreactors require a large volume of culture medium and incubator space. With frequent medium changes over several months of culturing, the system is cost-prohibitive for a majority of laboratories to maintain and precludes scalability, use of expensive growth factors, or screening of chemical compounds. It also presents a major roadblock for testing multiple conditions to optimize protocols. Second, the current cerebral organoid method ("intrinsic protocol") is based on self-assembly of cells without external control, and each organoid is comprised of heterogeneous cell types found in forebrain, hindbrain, and retina (Lancaster et al., 2013). Large sample to sample variability for all current technologies make quantitative analysis challenging and limit their broad applications. Third, some key features of human brain development have yet to be recapitulated in a robust manner in cerebral organoids reported so far. For example, unlike rodents, the embryonic human cerebral cortex contains an abundant population of specialized outer radial glia cells (oRGCs) in the outer subventricular zone (oSVZ) that are believed to contribute significantly to the evolutionary increase in the size and complexity of human cortex (Dehay et al., 2015; Lui et al., 2011; Taverna et al., 2014). Cerebral organoids generated with existing protocols contain only sparse progenitors with morphological characteristics of oRGCs and none have exhibited a well-developed oSVZ layer (Kadoshima et al., 2013a; Lancaster et al., 2013; Mariani et al., 2015; Pasca et al., 2015). Taken together, there is a critical need to develop an organoid platform with drastically reduced cost and higher throughput, increased reproducibility and minimal variability, and better resemblance of critical aspects of human cortical development.

3.2 - Methods

3.2.1 - Bioreactor Design, Printing and Assembling

We used SolidWorks for design and drawings of all parts, including spinning sleeves and shafts (CAD files to be deposited in the public domain). Cover units were designed to fit a standard 12-well culture plate. Autoclavable plates and spinning shafts were printed with a 3D printer (Fortus 450mc) using ULTEM 9085, and other parts were printed using polycarbonate. Standalone spinning bioreactors were assembled from parts consisting of IG16 6VDC 051 RPM Gear Motor (SuperDroid Robots TD-060-051), gears (GR.MOLD.SP.M0.5 (US); SDP/SIA 1Z 2MYZ0505206), sleeve bearings (Metric PTFE Sleeve Bearing, for 6 mm Shaft Diameter, 12 mm OD, 10 mm Length; McMaster-Carr 2685T11), Aluminum Unthreaded Spacers (1/4" OD, 3/4" Length, #4 Screw Size; McMaster-Carr 92510A308), and power supply (Hosa Cable ACD477 Universal AC Power Supply; Amazon). The modular individual bioreactors were made to fit into a stackable bioreactor with some modifications. All gears in the stackable bioreactor were driven by a more powerful motor (IG32 Right Angle 12VDC 043 RPM Gear Motor; SuperDroid Robots TD-035-043) connected to a series of shaft couplings (Rigid, Setscrew; Misumi CPR16-6-6), rotary shafts (D Cut; Misumi SSFRV6-55-F19-T12), bearings (Single Row, Metric Sizes, Acetal Plastic Radial Ball Bearings fitted with Glass Balls; KMS Bearings A626-G), and gears (Module 0.5, 96 Teeth, 20° Pressure Angle, Acetal/Brass Insert Spur Gear (SDP/SIA 1Z 2MYZ0509606).

3.2.2 - Culture of Forebrain Organoids from Human iPSCs

To generate forebrain-specific organoids, human iPSC colonies were detached with Collagenase Type IV 7 days after passage, washed with fresh stem cell medium and cultured in a 15 ml conical tube. On day 1, detached and washed iPSC colonies were transferred to an Ultra-Low attachment 6-well plate (Corning Costar), containing 3 ml of stem cell medium (without FGF-2), plus 2 µM Dorsomorphine (Sigma) and 2 µM A83-01 (Tocris). On days 5-6, half of the medium was replaced with induction medium consisting of DMEM:F12, 1X N2 Supplement (Invitrogen), 10 µg/ml Heparin (Sigma), 1X Penicillin/Streptomycin, 1X Non-essential Amino Acids, 1X Glutamax, 4 ng/ml WNT-3a (R&D Systems), 1 µM CHIR99021 (Cellagentech), and 1 µM SB-431542 (Cellangentech). On day 7, organoids were embedded in Matrigel (BD Biosciences) and continued to grow in induction medium for 6 more days. On day 14, embedded organoids were mechanically dissociated from Matrigel by pipetting up and down onto the plate with a 5 ml pipette tip. Typically, 10 - 20 organoids were transferred to a 12-well spinning bioreactor (SpinΩ) containing differentiation medium consisting of DMEM:F12, 1X N2 and B27 Supplements (Invitrogen), 1X Penicillin/Streptomycin, 1X 2-Mercaptoenthanol, 1X Non-essential Amino Acids, 2.5 µg/ml Insulin (Sigma). At day 71, differentiation medium was exchanged with maturation medium consisting of Neurobasal (Gibco), 1X B27 Supplement, 1X Penicillin/Streptomycin, 1X 2-Mercaptoenthanol, 0.2 mM Ascorbic Acid, 20 ng/ml BDNF (Peprotech), 20 ng/ml GDNF (Peprotech), 1 ng/ml TFGβ (Peprotech), and 0.5 mM cAMP (Sigma). The organoids could grow beyond 110 days in maturation medium. All media were changed every other day. For the stationary culture, day 14 organoids were generated following the same protocol above and were maintained in non-attaching 6 well plate with differentiation media. The intrinsic protocol for spontaneous differentiation of human iPSCs into cerebral organoids followed the published protocol (Lancaster et al., 2013).

3.2.3 - Culture of Midbrain Organoids from Human iPSCs

To generate midbrain-specific organoids, human iPSC colonies were detached with Collagenase Type IV 7 days after passage and washed with fresh stem cell medium in a 15 ml conical tube. On day 1, the detached and washed iPSC colonies were transferred to an Ultra-Low attachment 6-well plate containing EB medium consisting of DMEM:F12, 15% Knockout Serum Replacer, 1X Glutamax, 1X 2-Mercaptoenthanol, 100 nM LDN-193189, 10 µM SB-431542, 100 ng/ml SHH (Peprotech), 2 µM Purmorphamine (Stemgent), 100 ng/ml FGF-8 (Peprotech). On day 5, EB medium was gradually switched to SHH medium consisting of DMEM:F12, 1X N2 Supplement, 1X Glutamax, 100 nM LDN-193189, 3 µM CHIR99021, 100 ng/ml SHH, 2 µM Purmorphamine, 100 ng/ml FGF-8. On day 7, SHH medium was replaced with induction medium consisting of DMEM:F12, 1X N2 Supplement, 1X Glutamax, 100 nM LDN-193189, 3 µM CHIR99021. On day 14, 10-20 organoids were transferred to SpinΩ with differentiation medium consisting of Neurobasal, 1X B27 Supplement, 1X Glutamax, 1X 2-Mercaptoenthanol, 20 ng/ml BDNF, 20 ng/ml GDNF, 0.2 mM Ascorbic Acid, 1 ng/ml TGFβ, and 0.5 mM c-AMP. All media was changed every other day.

3.2.4 - Culture of Hypothalamus Organoids from Human iPSCs

To generate hypothalamus-specific organoids, human iPSC colonies were detached with Collagenase Type IV after 7 days following passaging and washed with fresh stem cell medium in a 15 ml conical tube. On day 1, the detached and washed iPSC colonies were transferred to an Ultra-Low attachment 6-well plate (Corning Costar) containing stem cell medium. One day after (day 2), stem cell medium was replaced with induction medium A consisting of DMEM:F12, 10% Knockout Serum Replacer, 1X Non-essential Amino Acids, 1X Penicillin/Streptomycin, 1X 2-Mercaptoenthanol, 1X Glutamax, 2.5 M LDN-193189 (Stemgent), 3 M SB-431542, and 450 M 1-Thioglycerol (Sigma). On day 4, the medium was switched to induction medium B consisting of DMEM:F12, 10% Knockout Serum Replacer, 1X Non-essential Amino Acids, 1X Penicillin/Streptomycin, 1X Glutamax, 1X N2 Supplement, 10 ng/m Wnt-3A, 20 ng/ml SHH, and 2 M Purmorphamine. On day 7, 5-10 organoids were transferred to a 12-well spin bioreactor and induction medium B was replaced with differentiation medium consisting of DMEM:F12/Neurobasal (1:1 ratio), 1X B27 Supplement, 1X Non-essential Amino Acids, 1X Penicillin/Streptomycin, 1X Glutamax, 10 ng/ml FGF-2 and 10 ng/ml CTNF (Peprotech). All media were changed every other day.

3.2.5 - BPA Treatment Experiment

Forebrain organoids were grown using protocol described above. For long-term BPA treatment experiments, forebrain organoids at day 14 from the same batch were distributed randomly into separate wells within SpinΩ and treated with corresponding concentrations of BPA (Sigma). BPA was dissolved in sequential dilution in differentiation media with 0.05% methanol, which was also added in the control condition. Media containing BPA was replaced every other day until day 28 for analysis. A previous study determined that tissue culture plates do not contain detectable BPA (Biswanger et al., 2006). Quantification was conducted by investigators blind to culture conditions.

For acute BPA treatment experiment, forebrain organoids were grown to day 28 and treated with corresponding concentration of BPA for 24 hours. At day 29, the culture media was replaced with fresh media and washed 3 times to remove residual BPA. Organoids were then pulsed with 10 μM EdU for 2 hr. The media were then replaced and organoids were washed 3 times with fresh media. At day 30, organoids were fixed for immunohistochemistry and EdU detection using Click-iT® EdU Alexa Fluor® 488 Imaging Kit (ThermoFisher C10337) according to the manufacturer's manual, followed by immunostaining for SOX2 and PH3. Imaging was acquired in Zeiss LSM 700 Confocal system at 25x magnification. Quantification was performed by counting the number of EdU and PH3$^+$ nuclei within SOX2$^+$ ventricular structures that were recognized by neural tube-like morphology. EdU and PH3 densities were normalized to the area of ventricular structures measured in ImageJ software. Quantification was conducted by investigators blind to culture conditions.

3.2.6 - Quantification of Cell Fates and Layer Thickness

For cell fate quantifications, organoids grown from the intrinsic protocol and forebrain protocol were immunostained for SOX2, PAX6 and OTX2 at day 14. Images were acquired with Zeiss Axiovert 200M fluorescent microscope. Neural tube structures were counted as positive for forebrain markers when more than 80% of all nuclei were positive for respective markers. Markers for different brain regions (FOXA2, NKX2.1 and PROX1) were quantified by measuring the area stained positive for markers and normalized to DAPI in ImageJ software.

Organoids grown from the intrinsic protocol and forebrain protocol were immunostained for SOX2, TUJ1 and CTIP2 at day 14 and 28. The ventricular-like zone (VZ) was defined by SOX2 immunoreactivity and neural-tube morphology and the outer layer was defined by the area outside the VZ to the nearest pial surface. For each ventricular structure, 3 measurements were performed forming a right-angle fan area pointing to the nearest pial surface, at 0, 45 and 90 degrees. The length for VZ and outer layer was measured in ImageJ software. The relative VZ thickness was defined as the ratio of VZ thickness to VZ plus outer layer thickness. Layer thickness measurements at day 56 and 85 in forebrain organoids were performed similarly as described above with the addition of SVZ. The SVZ was defined by the region within mixed population of SOX2$^+$ and CTIP2$^+$ nuclei outside the VZ. The cortical plate (CP) was defined by the region from the boundary of SVZ to the pial surface within exclusive CTIP2$^+$ nuclei. Relative thicknesses for VZ, SVZ and CP were calculated by the ratio to total thickness from ventricular to pial surface.

3.2.7 - RNA-Seq and Bioinformatic Analysis

Forebrain organoids at days 26, 40, 54 and 100 (three samples for the first three time points and two samples for day 100) were collected and processed for RNA-seq and bioinformatics analyses as previously described (Guo et al., 2014).

Sequence read counts for 22 different human fetal organs were obtained from GSE66302. The sequences were aligned to UCSC hg19 reference genome using Bowtie

(Langmead and Salzberg, 2012), and the read counts were obtained using R/Bioconductor (Gentleman et al., 2004). Human dorsolateral prefrontal cortex RNA-seq datasets (RPKM values) from six different life stages were obtained from (Jaffe et al., 2015) (http://www.nature.com/neuro/journal/v18/n1/extref/nn.3898-S9.zip). RNA-seq gene expression (RPKM) for 11 time points of fetal development and 16 different brain regions were obtained from Allen Brain Atlas (http://www.brain-map.org/). All gene expression values are summarized as the log RPKM values against the Ensembl gene annotation.

To assess the correlations of gene expressions between organoids from the current study and fetal organs, we first select genes with moderately high average expression levels and variance. Briefly, we only used genes with average expression levels greater than three and variance greater than one from fetal organs. These genes show marked differences among organs and thus are more informative than using all genes in the correlation analysis. Pearson correlations were computed based on expression of these genes. Correlations were averaged for biological replicates show all the correlation values. We found that the patterns of correlation were stable against the gene selection criteria. Thresholds used for selecting genes, albeit arbitrary, had very little impact on the final results. The same strategy was used to compute the correlations between organoid and other samples (brains at different developmental stages and regions).

Differentially expressed genes between D26 and late stages of organoids were defined as genes with absolute log fold changes of RPKM greater than one, and the average base line expression (log RPKM) greater than 2. Schizophrenia-related risk genes were obtained from Schizophrenia Gene Resource (SZGR) (http://bioinfo.mc.vanderbilt.edu/SZGR/). Autism-related risk genes were obtained from Simons Foundation Autism Research Initiative (SFARI) (https://gene.sfari.org/autdb/HG_Home.do). The significance of gene overlap was assessed by chi-squared test on 2-by-2 tables.

R programming language was used to perform all data analysis and generate the figures.

3.2.8 - Electroporation

Organoids at day 50 were transferred into Petri dish containing PBS, and 2 l of GFP expressing plasmid (pCAGGS-eGFP, 2 g/ l, diluted in sterile PBS with 0.01% fast green) was injected into 3-4 locations within an organoid using a beveled and calibrated micropipette. Five pulses (40 V, 50 ms in duration with a 950 ms interval) were delivered with tweezer electrodes (CUY650-5, Nepa Gene) by a CUY21SC electroporator (Nepa Gene) as previously described (Yoon et al., 2014). Electroporated organoids were transferred back to SpinΩ and cultured until fixation.

3.2.9 - Electrophysiology

Organoid slices were prepared by embedding organoids in 4% low melting point agarose cooled to approximately 32°C. Slices (250 µm) were sectioned using a vibratome (Microm HM650V) and stored at room temperature, oxygenated (95% 02, 5% CO2) artificial cerebrospinal fluid (ACSF) containing (in mM): 125 NaCl, 25 NaHCO3, 1.25 NaH2PO4, 3 KCl, 25 dextrose, 1 MgCl2, and 2 CaCl2, pH 7.3. Slices were immediately ready for recording.

For all experiments, ACSF was oxygenated (95% O2, 5% CO2) and bath temperature was approximately 38°C. Patch pipettes were fabricated from borosilicate glass (N51A, King Precision Glass, Inc.) to a resistance of 2-5 MΩ. For current- and voltage-clamp measurements pipettes were filled with (in mM): 125 potassium gluconate, 10 HEPES, 4 Mg-ATP, 0.3 Na-GTP, 0.1 EGTA, 10 phosophocreatine, 0.05%, adjusted to pH 7.3 with KOH. For all experiments GABAA receptors were blocked with SR-95531 (Gabazine, 5 µM, Abcam). In sEPSC experiments, synaptic currents were blocked with 6,7-Dinitroquinoxaline-2,3-dione (DNQX, 10µM, Abcam). Sodium currents and action potentials were blocked with tetrodotoxin (TTX, 300 nM, Abcam). Current signals were recorded with either an Axopatch 200B (Molecular Devices) or a Multiclamp 700A amplifier (Molecular Devices) and were filtered at 2 kHz using a built in Bessel filter and digitized at 10 kHz. Voltage signals were filtered at 2 kHz and digitized at 10kHz. Data were acquired using Axograph on a Dell PC (Windows 7). For voltage clamp recordings, cells were held at -70 mV.

3.2.10 - Calcium Imaging Analysis

Calcium imaging was performed similarly as previously described (Kim et al., 2012). Organoids were loaded with Fluo-4 (Life Technologies) for 30 min before the start of imaging. Throughout experiments, oxygenated aCSF was continuously perfused at a rate of 3 ml/min at room temperature (25 ± 2°C). Glutamate and GABA were added to media during imaging sessions at a final concentration of 20 µM and 10µM, respectively. Bicuculline was added by bath application to media during imaging at a final concentration of 50 µM and imaging was resumed after a 15-min incubation time. Cells were excited at 488 nm, and Fluo-4 signal was collected at 505–550 nm. Images were acquired and analyzed using NIH Image J software. The $Ca2^+$ signal change was determined by ΔF/F [ΔF/F = [(F1-B1)-(F0-B0)]/(F0-B0)], which was normalized to the mean fluorescence intensity measured at the baseline condition (set as 0%).

3.3 - Results

3.3.1 - A Miniaturized Spinning Bioreactor to Optimize Organoid Cultures from Human iPSCs

To drastically reduce the cost for culturing organoids under each condition, we attempted to miniaturize the large spinning flask. Because of differences in fluid dynamics, we could not simply proportionally scale down the system in size. Instead, we engineered a multi-well spinning device to fit a standard 12-well tissue culture plate (Figure 1A). Above the cover, spin shafts are attached to a set of 13 interconnecting gears, driven by a single electric motor for synchronous rotation (Figure 1A). We used Computer-Aided Design software Solidworks to design and 3D print each component, including the spinning shaft and leaf, and plate cover. We assembled prototypes to optimize fluid dynamics that sustains organoids of varying sizes in suspension under moderate spinning speed, and prevents organoid aggregation underneath the shaft at the center of each well. After multiple rounds of systematic optimization of individual components, including number, shape, size and angle of leaves, and diameter, length and shape of shaft, we arrived at SpinΩ, a miniaturized spinning bioreactor unit that requires as little as 2 ml of medium per well, a 50-fold reduction in medium consumption and drastically reduced incubator space. We further designed a stackable version with insertable cassettes to be driven by one common motor. The miniaturized spinning bioreactor permits comparisons of a large number of conditions in parallel for protocol optimization to achieve minimal variability and high reproducibility.

To reduce the tissue heterogeneity observed in cerebral organoids generated by the "intrinsic protocol" (Lancaster et al., 2013), we pre-patterned embryoid bodies to the fate of a specific brain region. Based on our recently developed protocol for 2D differentiation of human iPSCs into forebrain-specific cortical neural progenitor cells (NPCs) (Wen et al., 2014), we first treated human iPSCs with dual SMAD inhibitors (dorsomorphin and A-83) for 7 days and then embedded embryoid bodies in Matrigel for another 7 days, followed by Matrigel removal and spinning in SpinΩ (Figure 1B). Compared to the "intrinsic protocol", we could reliably generate organoids from multiple iPSC lines with reduced heterogeneity in organoid shape and size. However, there was significant cell death within organoids as shown by activated caspase-3 immunostaining. We then tested combinations of different signaling molecules for various durations. We found that treatment with three factors, GSK-3β inhibitor CHIR99021, recombinant Wnt3A protein, and SMAD inhibitor SB-431542, during the Matrigel stage drastically reduced numbers of activated caspase-3^+ cells within organoids at day 14. Later we found that Wnt3A contribution was minimal, likely because Wnt3A and CHIR99021 activate the same downstream signaling pathway. Notably, nearly all cells within organoids self-assembled into organized neuroepithelial tissue at this stage and individual neuroepithelial structures were consistently much larger than those generated without treatment of these factors. At day 14, well-defined polarized neuroepithelium-like structures resembled neural tubes in embryonic development, with a pure population of NESTIN$^+$SOX2$^+$ NPCs, and expression of adherent junction markers (β-CATENIN and PKCλ) and proliferation marker phospho-Histone H3 (PH3) localized exclusively at the ventricular surface (Figure 1C). Upon spinning in SpinΩ, these organoids developed into multi-layer stratified structures, composed of $SOX2^+$ NPCs, $TBR2^+$ intermediate progenitor cells (IPCs) and $CTIP2^+$ neuron layers (Figure 1D). With the small volume of culture medium required, it became affordable to supplement with growth factors, such as BDNF, GDNF and TGFβ, at later stages to promote survival, neuronal maturation and expansion of cortical layer sizes (Figure 1B).

As comparisons, we followed the same protocol but maintained organoids in stationary culture after day 14. At day 42, there was substantial cell death in the interior of organoids as shown by activated caspase-3 immunostaining. In addition, ventricular structures were largely absent in these organoids; instead, extensive neurogenesis without defined organization was observed. We also cultured our forebrain organoids using orbital shakers (Lancaster and Knoblich, 2014a). Under a similar rotation speed that we used for spinning in SpinΩ, shaking generated rotational movements causing organoids to roll on the culture plate bottom. At day 42, organoids showed substantial cell death in the neuronal layer despite retaining defined ventricular structures. After day 50, many of these organoids disintegrated. These results suggest that spinning cultures enhance cell viability and promote maintenance of the stem cell niche at least for forebrain organoids generated using our protocol. The miniaturized spinning bioreactor platform opens doors for cost-effective generation of organoids from human iPSCs and provides access and affordable organoid technology to a broader scientific community.

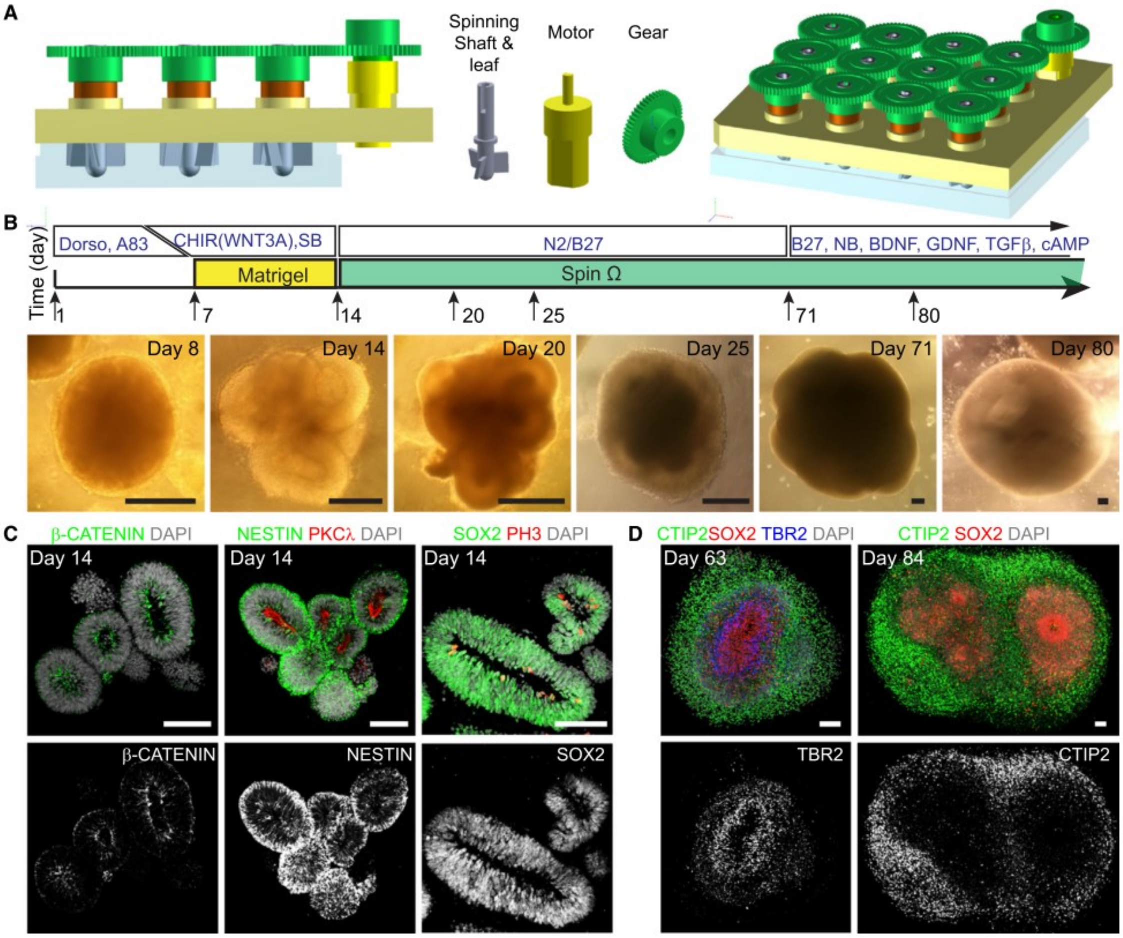
A
Spinning Shaft & leaf
Motor
Gear
B
Time (day)
Dorso, A83
CHIR(WNT3A),SB
N2/B27
B27, NB, BDNF, GDNF, TGFβ, cAMP
Matrigel
Spin Ω
1
7
14
20
25
71
80
Day 8
Day 14
Day 20
Day 25
Day 71
Day 80
C
β-CATENIN DAPI
NESTIN PKCλ DAPI
SOX2 PH3 DAPI
Day 14
Day 14
Day 14
β-CATENIN
NESTIN
SOX2
D
CTIP2 SOX2 TBR2 DAPI
CTIP2 SOX2 DAPI
Day 63
Day 84
TBR2
CTIP2

Figure 1. SpinΩ Bioreactor-based Forebrain Organoid Culture System.

(A) *Computer-Aided-Design (CAD) drawings of the 12-well version SpinΩ bioreactor and individual parts.*

(B) *Schematic diagram of the protocol for generating forebrain organoid and sample phase images at different stages. Scale bars: 100 µm (Day 8 – 25) and 500 µm (Day 71 and 80). See Experimental Procedures for details. Dorso: Dorsomorphin (2 µM); A83: A-83-01 (2 µM); CHIR: CHIR99021 (1 µM); SB: SB-431542 (1 µM); B27: B27 supplement; N2: N2 supplement; NB: Neurobasal medium; GDNF: Glial cell-derived neurotrophic factor (20 ng/ml); BDNF: Brain-derived neurotrophic factor (20 ng/ml); TGFβ: Transforming growth factor beta (1 ng/ml); cAMP: cyclic adenosine monophosphate (0.5 mM).*

(C) *Immunostaining of neuroepithelium-like tissue formed at day 14 for adherent junction markers (β-Catenin and PKCλ), neural progenitor cell (NPC) markers (SOX2 and Nestin). Neuroepithelium-like tissue exhibits apical-basal polarity with the apical surface identified by PKCλ expression and PH3*$^{+}$ *cells undergoing mitosis. Scale bars: 100 µm.*

(D) *Immunostaining of forebrain organoids at day 63 (left) and 84 (right) for the NPC marker (SOX2), intermediate progenitor cell (IPC) marker (TBR2) and cortical neuron marker (CTIP2).*

Scale bars: 100 µm (Day 63) and 200 µm (Day 85).

3.3.2 - Organoids with a Forebrain Identity and Increased Homogeneity

We next performed detailed characterization of early stage forebrain organoids produced in SpinΩ (Figure 1B). At day 14, immunohistological analysis showed almost exclusive expression of forebrain-specific progenitor markers, including PAX6, OTX2 (Figure 2A) and FOXG1, with minimal expression of markers for other brain regions tested. We obtained similar results with multiple iPSC lines and with different clones of the same iPSC lines (Figure 2A). Consistent with previous findings, cerebral organoids generated in large spin flasks using the "intrinsic protocol" exhibited diverse brain region identities with less than 50% of rosettes expressing forebrain markers PAX6 or OTX2 (Figure 2A).

We further assessed the temporal homogeneity of neuronal differentiation via quantification of the relative thickness of the SOX2$^+$ ventricular zone-like (VZ) layer and the TUJ1$^+$ neuronal layer between apical and basal surfaces (Figure 2B). At day 14, organoids generated using the "intrinsic protocol" exhibited varying degree of neurogenesis, whereas very few neuronal progenies were detected in forebrain organoids. As a result, our protocol produced organoids with nearly 100% of cells organized as the VZ layer, compared to significant variability using the "intrinsic protocol" (Figure 2B). By day 28, we observed both a SOX2$^+$ progenitor layer and a TUJ1$^+$/CTIP2$^+$ neuronal layer (Figure 2C). Forebrain organoids further exhibited a consistent ratio between progenitor and neuronal layers, compared to the large variability using the "intrinsic protocol" (Figure 2D). These quantitative analyses indicate that forebrain organoids exhibit markedly enhanced homogeneity, in term of both brain region identity and timing of differentiation.

The apparent homogeneity of forebrain organoids, small medium volume per condition and multi-well format of SpinΩ comprise a platform amenable to chemical compound testing. As a proof-of-principle, we tested the effect of Bisphenol A (BPA), which is commonly found in household plastic products and has been shown to affect rodent neural development (Kinch et al., 2015; Kundakovic et al., 2013; Mathisen et al., 2013). We treated forebrain organoids from day 14 to 28 with a range of concentrations of BPA and observed a dose-dependent decrease in the relative VZ thickness at day 28 (Figure 2E-F). To explore potential underlying cellular mechanism, we treated forebrain organoids acutely with a range of higher concentrations of BPA for 24 hours and then pulse-labeled proliferating cells with EdU. Quantitative analysis showed a dose-dependent decrease in the density of EdU^+ or $PH3^+$ NPCs, suggesting that reduced NPC proliferation contributes to a decrease in the relative VZ thickness.

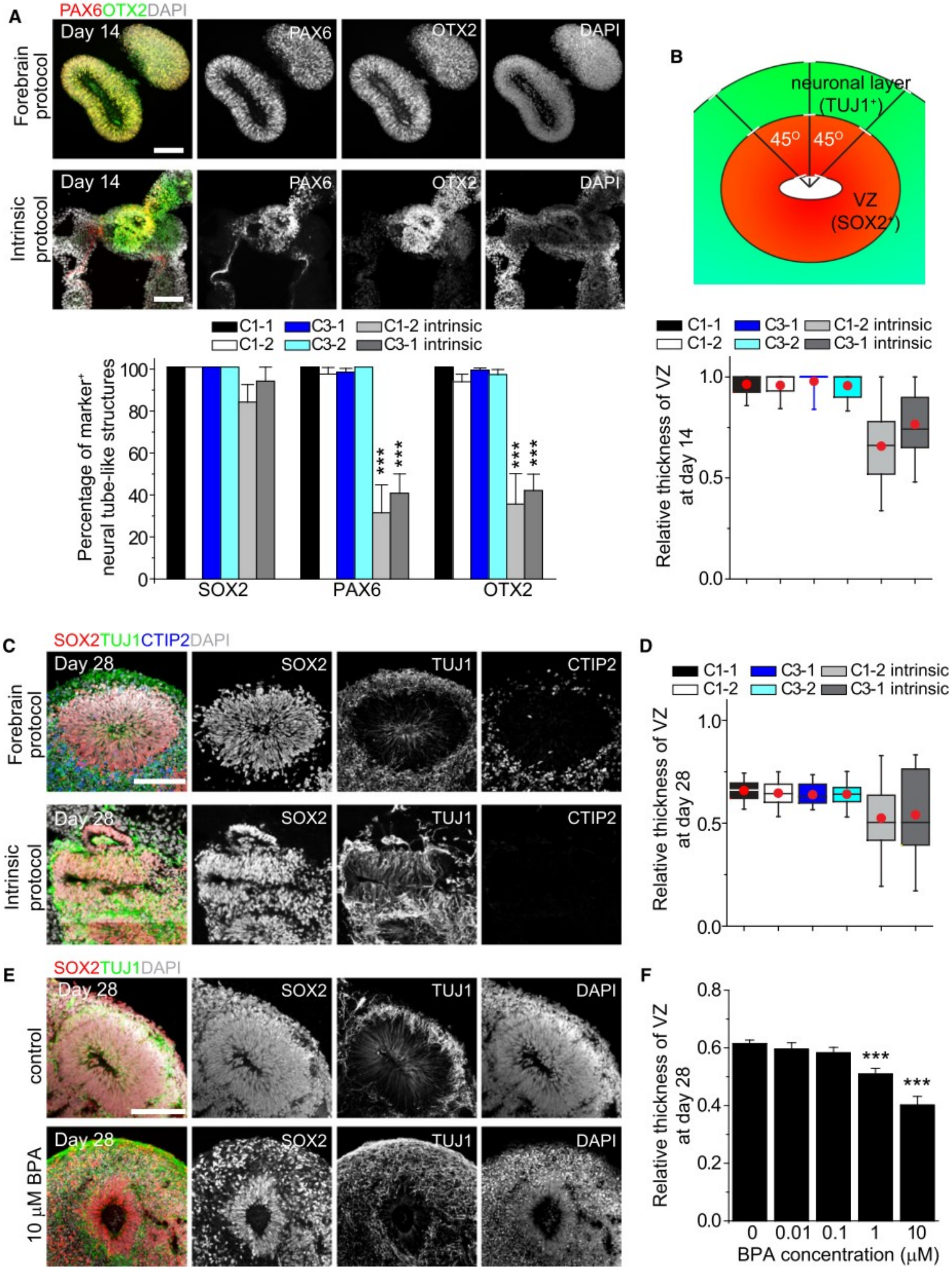
A
PAX6OTX2DAPI
Day 14
PAX6
OTX2
DAPI
Forebrain protocol
Day 14
PAX6
OTX2
DAPI
Intrinsic protocol
B
neuronal layer (TUJ1⁺)
45° 45°
VZ (SOX2⁺)
C1-1 C3-1 C1-2 intrinsic
C1-2 C3-2 C3-1 intrinsic
Percentage of marker⁺ neural tube-like structures
0 20 40 60 80 100
SOX2 PAX6 OTX2
***
Relative thickness of VZ at day 14
0.0 0.5 1.0
C
SOX2TUJ1CTIP2DAPI
Day 28
SOX2
TUJ1
CTIP2
Forebrain protocol
Day 28
SOX2
TUJ1
CTIP2
Intrinsic protocol
D
C1-1 C3-1 C1-2 intrinsic
C1-2 C3-2 C3-1 intrinsic
Relative thickness of VZ at day 28
0.0 0.5 1.0
E
SOX2TUJ1DAPI
Day 28
SOX2
TUJ1
DAPI
control
Day 28
SOX2
TUJ1
DAPI
10 μM BPA
F
Relative thickness of VZ at day 28
0.0 0.2 0.4 0.6 0.8
***
0 0.01 0.1 1 10
BPA concentration (μM)

Figure 2. Homogeneity of Early Stage Forebrain Organoids and Effects of BPA.

(A) *Sample images and quantification among multiple iPSC cell lines and clones for immunostaining of forebrain progenitor marker (Pax6 and OTX2) in neural tube-like structures generated from either the forebrain or the "intrinsic protocols" at day 14. Scale bars: 100 µm. Values represent mean ± SEM (42- 128 total neural tube structures for the forebrain protocol and 11- 30 total neural tube structures for the intrinsic protocol from at least 10 organoids each; *$P < 0.05$, Student's t-test).*

(B) *Schematic drawing for $SOX2^+$ ventricular zone (VZ) and $TUJ1^+$ neuronal layer measurement in cortical structures (top panel) and box plot for relative VZ thickness in day 14 organoids generated using forebrain and intrinsic protocols (Bottom panel). For each cortical structure, three measurements were taken at 45 degree angles to obtain the mean value. Relative VZ thickness= ratio of VZ thickness to total thickness from ventricular surface to pial surface. See Experimental Procedures for details. The red dot indicates mean; upper and lower error bars in each box plot represent the top whisker (maximum value) and bottom whisker (minimum value), respectively (30 cortical structures for the forebrain protocol and 15 cortical structures for the intrinsic protocol from at least 10 organoids each).*

(C) *Sample images of immunostaining for NPC marker (SOX2) and neuronal marker (TUJ1 and CTIP2) in organoids from the forebrain or "intrinsic protocols" at day 28. Scale bars: 100 µm.*

(D) *Box plot for relative VZ thickness at day 28. Similar to (B) (20 cortical structures from at least 10 organoids each).*

(E-F) *Effect of BPA on forebrain organoids. Shown are sample images of immunostaining for NPC marker (SOX2) and neuron marker (TUJ1) to control and BPA-treated forebrain organoids (E) and quantification of relative VZ thickness (F) at day 28. Organoids were treated with BPA from day 14 to 28. Scale bar: 100 µm. Values represent mean ± SEM. ($n = 21$ cortical structures from at least 10 organoids; ***$P < 0.0005$, Student's t-test).*

3.3.3 - Multiple Progenitor Zones that Recapitulate Human Embryonic Neocortex Development

To characterize developmental progression, we systematically performed immunohistochemical analysis of day 28, 56 and 84 organoids. We observed well-defined VZ-like structure with packed SOX2$^+$ NPCs near the lumen at all three time points (Figure 3A-C). At day 28, a layer formed above the VZ containing a mixture of TBR2$^+$ IPCs and CTIP2$^+$ neurons, reminiscent of the preplate (PP) in human cortical development (Figure 3A). By day 56, distinct SVZ-like structures containing a mixture of SOX2$^+$ NPCs, TBR2$^+$ IPCs and immature neurons formed above VZ, and cortical plate-like (CP) structures containing pure CTIP2$^+$ neurons formed above the VZ and SVZ (Figure 3B).

One hallmark of embryonic human cerebral cortex is the prominence of specialized oRGCs in the oSVZ layer (Dehay et al., 2015; Lui et al., 2011). Similar to the developing human cortex, in day 84 organoids a thin gap appeared to separate the expanded SVZ into an inner SVZ-like (iSVZ) region that contains densely packed TBR2$^+$ IPCs and an oSVZ-like region (Figure 3C). Recent studies have identified markers preferentially expressed by oRGCs in the developing human cortex, including HOPX, FAM107A and PTPRZ1 (Pollen et al., 2015; Thomsen et al., 2015). Using antibody reagents that we validated with gestational week 22 (GW22) human tissues, we found a large number of SOX2$^+$HOPX$^+$ oRGCs in day 84 organoids (Figure 3D). Previous cerebral organoid protocols only generated sparse NPCs with apparent oRGC characteristics that did not organize into a progenitor layer outside the VZ (Lancaster et al., 2013). In contrast, our forebrain organoids exhibited a distinct $SOX2^{+}HOPX^{+}$ oSVZ-like layer separated from the $SOX2^{+}HOPX^{-}$ VZ layer (Figure 3D). In some cases, we observed $HOPX^{+}$ radially-oriented basal processes from these oRGCs with pial contact but lacking an apical process, a morphological hallmark of human oRGCs (Hansen et al., 2010). Two other oRGCs markers, FAM107A and PTPRZ1, were also expressed in oSVZ, indicating that these RGCs are molecularly distinct from VZ NPCs (Figure 3E, G). Many $SOX2^{+}$ progenitors in the oSVZ were positive for cell cycle marker Ki67, indicating active cell division in this region (Figure 3F).

The presence of a prominent oRGC-like population in day 84 forebrain organoids offers an opportunity to follow the time-course of oRGC marker expression at different stages of organoid development. A recent study showed that oSVZ-exclusive expression of HOPX, FAM107A and PTPRZ1 does not occur in the developing human cortex until gestational week 15-20 (Pollen et al., 2015). Interestingly, very limited HOPX expression was detected in day 28 organoids, while at day 56 its expression was prominent in both VZ and SVZ, not exclusive to SVZ.

Together, these results demonstrate that forebrain organoids exhibit multi-layer progenitor zone organization that recapitulates embryonic human cortical development, including a prominent oSVZ layer with oRGC-exclusive expression of defined molecular markers. Our system provides a new model to investigate the origin, property and mechanisms that regulate human oRGCs.

3.3.4 - Generation of Diverse Neuronal Subtypes of All Six Cortical Layers

Next, we performed detailed expression analysis of markers for different neuronal subtypes in forebrain organoids over the course of development (Figure 3H). At day 28, the neuronal layer contained neurons expressing deep layer cortical neuron markers CTIP2 and TBR1, as well as neurons expressing the Cajal-Retzius cell marker REELIN (Figure 3I). At day 56 and 70, the SVZ contained neurons weakly expressing CTIP2, a feature of migrating immature neurons found in this region (Lui et al., 2011) (Figure 3J-K). The CP-like structure hosted a dense population of neurons expressing deep layer cortical neuron marker CTIP2 and TBR1, as well as a sparser population expressing upper layer cortical neuron marker SATB2 that were localized closer to the pial surface (Figure 3J-K). There was also a cell-sparse layer visualized by REELIN and DCX expression at the pial surface, resembling the marginal zone (MZ) that normally become layer I in vivo. At day 84, late-born SATB2$^+$ neurons formed a layer partially separated from the early-born CTIP2$^+$ layer, suggesting specification of upper and deep cortical layers (Figure 3L). Furthermore, neurons expressing layer II/III neuron markers CUX1 and BRN2 started to appear with the CUX1$^+$ neuronal layer localized near the pial surface (Greig et al., 2013) (Figure 3L). Quantification showed CP and SVZ layer expansion and VZ layer reduction from day 56 to 84 (Figure 3M). These features resemble the developing human cortex, in which VZ shrinks to 1-2 cell widths across the layer by GW22 and the oSVZ become the dominant progenitor zone responsible for neurogenesis and CP expansion.

Together, these results reveal the developmental time course of marker expression for neurons of all six cortical layers in forebrain organoids (Figure 3H). Importantly, quantitative analysis of different organoids and iPSC lines shows little variability in the relative thickness of different layers (Figure 3M), again indicating robustness and reproducibility of our organoid system.

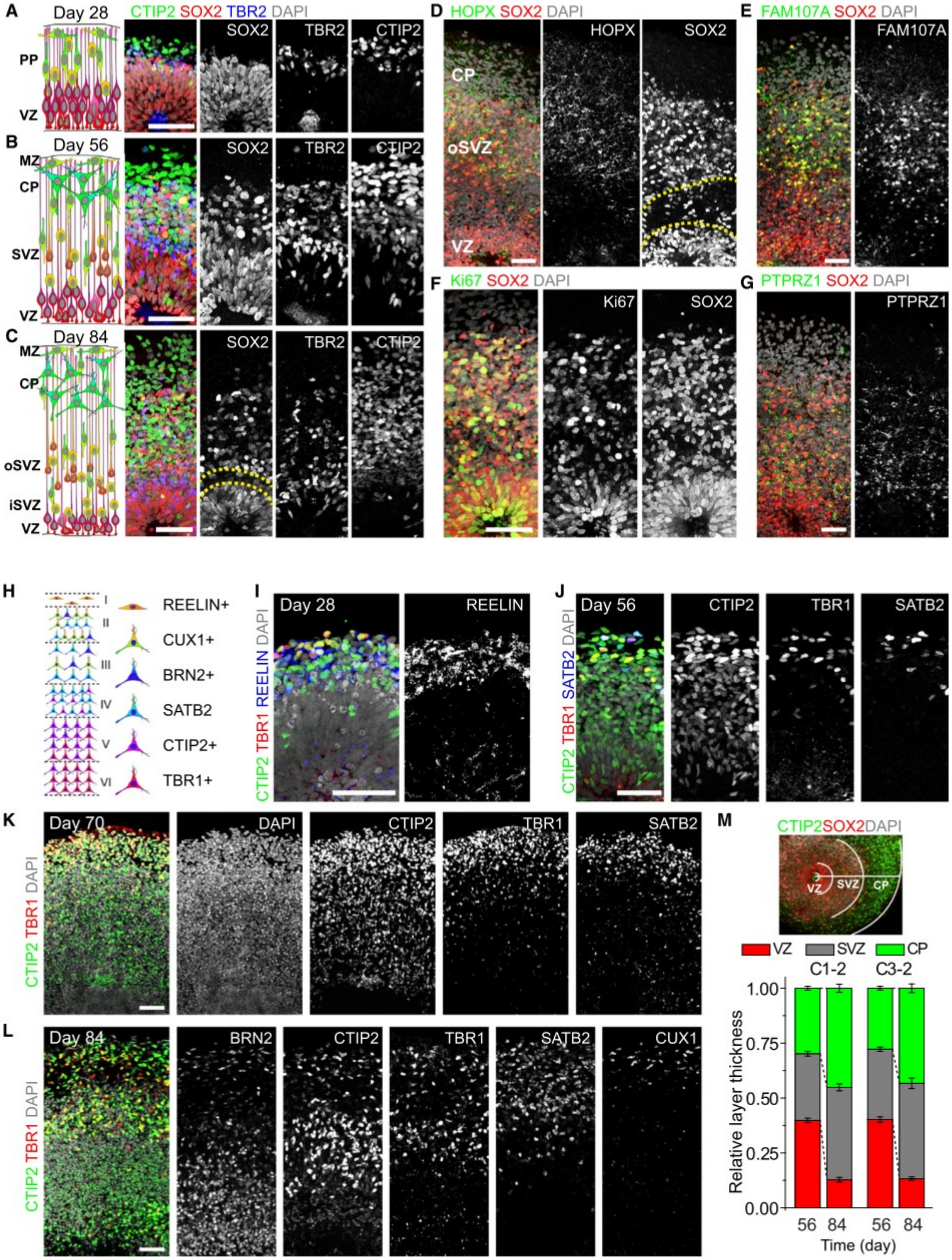
A
Day 28
CTIP2 SOX2 TBR2 DAPI
PP
VZ
SOX2
TBR2
CTIP2
B
Day 56
MZ
CP
SVZ
VZ
SOX2
TBR2
CTIP2
C
Day 84
MZ
CP
oSVZ
iSVZ
VZ
SOX2
TBR2
CTIP2
D
HOPX SOX2 DAPI
CP
oSVZ
VZ
HOPX
SOX2
E
FAM107A SOX2 DAPI
FAM107A
F
Ki67 SOX2 DAPI
Ki67
SOX2
G
PTPRZ1 SOX2 DAPI
PTPRZ1
H
I
II
III
IV
V
VI
REELIN+
CUX1+
BRN2+
SATB2
CTIP2+
TBR1+
I
Day 28
CTIP2 TBR1 REELIN DAPI
REELIN
J
Day 56
CTIP2 TBR1 SATB2 DAPI
CTIP2
TBR1
SATB2
K
Day 70
CTIP2 TBR1 DAPI
DAPI
CTIP2
TBR1
SATB2
L
Day 84
CTIP2 TBR1 DAPI
BRN2
CTIP2
TBR1
SATB2
CUX1
M
CTIP2SOX2DAPI
VZ
SVZ
CP
VZ
SVZ
CP
C1-2
C3-2
Relative layer thickness
1.00
0.75
0.50
0.25
0.00
56
84
56
84
Time (day)

Figure 3. Organization and Marker Expression of Different Progenitor Zones and Cortical Neurons of all Six Layers.

(A-C) *Schematic representations and sample images of forebrain organoids for immunostaining of NPC marker SOX2, IPC marker TBR2, and neuron marker CTIP2 at Day 28 (A), 56 (B) and 84 (C). Scale bars: 50 µm. PP: preplate; VZ: ventricular zone; MZ: marginal zone; CP: cortical plate; SVZ: subventricular zone; oSVZ: outer subventricular zone; iSVZ: inner subventricular zone.*

(D-G) *Sample images of immunostaining of oRGC markers HOPX (D), FAM107A (E) and PTPRZ1 (G), and active cell cycle marker Ki67 (F) in day 84 forebrain organoids. Note that oRGC markers are exclusively expressed within the oSVZ-like region and co-localize with NPC marker SOX2. Scale bars: 50 µm.*

(H) *Schematic representation of marker expression for cortical neurons in the mature mammalian neocortex.*

(I) *Sample images of immunostaining for preplate Cajal-Retzius cell marker REELIN and deep layer neuron markers CTIP2 and TBR1 in day 28 forebrain organoids. Scale bar: 50 µm.*

(J-K) *Sample images of immunostaining for deep layer neuron markers (CTIP2 and TBR1) and superficial layer neuron marker (SATB2) in forebrain organoids at day 56 (J) and 70 (K). Images shown in (K) are from consecutive sections for the same cortical structure. Scale bar: 50 µm.*

(L) *Sample images of immunostaining for deep layer neuron markers (CTIP2 and TBR1) and superficial layer neuron markers (SATB2, BRN2 and CUX1) in forebrain organoids at day 84. Images shown are from consecutive sections for the same cortical structure. Scale bar: 50 µm.*

(M) *Sample image showing layer specification in forebrain organoids and quantification of the relative thickness of VZ, SVZ and CP at days 56 and 84 for two iPSC lines. The VZ is defined by* $SOX2^{+}$ *NPCs densely organized in distinct radial morphology; SVZ is defined by the region with mixed populations of* $SOX2^{+}$ *NPCs and* $CTIP2^{+}$ *migrating neurons outside the VZ; CP is defined by the region outside SVZ to the pial surface with pure neuronal populations. Relative thickness is the ratio between thickness of VZ, SVZ or CP to the total thickness from ventricular to pial surfaces. For each cortical structures, three measurements were taken at 45 degree angles to obtain the mean. Values represent mean ± SEM (n ≥ 6 cortical structures from 6 organoids).*

3.3.5 - Molecular Signatures of Forebrain Organoids at Different Developmental Stages

To further compare our forebrain organoids to in vivo human brain development, we performed RNA-seq analyses of global transcriptomes from day 26, 40, 54 and 100 organoids. We compared organoid transcription profiles to published datasets from 21 different human fetal organs during the first and second trimester (Roost et al., 2015). Pearson's correlation analysis showed that organoids from all 4 time points strongly correlated with fetal brains and spinal cord, with less or no correlation with other fetal somatic tissues (Figure 4A). Further comparison with published transcriptomes from human dorsolateral prefrontal cortex samples across six stages over the life span (Jaffe et al., 2015) showed that organoids at different stages exhibited the highest correlation with fetal brain tissues, with the best correlation at day 100. These results suggested that organoid development is reminiscent of fetal human brain development at the molecular level.

To pinpoint developmental stages and brain subregion identities of forebrain organoids, we performed large-scale comparisons with transcriptome datasets of 16 different human brain regions at 11 developmental stages from the Allen Brain Atlas. Interestingly, transcriptome analyses revealed a temporal correlation between organoid development and fetal human brain development, particularly for prefrontal cortex development (Figure 4B). For example, day 26-54 organoid profiles were closer to several subregions of prefrontal cortex at 8-9 PCW, whereas day 100 organoids were more closely related to 17-24 PCW, or even 35 PCW for some subregions (Figure 4B), well into the third trimester of human fetal development.

We also identified differentially expressed genes during organoid development. These genes displayed similar trends during brain development from fetal to later stages in vivo (Figure 4C). Gene Ontology analysis revealed enrichment of many neuronal function pathways among upregulated genes (Figure 4D) and enrichment of cell cycle-related pathways among down-regulated genes. Interestingly, common gene analysis between differentially expressed genes during organoid development and risk genes for schizophrenia or autistic spectrum disorders showed significant overlap ($P < 0.001$, chi-square test; Figure 4E). Therefore, the organoid system can be used to study the functional impact of the dynamic expression of these disease risk genes in human brain development.

Together, our systematic and comprehensive transcriptome comparisons provide additional validation of forebrain organoids to resemble normal human embryonic cortical development.

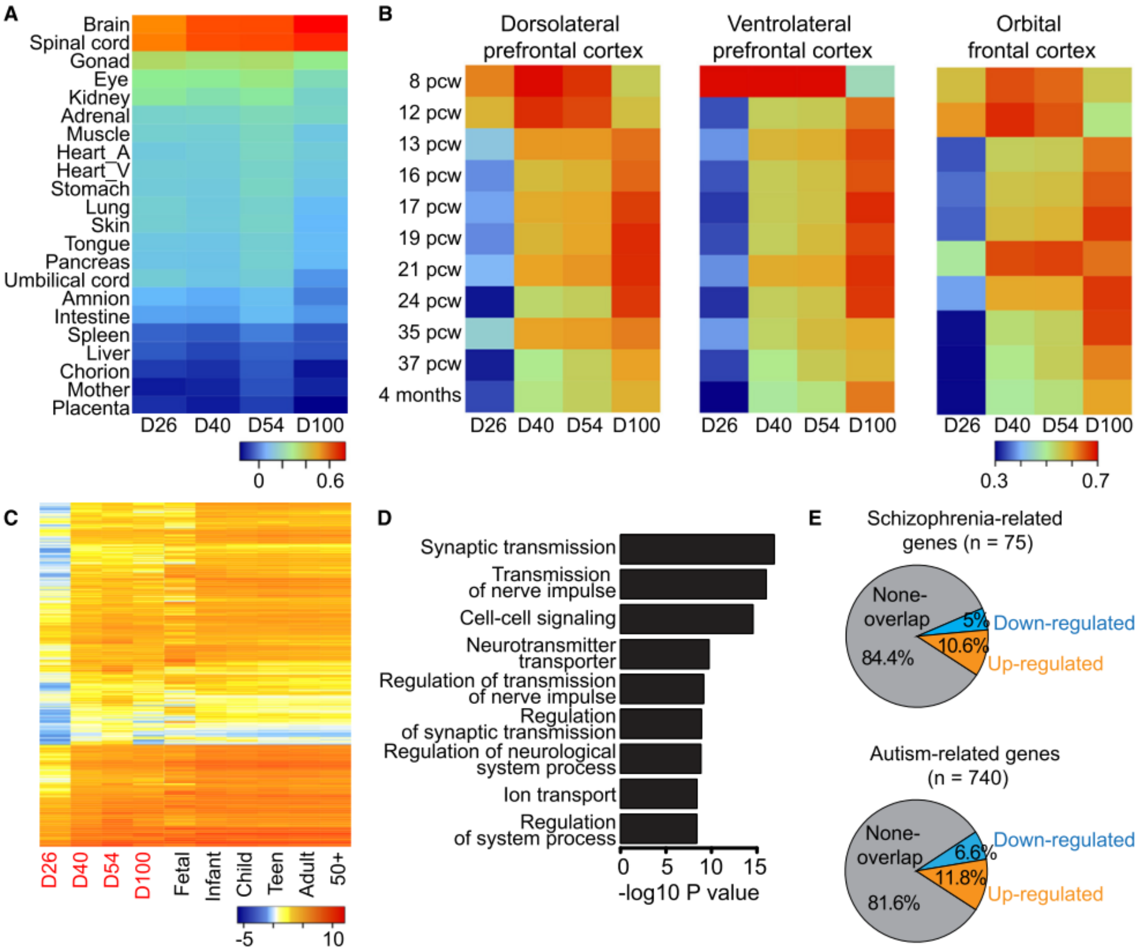
A
Brain
Spinal cord
Gonad
Eye
Kidney
Adrenal
Muscle
Heart_A
Heart_V
Stomach
Lung
Skin
Tongue
Pancreas
Umbilical cord
Amnion
Intestine
Spleen
Liver
Chorion
Mother
Placenta
D26 D40 D54 D100
0 0.6
B
Dorsolateral prefrontal cortex
Ventrolateral prefrontal cortex
Orbital frontal cortex
8 pcw
12 pcw
13 pcw
16 pcw
17 pcw
19 pcw
21 pcw
24 pcw
35 pcw
37 pcw
4 months
D26 D40 D54 D100
0.3 0.7
C
D26 D40 D54 D100 Fetal Infant Child Teen Adult 50+
-5 10
D
Synaptic transmission
Transmission of nerve impulse
Cell-cell signaling
Neurotransmitter transporter
Regulation of transmission of nerve impulse
Regulation of synaptic transmission
Regulation of neurological system process
Ion transport
Regulation of system process
0 5 10 15
-log10 P value
E
Schizophrenia-related genes (n = 75)
None-overlap
84.4%
5%
10.6%
Down-regulated
Up-regulated
Autism-related genes (n = 740)
None-overlap
81.6%
6.6%
11.8%
Down-regulated
Up-regulated

Figure 4. Correlation of Global Transcriptomes between Forebrain Organoid and Fetal Human Brain Development.

***(A)** Heatmap plot of Pearson's correlation analysis of RNA-seq datasets from forebrain organoids at days 26, 40, 54 and 100 and published datasets from 21 different human fetal organs during the first and second trimester of development (Roost et al., 2015). Shown are averaged values for biological replicates.*

***(B)** Heatmap plots of Pearson's correlation analysis of RNA-seq datasets among forebrain organoids at different stages and published transcriptome datasets of 3 different cortical subregions at 10 fetal developmental stages and 1 postnatal stage from Allen Brain Atlas (http://www.brain-map.org/).*

***(C)** Heatmap plot of gene expression dynamics from up-regulated genes between D26 and late stages of organoid development.*

***(D)** Gene Ontology analysis of upregulated genes by The Database for Annotation, Visualization and Integrated Discovery (DAVID) (Huang da et al., 2009). Nine top terms (in terms of p-values) are shown.*

***(E)** Overlap of differentially expressed genes during organoid development with known schizophrenia related risk genes (from Schizophrenia Gene Resource: (http://bioinfo.mc.vanderbilt.edu/SZGR/) and autism related risk genes (from Simons Foundation Autism Research Initiative: https://gene.sfari.org/autdb/HG_Home.do). Overlapping genes are statistically significant ($p < 0.001$, chi-square test.*

3.3.6 - Functionally Connected Cortical Neurons and GABAergic Neuronal Subtypes

To assess physiological properties of cells in organoids, we performed electrophysiological whole-cell recording in slices acutely sectioned from organoids. Recorded neurons were capable of firing trains of TTX-sensitive action potentials in response to current injection (Figure 5A). Neurons showed rectifying membrane properties, Na^+ currents, and K^+ currents in response to voltage ramps. Cells with linear membrane properties were also observed, indicating the presence of astrocytes (Figure 5B). We observed developmental changes of intrinsic properties in recorded neurons across different stages. Both Na^+ and K^+ channel currents increased over time, which was accompanied by a decrease in membrane resistance and an increase in membrane capacitance.

To visualize morphology of individual neurons, we electroporated organoids to sparsely label cells with GFP. At day 85, GFP^+ neuron exhibited complex neuronal morphology with spine-like structures in close association with $SV2^+$ puncta (Figure 5C). About 50% of cells recorded showed spontaneous excitatory postsynaptic current (sEPSC) that were sensitive to the glutamate receptor antagonist DNQX (Figure 5D). Both intrinsic properties and synaptic connectivity were similar between two iPSC clones.

One hallmark of neuronal maturation is the switch of cellular responses to GABA from depolarization to hyperpolarization (Owens and Kriegstein, 2002). This shift is due to developmentally regulated changes in intracellular Cl^- concentration, mediated by down-regulation of chloride-importing sodium-potassium-chloride co-transporter 1

(NKCC1) and up-regulation of chloride-exporting potassium-chloride cotransporter 2 (KCC2) (Ben-Ari and Spitzer, 2004). To assess whether human neurons in organoids recapitulate this switch, we performed immunohistochemistry and found that NKCC1 was expressed at both days 56 and 84, whereas KCC2 was strongly expressed in the CP at day 84 but not day 56. We further performed a functional assay to monitor Ca^{2+} rise in response to GABA-induced depolarization (Ganguly et al., 2001) (Figure 5E). Quantification showed an increase in the percentage of neurons without GABA-induced Ca^{2+} rise among all neurons that responded to glutamate over time (Figure 5F). Therefore, forebrain organoids exhibit functional features of neuronal maturation found in vivo.

Similar to our 2D differentiation protocol to direct human iPSCs towards a forebrain fate, which results in about 10% GABAergic neurons (Wen et al., 2014), we observed $GABA^{+}VGLUT^{-}$ neurons in forebrain organoids after day 84 (Figure 5G). Electrophysiological recordings in the presence of DNQX to block all glutamatergic synaptic transmission also showed spontaneous postsynaptic currents with slower kinetics (Figure 5H). Immunohistological analysis further revealed the presence of at least three major subtypes of GABAergic neurons expressing parvalbumin, nNOS or somatostatin (Figure 5I). Consistent with electrophysiological recording results (Figure 5B), we observed $S100\beta^{+}$ and $GFAP^{+}$ astrocytes in close association with surrounding neurons (Figure 5J-L). Together, these findings demonstrate that forebrain organoids contain a diverse collection of neuronal and other cell types found in developing human brains.

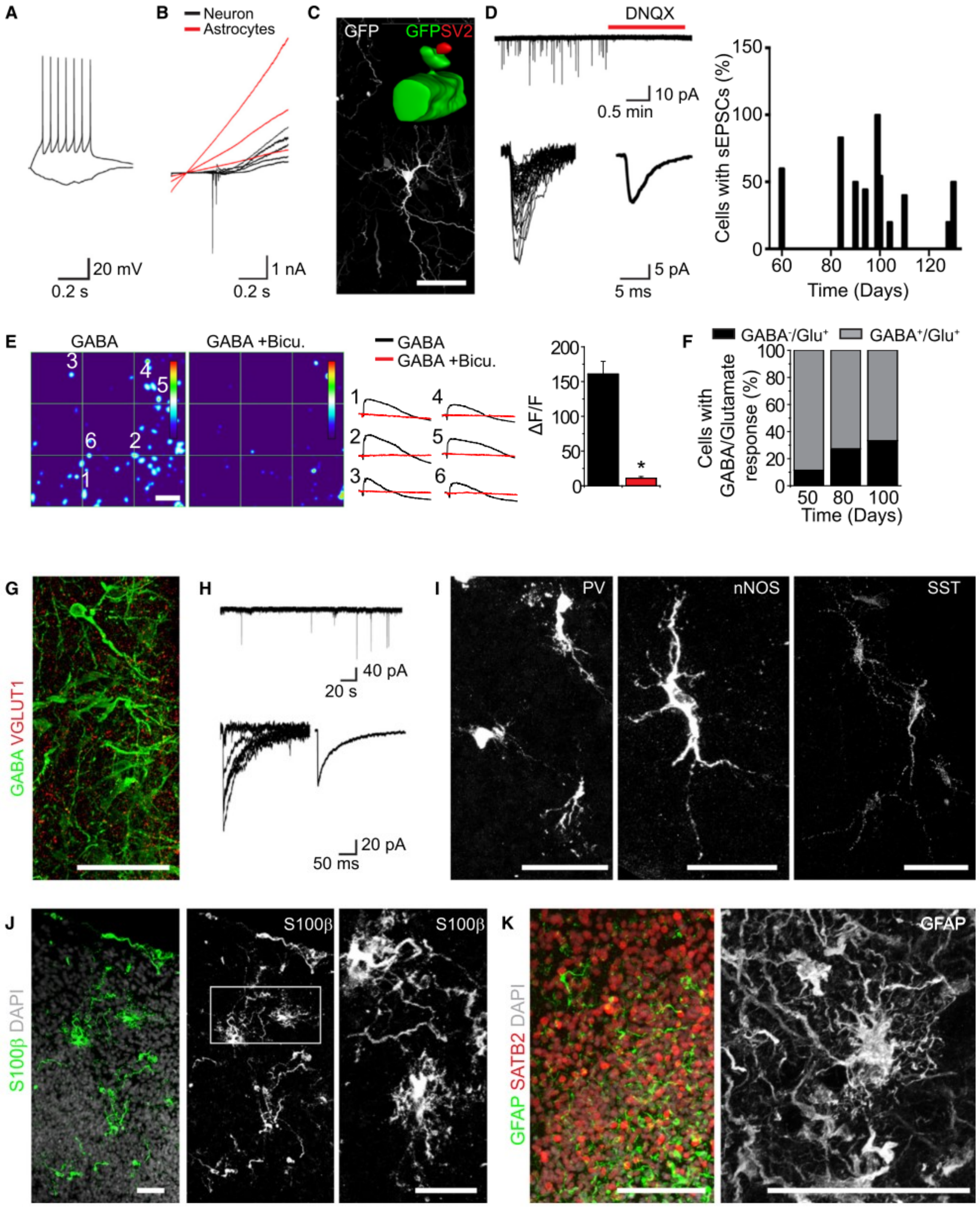
A
20 mV
0.2 s
B
Neuron
Astrocytes
1 nA
0.2 s
C
GFP
GFPSV2
D
DNQX
10 pA
0.5 min
5 pA
5 ms
Cells with sEPSCs (%)
150
100
50
0
60
80
100
120
Time (Days)
E
GABA
GABA +Bicu.
3
4
5
6
2
1
GABA
GABA +Bicu.
1
2
3
4
5
6
ΔF/F
200
150
100
50
0
*
F
GABA⁻/Glu⁺
GABA⁺/Glu⁺
Cells with GABA/Glutamate response (%)
100
80
60
40
20
0
50
80
100
Time (Days)
G
GABA VGLUT1
H
40 pA
20 s
20 pA
50 ms
I
PV
nNOS
SST
J
S100β DAPI
S100β
S100β
K
GFAP SATB2 DAPI
GFAP

Figure 5. Functional Characterization of Forebrain Organoids.

(A-D) *Electrophysiological and morphological analyses of cells in forebrain organoids. Shown in (A) are sample current-clamp traces of a neuron firing a train of action potentials in response to 10 pA of current injection. A hyperpolarizing step of -5 pA is also shown. Shown in (B) are sample voltage-clamp traces showing currents in response to a ramp protocol (- 90 mV to 110 mV). Shown in (C) is a sample image of a neuron in a day 85 forebrain organoid labeled by GFP upon electroporation. The insert shows surface rendering of a dendritic spine structure on a GFP-labeled neuron with the pre-synaptic terminal labeled by SV2 staining in red. Scale bars: 50 μm. Shown in (D, left) are sample recording traces of sEPSCs and pharmacological blockade by the glutamate receptor antagonist DNQX. Identified sEPSC events are overlaid and the average sEPSC trace is shown. Also shown in (D, right) is the summary of the percentage of cells that exhibited detectable sEPSC events in organoids of different ages.*

(E) *Calcium imaging analysis of cellular response to GABA application (10 μM). Day 100 organoids were loaded with Fluo-4. Shown in left panels are sample heat maps of GABA-induced fluorescence changes (ΔF/F) within the same region in the absence or presence of Bicuculline (Bicu. 50 μM). The color scale at the right indicates a ΔF/F range of 0 to 250%. Scale bars: 50 μm. Shown in the middle panel are calcium response curves for individual cells indicated in the heatmap. Shown in the right panel is the summary of ΔF/F in response to GABA in absence or presence of bicuculline. Values represent mean ± SEM (n = 43 neurons from 3 organoids).*

(F) *Developmental shift of the percentage of cells in forebrain organoids that exhibit calcium rise in response to GABA (10 μM) and glutamate (20 μM). Shown is the summary of percentages of cells without GABA-induced* Ca^{2+} *rise* ($GABA^-$) *among those that responded to glutamate* (Glu^+)*. Value represent mean (n = 26, 77 and 69 neurons from 3 organoids at days 50, 80 and 100, respectively).*

(G-I) *GABAergic neurons in forebrain organoids. Shown are sample images of immunostaining for GABA and VGLUT1 (G) and GABAergic neuron subtypes (I), including parvalbumin (PV)-, neuronal nitric oxide synthases (nNOS)- and somatostatin (SST)-expressing neurons. Note that* $GABA^+$ *neurons did not express the glutamatergic neuron marker VGLUT1 (G). Shown in (H) are sample recording traces of sIPSCs. Identified sIPSC events are overlaid and the average sIPSC trace is shown. Scale bars: 50 μm.*

(J-L) *Astrocytes in forebrain organoids after day 100. Shown are sample images of immunostaining for astrocyte markers S100β (J) and GFAP (L). Astrocytes were distributed among* $SATB2^+$ *cortical neurons and display complex morphologies. Scale bars: 50 μm.*

3.3.7 - Generation of Midbrain and Hypothalamic Organoids from Human iPSCs

As one application of SpinΩ is to test various culture conditions, we explored approaches to generate organoids with other brain region identities. Building upon a previously established 2D differentiation protocol for generating midbrain dopaminergic (DA) neurons (Kriks et al., 2011), we applied Sonic Hedgehog (SHH) agonists (recombinant SHH and Purmorphamine), Fibroblast growth factor 8 (FGF-8), SMAD inhibitors (SB431542 and LDN193189), and GSK3β inhibitor (CHIR99021) to induce floor plate differentiation of human iPSCs, which were then transferred to SpinΩ at day 14 (Figure 6A). At day 18, midbrain organoids showed organized neuroepithelial structures expressing NESTIN and floorplate precursor marker FOXA2, but not DA neuron marker TH, whereas very few cells expressed forebrain marker PAX6 or hypothalamus progenitor marker RAX1 (Figure 6B and S6A). At day 38, we observed numerous TH^+ DA neurons in midbrain organoids (Figure 6C). At day 56, the majority of TH^+ neurons expressed $FOXA2^+$ and dopamine transporter (DAT). In addition, midbrain organoids contained TH^+ cells that expressed midbrain DA neuron markers NURR1 and PITX3. At day 75, PITX3 was robustly expressed by TH^+ cells, suggesting specification of A9 DA neurons (Chung et al., 2005) (Figure 6D). To quantify TH and FOXA2 expression, we dissociated midbrain organoids at day 65 to plate on Matrigel-coated tissue culture plates for 5 days. Immunohistochemistry analysis showed that 95 $\pm$ 1% of cells were $FOXA2^+$ and 55 $\pm$ 4% were TH^+ DA neurons ($n = 6$; Figure 6E).

We also explored methods to generate hypothalamic organoids from human iPSCs. We initially tested a number of published protocols (Wang et al., 2015; Wataya et al., 2008) using our SpinΩ system, but differentiation was not robust and most organoids died after 30 days (data not shown). To increase efficiency and to adapt cells to SpinΩ, we first treated human iPSCs with dual SMAD inhibitors (SB431542 and LDN193189) to pre-pattern them to the neuroectodermal fate (Chambers et al., 2009) (Figure 6F). After 3 days, embryonic bodies were treated with Wnt3A, recombinant SHH and Purmorphamine to be further patterned into the hypothalamic lineage (Dale et al., 1997; Lee et al., 2006; Shimogori et al., 2010). At day 8, the majority of cells in organoids expressed NKX2.1, NKX2.2, RAX1, SOX2, NESTIN and FOXA2, markers that are consistently expressed during early hypothalamus development (Blackshaw et al., 2010; Byerly and Blackshaw, 2009; Lu et al., 2013) (Figure 6G). At day 40, peptidergic neuronal markers, including POMC, VIP, OXT and NPY (Merkle et al., 2015), were detected in organoids generated from different iPSC lines (Figure 6H). Furthermore, a subset of cell populations within the organoids expressed OTP, a homeobox protein essential for specification of hypothalamic neuronal lineages (Wang and Lufkin, 2000) at day 40, but not day 8 (Figure 6H). Together, these findings demonstrate the versatility of SpinΩ to support growth of organoids of different types.

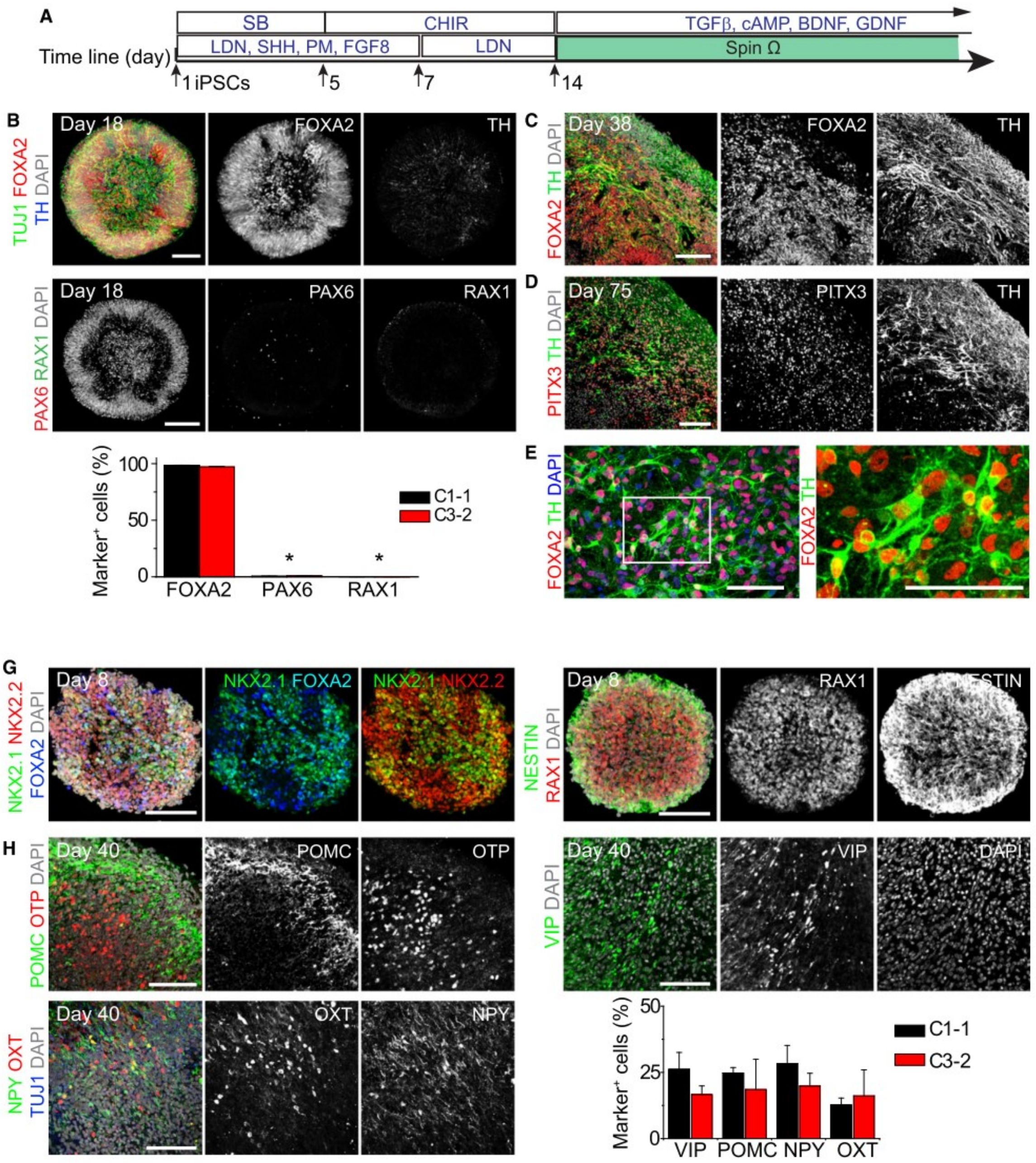
A
SB
CHIR
TGFβ, cAMP, BDNF, GDNF
Time line (day)
LDN, SHH, PM, FGF8
LDN
Spin Ω
1 iPSCs
5
7
14
B
Day 18
FOXA2
TH
TUJ1 FOXA2 TH DAPI
Day 18
PAX6
RAX1
PAX6 RAX1 DAPI
Marker⁺ cells (%)
100
50
0
FOXA2
PAX6
RAX1
*
*
C1-1
C3-2
C
Day 38
FOXA2
TH
FOXA2 TH DAPI
D
Day 75
PITX3
TH
PITX3 TH DAPI
E
FOXA2 TH DAPI
FOXA2 TH
G
Day 8
NKX2.1 FOXA2
NKX2.1 NKX2.2
NKX2.1 NKX2.2 FOXA2 DAPI
Day 8
RAX1
NESTIN
NESTIN RAX1 DAPI
H
Day 40
POMC
OTP
POMC OTP DAPI
Day 40
VIP
DAPI
VIP DAPI
Day 40
OXT
NPY
NPY OXT TUJ1 DAPI
Marker⁺ cells (%)
50
25
0
VIP
POMC
NPY
OXT
C1-1
C3-2

Figure 6. Generation of Midbrain and Hypothalamic Organoids using SpinΩ Bioreactor.

(A-E) *Midbrain organoids from human iPSCs. Shown in (A) is a schematic diagram of the protocol for generating midbrain organoids. See Experimental Procedures for detail. LDN: LDN193189 (100 nM); SHH: recombinant human Sonic Hedgehog (100 ng/ml); Pur: purmorphamine (2 µM); FGF-8: Fibroblast Growth Factor 8 (100 ng/ml). Shown in (B, top panels) are sample images of day 18 organoids showing expression of the floor plate precursor marker (FOXA2), but not the dopaminergic (DA) neuron marker TH (Tyrosine hydroxylase), forebrain progenitor marker (Pax6), or hindbrain progenitor marker (Rax1). Scale bars: 100 µm. Also shown in (B, bottom panel) is a summary of marker expression. Values represent mean ± SEM (n = 4 organoids each; *P < 0.05, Student's t-test). Also shown are sample images of immunostaining of midbrain organoids at day 38 (C) and day 75 (D) for FOXA2, TH and midbrain DA neuron maker Pituitary homeobox 3 (PITX3). Shown in (E) are sample images of immunostaining of monolayer cultures at 5 days after dissociation and plating of day 65 midbrain organoids. Scale bars: 50 µm.*

(F-H) *Hypothalamic organoids. Shown in (F) is a schematic diagram of the protocol for generating hypothalamus organoids. See Experimental Procedures for details. WNT: recombinant Wnt3a (10 ng/ml); CNTF: Ciliary neurotrophic factor (10 ng/ml); FGF-2: Fibroblast Growth Factor 2 (10 ng/ml). Shown in (G) are sample images of day 8 organoids. Shown in (H) are sample images of day 40 organoids for peptidergic neuronal markers. Scale bars: 100 µm. Also shown in (H) is a summary of quantification for peptidergic neuronal markers expression in day 40 hypothalamus organoids from 2 iPSC lines. Values represent mean ± SEM (n = 3 organoids each).*

4.4 - Discussion

We have developed a cost effective, simple to use system for 3D organoid cultures using a miniaturized multi-well spinning bioreactor, SpinΩ. The low cost of the platform, 50-fold less per condition than a standard spinning flask, allowed us to optimize protocols to generate reproducible forebrain organoids with minimized heterogeneity and variability that are amendable to quantitative analyses, and better recapitulates developing human cortex in layer formation, progenitor zone organization, and gene expression. Specifically, forebrain organoids exhibit well-developed oSVZ-like region containing NPCs that share molecular and morphological features of human oRGCs, organized neuronal subtypes of all six cortical layers and GABAergic neuronal subtypes. We further demonstrated the versatility of the SpinΩ system by developing protocols to generate organoids recapitulating characteristics of other brain regions. Finally, we applied our forebrain organoid platform for chemical compound testing and modeling ZIKV infection.

4.4.1 - SpinΩ, a Miniaturized Spinning Bioreactor for Cost-effective Organoid Culturing

Several pioneering studies showed that cerebral organoid systems offer improved growth condition for 3D tissue, leading to a more representative model of the developing human brain than had been achieved with traditional methods (Danjo et al., 2011; Kadoshima et al., 2013a; Lancaster et al., 2013; Mariani et al., 2015; Pasca et al., 2015). In particular, use of a spinning flask provides a 3D low-shear stress suspension culture with enhanced diffusion of oxygen and nutrients and supports formation of larger, continuous cortical structures (Lancaster et al., 2013). At least under our culture conditions, our direct comparison with stationary and orbital shaker cultures confirmed the beneficial effect of spinning for forebrain organoids. However, maintaining organoids in standard spin flasks is very expensive due to large volumes of culture media, making it cost-prohibitive to supplement the media with small molecules and growth factors to promote growth and differentiation of organoids. Our miniaturized spinning bioreactor SpinΩ addresses this limitation by dramatically reducing the required media volume, which allows for systematic and efficient testing of culture conditions in parallel. Moreover, SpinΩ's small footprint and compact shape reduces the incubator space required, a feature that is further highlighted by the stackable version. Importantly, many of the design parameters of SpinΩ, including number and size of wells, rotation speed, shaft angle and shape, can be customized based on specific needs. Together, the SpinΩ system provides better accessibility and higher efficiency for developing 3D tissue cultures for applications related to the brain and other organs.

4.4.2 - Advanced Features of Forebrain Organoids and Areas for Future Improvements

Compared to several pioneering cerebral organoid systems, our forebrain organoids show high reproducibility, which is critical to realize its promises as a standardized in vitro model for human cortical development. Two rounds of patterning factors effectively induce forebrain differentiation and significantly reduces brain region heterogeneity. It further reduces temporal heterogeneity of neural differentiation within forebrain organoids, allowing systematic characterization of a developmental time-course. Our proof-of-principle study with BPA demonstrates that many parameters in these organoids can be reliably quantified, therefore this platform can be used for drug testing, compound screening and disease modeling.

Importantly, forebrain organoids better recapitulates developing human cortex among multiple dimensions compared to previously reported methods. First, it produces a well-defined oSVZ-like progenitor region that is separated from the iSVZ-like region and contains a prominent oRGC-like NPC layer (Figure 3C-D), all of which are distinct features of developing human cortex that are absent in rodents and previous organoid models. The time-course of SVZ and oSVZ layer formation and progression also displays similarities with dynamic changes during human cortical development in vivo. Moreover, oRGCs in forebrain organoids express all three recently identified markers preferentially expressed by human oRGCs in vivo (Figure 3D, E, G). Second, forebrain organoids robustly generate organized cortical neurons expressing markers found in all six layers of human neocortex, including for the first time a layer of CUX1^{+} neurons destined for layer II (Figure 3L). Interestingly, the production peak of late-born neurons expressing the upper layer neuron marker SATB2 took place after day 56, coinciding with the specification and expansion of oSVZ. Because the height of oSVZ proliferation coincides in time with formation of upper cortical layers, which are particularly cell dense in human cortex, it has been suggested that the abundant oRGC population in human oSVZ is responsible for this evolutionary change (Lui et al., 2011; Marin-Padilla, 1992). In addition, plated human oRGCs after dissociation from post-mortem tissue was shown to preferentially give rise to upper layer neurons over deep layer neurons (Pollen et al., 2015). Therefore, the presence of well-developed oSVZ may be responsible for robust generation of upper layer neurons in forebrain organoids. Our electrophysiology and calcium imaging analyses revealed functional neuronal properties, active synaptic transmission and recapitulation of neuronal maturation characteristics similar to those observed in vivo, including a switch in GABA response properties. While a previous study has shown the presence of GABAergic neurons in organoids (Mariani et al., 2015), we show, for the first time, presence of GABAergic neuronal subtypes in organoids. The apparent absence of NKX2.1^{+} ventral progenitors during early differentiation suggest a possible dorsal origin of GABAergic neurons, a distinct feature of primates and humans (Jakovcevski et al., 2011; Petanjek et al., 2009; Yu and Zecevic, 2011). Lastly, large-scale comparison of global transcriptome analyses confirms that development of forebrain organoids closely correlates with human cortical development at the molecular level. Forebrain organoids with a well-developed oSVZ will significantly expand our ability to study distinct characteristics of human cortical development that cannot be represented in rodent models. Compared to studies on postmortem human tissues, forebrain organoids offer a model to investigate embryonic human cortical development as a continuous dynamic process in live cells, and allows pharmacological and genetic manipulations to investigate underlying mechanisms.

It is likely that continuous optimization can further improve the forebrain organoid system. First, depletion of nutrients and oxygen in the interior of organoids is one factor limiting our ability to model human brain development beyond the second trimester. Due to the dramatic expansion of the cortical plate, progenitor zones in forebrain organoids become gradually depleted after day 100. One potential solution may come from recently reported advances in engineering vascularized 3D tissue by endothelial cell co-cultures (Takebe et al., 2013; Takebe et al., 2014) or implementing microfluidic perfusion networks as has been proposed (Yin et al., 2016). An alternative approach would be to explore culture conditions that can accelerate the development of forebrain organoids, and produce features of late-stage cortical development with smaller overall tissue size. Second, our forebrain organoids do not contain well-defined regions representing the intermediate zone (IZ) and subplate, which play important roles in neuronal migration during cortical development (Bystron et al., 2008a). Intriguingly, a previously reported cortical neuroepithelial system showed formation of a cell-sparse IZ-like region despite lacking oSVZ (Kadoshima et al., 2013a). Third, although we have identified cortical neurons expressing markers found in all six layers of human cortex, they display only rudimentary separation and are not as six distinctly layers. Additional chemical and physical cues may be required to better regulate neuron migration and more precise localization of upper layer neurons above existing post-migratory neuron layers.

4.4.3 - Additional Future Applications

In addition to modeling brain disorders due to environmental insults or genetic causes using iPSCs derived from patients and healthy subjects, the organoid system provides a novel and renewable source of human neurons and other cell types, such as DA neurons for transplantation in models of Parkinson’s disease. Organoid growth is coupled with dramatic expansion in cell numbers. For example, embryoid bodies of around 300 μm in diameter could expand to organoids that are up to 3 mm in diameter, achieving a 1000-fold expansion in cell mass. Finally, just as the cerebral organoid methodology was inspired by self-organizing tissue organoids developed for other organs, SpinΩ has the potential to be broadly applied to other types of 3D tissue cultures beyond the nervous system, where SpinΩ’s advantages in reduced cost, increased throughput, enhanced cell survival and improved factor absorption would prove beneficial. The modular stackable version of SpinΩ allows for consistent culture conditions for numerous plates simultaneously and new possibilities for large-scale 3D tissue cultures and drug screens.

4 - Using forebrain organoids to investigate Zika virus-induced birth defects.

(This chapter was published(Qian et al., 2016). I am the first author and was involved in all aspects of the study.)

4.1 - Introduction

ZIKV, a mosquito-borne flavivirus, has been reportedly spread in over 70 countries and territories globally (CDC, 2016; Heukelbach et al., 2016). While ZIKV infection in adults usually results in mild symptoms, there has been tremendous attention drawn towards the co-occurrence of ZIKV outbreaks and an increased incidence of newborns with microcephaly, a condition where infants are born with an abnormally small head. Since the declaration of ZIKV as a global health emergency by the World Health Organization (WHO), growing evidence from clinical examinations of microcephalic fetal tissues has shown the presence of ZIKV in damaged fetal brains (Heymann et al., 2016; Mlakar et al., 2016a; Ventura et al., 2016). More recently, the United States Centers for Disease Control and Prevention (CDC) evaluated existing evidence and concluded that ZIKV causes microcephaly and other severe fetal brain defects (CDC, 2016). Live infected fetal tissues are not accessible and postmortem tissues are variable in their quality and genetic backgrounds, and clinical studies alone cannot provide sufficient insights for understanding how ZIKV causes this damage. Therefore, researchers have adopted brain organoid models to study ZIKV's cellular tropism and molecular mechanisms in controlled settings.

Brain organoids arise from the self-assembly capability of human pluripotent stem cells and is believed to be largely guided by the same intrinsic mechanism responsible for fetal development *in vivo* (Lancaster and Knoblich, 2014c). As a result, while monolayer and neurospheres usually contains relatively pure populations of one or a few cell types, brain organoids better recapitulate the composition, diversity and organization of cell types found in the developing human brain. By exposing the whole organoid to ZIKV, we could analyze and compare the efficiency with which ZIKV infects different cell types and different cell layers/regions within the same organoids. In addition, comparing to 2D differentiation protocols, brain organoids of different stages can more accurately mimic the developing trajectory of fetal brain within the first and second trimesters of pregnancy. Because these tempo-spatial transitions take place as a continuous process, researchers can examine the organoids at any time points of interest to gain insight on both short- and long-term effects of viral infection over the course of fetal brain development. Therefore, under the context of a global health emergency, such as the ZIKV outbreak, the brain organoid systems can provide direct insight into human neural development and expedite the progress of therapeutic development

4.2 - Methods

ZIKV was prepared and titered as previously described (Tang et al., 2016). Supernatant from infected mosquito cells was thawed, diluted 1:40 (0.25x) or 1:10 (1x) into forebrain organoid differentiation media, and applied directly on forebrain organoids maintained in SpinΩ. The virus inoculum was removed after a 24-hour incubation in spinning culture and replaced with fresh medium. Forebrain organoids infected at day 28 were pulsed with 10 μM EdU for 2 hours on day 42, and fixed for analysis 24 hours later. Quantitative analyses were conducted on randomly picked cortical structures captured by confocal microscope (Zeiss LSM 700). Cell proliferation was measured by density of $PH3^+$ or EdU^+ nuclei in ventricular structures similar to those described in BPA experiments. Cell death was quantified by counting cleaved caspase-3^+ nuclei over total nuclei stained by DAPI. Area of VZ and lumen, and thickness of VZ and neuronal layers were measured using ImageJ software. Overall size of organoids was measured under calibrated 4X bright field microscope.

4.3 – Results

4.3.1 - Modeling ZIKV Infection during Different Stages of Cortical Development

We performed a series of experiments to model ZIKV infection at different stages of human cortical development via exposure of forebrain organoids to ZIKV in culture medium for 24 hours in SpinΩ. Consistent with findings from our recent 2D study (Tang et al., 2016), ZIKV readily infected NPCs in day 14 forebrain organoids (Figure 7A and 8A). After 18 days, ZIKV infection resulted in an overall decrease in organoid size (Figure 8B-C). Quantitative analyses showed dramatically reduced thickness and size of ventricular structures (Figure 8D-F), likely due to significant cell death and suppression of NPC proliferation (Figure 7B-C). We also observed a significant increase in the size of lumen within ventricular structures (Figure 8F), reminiscent of dilated ventricle size in a recently reported case of a fetal brain infected with ZIKV (Driggers et al., 2016).

Next, we used two different doses of ZIKV to treat day 28 organoids, which contained both progenitor and neuronal layers (Figure 8G). Interestingly, ZIKV preferentially infected SOX2^{+} NPCs, and infected much fewer TBR2^{+} IPCs or CTIP2^{+} immature neurons when examined 4 days later (Figure 7D), suggesting specific tropism of ZIKV towards NPCs in the 3D tissue. By day 14, we observed a significantly increased number of ZIKV infected cells (Figure 8H), consistent with productive infection by ZIKV in NPCs (Tang et al., 2016). In addition to the significant reduction in overall size (Figure 8I), we also observed a ZIKV-dose-dependent reduction in both VZ and neuronal layer thickness (Figure 7E), decrease of EdU^{+} proliferating cells, and increase of activated caspase 3^+ cells (Figure 7F and 8J). Interestingly, a significant proportion of activated caspase 3^+ cells are neurons negative for ZIKVE, indicating non-autonomous toxicity effects. Therefore, ZIKV infection of early stage organoids, which corresponds to first trimester of human fetal development, leads to features resembling microcephaly.

We also assessed the effect of ZIKV on day 80 forebrain organoids (Figure 8J). After 10 days, we observed again preferential localization of ZIKV in $SOX2^+$ NPCs in VZ and oSVZ, but also in $CTIP2^+$ neurons and occasionally in $GFAP^+$ astrocytes (Figure 7G-H). The infection appeared less robust compared to earlier stages of organoids, possibly due to the limited penetration of ZIKV from the culture medium to the interior of organoids where NPCs reside. After 20 days, we observed significantly increased number of infected cells (Figure 7I). Despite dramatically expanded neuronal population and depletion of the NPC population at this time, quantification again showed significantly more SOX^+ NPCs with ZIKV than $CTIP2^+$ neurons (Figure 7I). Importantly, we observed $ZIKV^+SOX2^+HOPX^+$ cells, suggesting infection of oRGCs by ZIKV (Figure 7J).

Together, our forebrain organoid system allowed quantitatively investigation of impacts of ZIKV infection at different stages of human cortical development and our results suggest that ZIKV, once it gain access to the fetal brain, causes microcephalic-like deficits in cortical development.

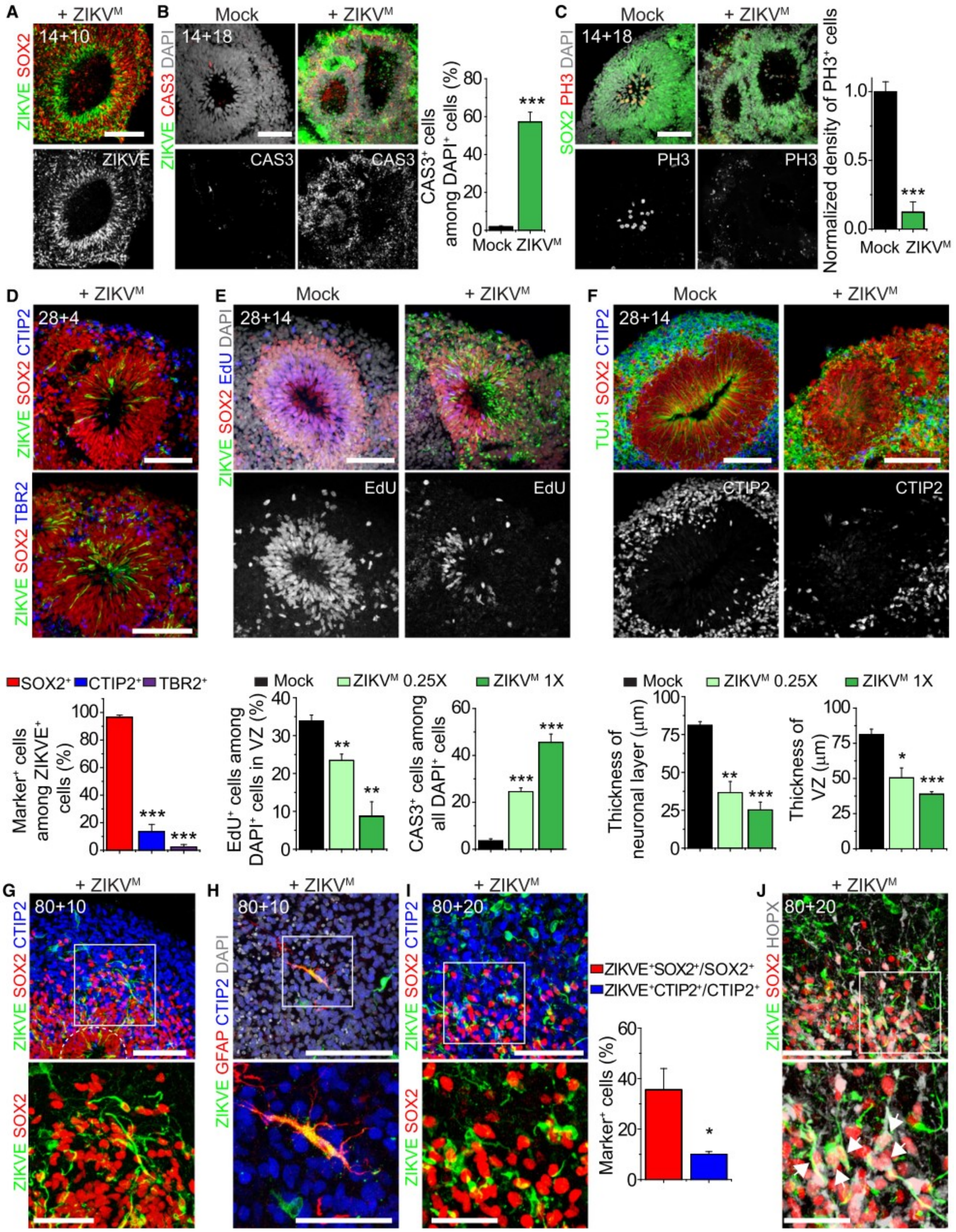
A
+ ZIKV^M
14+10
ZIKVE SOX2
ZIKVE
B
Mock
+ ZIKV^M
14+18
ZIKVE CAS3 DAPI
CAS3
CAS3
CAS3$^+$ cells among DAPI$^+$ cells (%)
80
60
40
20
0
***
Mock
ZIKV^M
C
Mock
+ ZIKV^M
14+18
SOX2 PH3 DAPI
PH3
PH3
Normalized density of PH3$^+$ cells
1.0
0.5
0.0
***
Mock
ZIKV^M
D
+ ZIKV^M
28+4
ZIKVE SOX2 CTIP2
ZIKVE SOX2 TBR2
E
Mock
+ ZIKV^M
28+14
ZIKVE SOX2 EdU DAPI
EdU
EdU
F
Mock
+ ZIKV^M
28+14
TUJ1 SOX2 CTIP2
CTIP2
CTIP2
SOX2$^+$
CTIP2$^+$
TBR2$^+$
Marker$^+$ cells among ZIKVE$^+$ cells (%)
100
80
60
40
20
0
***
***
Mock
ZIKV^M 0.25X
ZIKV^M 1X
EdU$^+$ cells among DAPI$^+$ cells in VZ (%)
40
30
20
10
0
**
**
CAS3$^+$ cells among all DAPI$^+$ cells
60
40
20
0
***
***
Mock
ZIKV^M 0.25X
ZIKV^M 1X
Thickness of neuronal layer (μm)
100
75
50
25
0
**
***
Thickness of VZ (μm)
100
75
50
25
0
*
***
G
+ ZIKV^M
80+10
ZIKVE SOX2 CTIP2
ZIKVE SOX2
H
+ ZIKV^M
80+10
ZIKVE GFAP CTIP2 DAPI
I
+ ZIKV^M
80+20
ZIKVE SOX2 CTIP2
ZIKVE SOX2
ZIKVE$^+$SOX2$^+$/SOX2$^+$
ZIKVE$^+$CTIP2$^+$/CTIP2$^+$
Marker$^+$ cells (%)
60
40
20
0
*
J
+ ZIKV^M
80+20
ZIKVE SOX2 HOPX

Figure 7. Modeling Impact of ZIKV Exposure using Forebrain Organoids.

(A) *Sample immunostaining images of forebrain organoid infected by 1X ZIKV at day 14 and analyzed at day 24 (14+10). Note localization of ZIKV envelop protein (ZIKVE) in VZ and co-localization with the NPC marker SOX2. Scale bar: 100 µm.*

(B-C) *Sample immunostaining images of forebrain organoids infected or mock-treated at day 14 and analyzed at day 32 (14+18) for the apoptosis marker activated Caspase-3 (CAS3; B), cell proliferation marker PH3 (C). Scale bars: 100 µm. Also shown are quantifications for the percentage of cells positive for CAS3 among the total number of nuclei stained by DAPI (B) and density of PH3$^+$ cells within the VZ. Values represent mean ± SEM (n = 5 organoids; *** $P < 0.0005$, Student's t-test)*

(D) *Sample immunostaining image of a forebrain organoid infected by 1X ZIKV at day 28 and analyzed at day 32 (28+4) for ZIKVE, SOX2$^+$, CTIP2$^+$ or TBR2 (top two panels; Scale bars: 100 µm). Also shown are quantifications for the percentages of SOX2$^+$, CTIP2$^+$ or TBR2$^+$ cells among the total number of ZIKVE$^+$ cells. Values represent mean ± SEM (n = 5 cortical structures from 3 organoids; *** $P < 0.0005$, Student's t-test).*

(E-F) *Forebrain organoids infected with ZIKV (at 1X or 0.25X) or mock-treated at day 28 and analyzed at day 42 (28+14). Shown in (E) are same immunostaining images and quantifications revealing reduced thickness of both VZ (SOX2$^+$ cell layer) and the neuronal layer (Tuj1$^+$ CTIP2$^+$) in forebrain organoids infected by 0.25X and 1X ZIKV. Shown in (F) are sample immunostaining images and quantification revealing reduced cell proliferation labelled by EdU and increased cell death in ZIKV-infected regions. Scale bars: 100 µm. Values represent mean ± SEM (n = 5 cortical structures from 3 organoids; **$P < 0.005$, ***$P < 0.0005$, Student's t-test).*

(G-J) *Sample immunostaining images (top) and magnified views (bottom) of forebrain organoid infected by 1X ZIKV at day 80 and analyzed at day 90 (80+10; G-H) or day 100 (80+20; I-J), showing localization of ZIKVE in VZ and oSVZ regions (G, I) and in GFAP$^+$ astrocytes (H). Arrows in (J) point to ZIKV$^+$HOPX$^+$SOX2$^+$ oRGC-like cells in the oSVZ region. Scale bars: 100 µm. Also shown in (I) are quantifications for the percentage of ZIKV$^+$ cells among the total number of SOX2$^+$ or CTIP2$^+$ cells in the whole cortical structures. Values represent mean ± SEM (n = 7 cortical structures from 5 organoids, *$P < 0.05$, Student's t-test).*

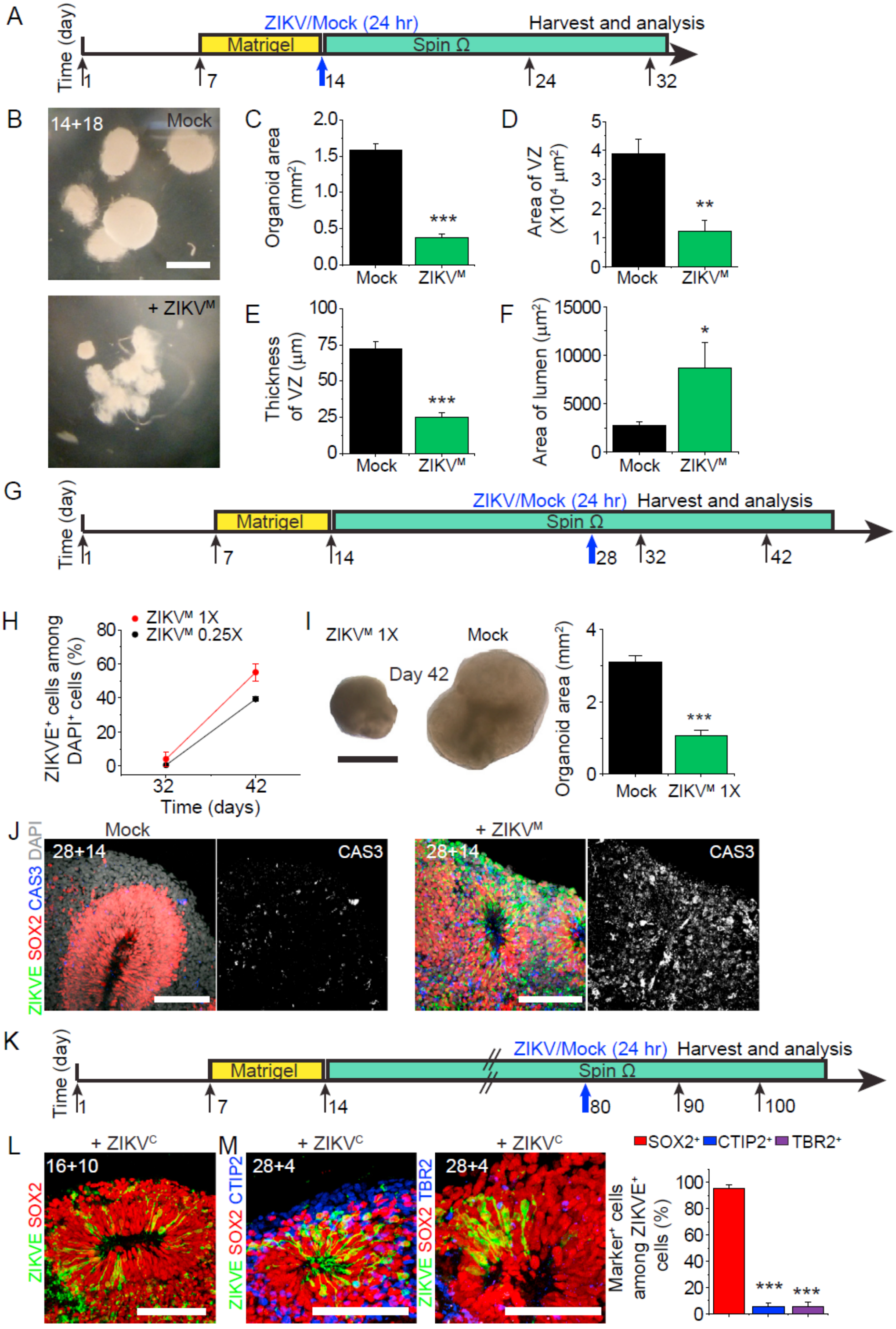
A
Time (day)
ZIKV/Mock (24 hr)
Harvest and analysis
Matrigel
Spin Ω
1
7
14
24
32
B
14+18
Mock
+ ZIKV^M
C
Organoid area (mm^2)
2.0
1.5
1.0
0.5
0.0
***
Mock
ZIKV^M
D
Area of VZ (X10^4 µm^2)
5
4
3
2
1
0
**
Mock
ZIKV^M
E
Thickness of VZ (µm)
100
75
50
25
0
***
Mock
ZIKV^M
F
Area of lumen (µm^2)
15000
10000
5000
0
*
Mock
ZIKV^M
G
Time (day)
ZIKV/Mock (24 hr)
Harvest and analysis
Matrigel
Spin Ω
1
7
14
28
32
42
H
ZIKV^M 1X
ZIKV^M 0.25X
ZIKVE$^+$ cells among DAPI$^+$ cells (%)
80
60
40
20
0
32
42
Time (days)
I
ZIKV^M 1X
Mock
Day 42
Organoid area (mm^2)
4
2
0
***
Mock
ZIKV^M 1X
J
ZIKVE SOX2 CAS3 DAPI
Mock
28+14
CAS3
+ ZIKV^M
28+14
CAS3
K
Time (day)
ZIKV/Mock (24 hr)
Harvest and analysis
Matrigel
Spin Ω
1
7
14
80
90
100
L
ZIKVE SOX2
+ ZIKV^C
16+10
M
ZIKVE SOX2 CTIP2
+ ZIKV^C
28+4
ZIKVE SOX2 TBR2
+ ZIKV^C
28+4
SOX2$^+$
CTIP2$^+$
TBR2$^+$
Marker$^+$ cells among ZIKVE$^+$ cells (%)
100
80
60
40
20
0
***
***

Figure 8. Experimental Paradigms and Additional Characterization for Effects of ZIKV Infection on Forebrain Organoids.

(A-F) *Forebrain organoids with ZIKV or mock infection (1X) at day 14 and analyzed at day 32 (14+18). Shown in (A) is a schematic diagram for the experimental paradigm. Shown in (B-C) are bright field microscopic images (B) and quantification of organoid size (C). Scale bar: 1 mm. Also shown are quantifications of VZ area (D), VZ thickness (E) and lumen size (F) measured on immunostaining images of mock and ZIKV infected organoids. Values represent mean ± SEM (n = 5 organoids; ***P < 0.0005, Student's t-test)*

(G-I) *Forebrain organoids with mock or ZIKV infection (0.25X or 1X) at day 28 and analyzed at day 32 (28+4) or day 42 (28+14). Shown in (G) is a schematic diagram for experimental paradigm. Shown in (H) is a summary of the percentage of ZIKVE^{+} cells over DAPI in cortical structures at day 32 and 42. Shown in (I) are bright field microscopic images and quantification of organoid size. Scale bar: 1 mm. Values represent mean ± SEM (n = 6 organoids; ***P < 0.0005Student's t-test).*

(J) *Sample immunostaining images of 42 (28+14) day forebrain organoids with mock or ZIKV (1X) infection showing cell apoptosis marked by CAS3.*

(K) *A schematic diagram for experimental paradigm for forebrain organoids infected at day 80.*

4.4 - Discussion

As an application of our organoid platform for disease modeling, we modeled the impact of ZIKV exposure at different stages of pregnancy. Recent clinical studies have established that ZIKV can pass through placenta to gain access to the developing fetal brain (Calvet et al., 2016; Driggers et al., 2016; Mlakar et al., 2016b). We show that among different cell types in the 3D tissue, ZIKV exhibits specific tropism towards NPCs, including oRGCs, although ZIKV could be detected in immature neurons, IPCs and astrocytes (Figure 7D, G-I). Time course analysis further shows that ZIKV infection in NPCs is productive, resulting in more infected cells over time. Therefore, even a very low dose of ZIKV exposure in vivo may lead to increasingly serious effect with time. Consistent with clinical findings that first trimester infections are the most dangerous (Cauchemez et al., 2016; Faria et al., 2016), incubating early stage forebrain organoids with ZIKV for one day leads to detrimental effects over the course of two weeks, mimicking many features of microcephaly, including decreased neuronal layer thickness and overall size as well as enlarged lumen/ventricles (Figure 7E and 8I). Mechanistically, we show increased cell death and an almost complete suppression of proliferation of infected NPCs (Figure 7F). The same ZIKV treatment of day 80 organoids, which is more complex and resembles the second trimester based on gene expression comparisons (Figure 5B), also leads to preferential infection of SOX2$^+$ NPCs, including HOPX$^+$ oRGCs (Figure 7I-J). Together, our results provide compelling evidence that, upon exposure to the fetal brain, productive and preferential infection of NPCs by ZIKV leads to characteristic features resembling microcephaly. Forebrain organoids therefore provide a quantitative experimental platform for future studies to investigate impacts of different ZIKV strains, identify cellular and molecular mechanisms, and screen for therapeutic interventions, issues that are critical to resolving the current global health emergency related to ZIKV.

5 - Sliced neocortical organoids for modeling distinct cortical neuronal layer formation.

(This chapter is under revision at Cell Stem Cell as of 12/04/2019. I am the first author and was involved in all aspects of the study.)

5.1 - Introduction

Brain organoids are human pluripotent stem cell (hPSC)-derived self-organizing three-dimensional (3D) tissues with cell types and cytoarchitectural features resembling the embryonic human brain (Lancaster and Knoblich, 2014c; Pasca, 2018; Shi et al., 2017). Recent developments in cerebral cortex organoid technologies have demonstrated striking recapitulation of human cortical development during early-to-mid gestation periods at molecular, cellular, and structural levels (Amiri et al., 2018; Bershteyn et al., 2017; Birey et al., 2017; Cugola et al., 2016; Lancaster et al., 2013; Mariani et al., 2015; Qian et al., 2016; Qian et al., 2019; Quadrato et al., 2017). However, due to a lack of functional circulation systems, the viability of cells within large cortical organoids is restricted by the limited supply of oxygen and nutrients delivered via surface diffusion (Kadoshima et al., 2013b; Kelava and Lancaster, 2016; Lancaster et al., 2017; Qian et al., 2016). Brain organoids grown as spheres in 3D suspension culture can expand up to 3 - 4 mm in diameter, but the cells in the interior suffer hypoxia, and a necrotic core forms inside. Despite methods to alleviate the diffusion limit and improve oxygen delivery, including using spinning bioreactors or gas-permeable culture plates, supplying higher oxygen in the incubator, or cutting organoids into smaller pieces, the healthy area of brain organoids is typically limited to a 300 to 400 μm deep ring along the outer surface (Kadoshima et al., 2013b; Qian et al., 2016; Sakaguchi et al., 2015; Watanabe et al., 2017). This diffusion barrier is particularly detrimental for cortical organoids because proliferating progenitor zones are organized in the interior, where they lose access to the external culture environment and eventually deplete as the outer layers thicken. The depletion of neural progenitor cells (NPCs) prohibits continuous cell generation and leads to architectural disorganization, limiting the structural development of organoids (Amiri et al., 2018; Qian et al., 2016). In contrast, the developing human embryonic neocortex continues to generate neurons and glia in the third trimester to expand the cortical volume (Bystron et al., 2008b; Fjell et al., 2015; Malik et al., 2013; Rakic, 2009; Samuelsen et al., 2003).

The increase in cortical plate (CP) thickness during human corticogenesis is accompanied by the establishment of six specialized cortical layers, a hallmark of human neocortex, which become distinctly separated by cytoarchitecture and layer-dependent expression of neuronal subtype markers by the perinatal period (Saito et al., 2011). During the mid-gestation stage, however, the upper (Layer II-IV) and deep (Layer V-VI) cortical layers are indistinguishable because the majority of CP neurons co-express markers for both upper and deep layers and the distribution of layer-dependent neuronal markers intermingles extensively (Fame et al., 2011; Ip et al., 2011; Nowakowski et al., 2017; Ozair et al., 2018; Zhong et al., 2018). A lack of accessibility to normal human embryonic tissues from the late gestation period has prevented systematic examination of this transition towards establishing separated cortical layers. Moreover, this prolonged period of co-expression of markers of different layers and neuronal subtypes is absent during rodent cortical development (Alsio et al., 2013; Britanova et al., 2008; Saurat et al., 2013), indicating the presence of human/primate-specific mechanisms controlling cortical neuron fate specification post-mitotically.

Brain organoids have demonstrated tremendous promise in recapitulating human-specific developmental features, most notably exemplified by the generation of an outer subventricular zone (oSVZ)-like progenitor layer containing outer radial glia (oRG)-like cells (Bershteyn et al., 2017; Qian et al., 2016). However, the interior hypoxia and cell death cause shrinkage of the oSVZ neurogenic niche and disruption of radial glia scaffolds in prolonged cultures, prohibiting neuronal production and proper inside-out migration required for the formation of cortical lamination (Qian et al., 2019). Thus far, despite occasionally observed rudimentary separation, no published cortical organoid models have shown consistent formation of CP structures that exhibit distinct separation between the upper and deep cortical layers. Here, we report the development of cortical organoids that overcome the diffusion limit using a slicing method, which leads to the formation of well-separated upper and deep cortical layers. We further demonstrate the utility of our system for investigation of molecular mechanisms regulating cortical neuron fate specification in normal development and psychiatric disorders.

5.2 - Methods

5.2.1 - Generation of sliced neocortical organoids

Forebrain organoid at Day 45 were collected from SpinΩ bioreactor using a cut P1000 pipette tip and immersed in melted 3% low melting point agarose dissolved in DMEM:F12 kept at 37 °C in a custom cubic mold of 1.5 cm sides. Typically, up to 10 organoids were embedded in one agarose block. Before the agarose solidify, multiple organoids were spread evenly and arranged in the same horizontal plane, with minimal spacing of 1 mm in between. The agarose blocks were placed on ice for 5-10 mins to solidify. Slicing was performed using a Leica VT 1200S vibratome in ice-cold DMEM:F12 medium at 0.1 mm/s speed and 1 mm vibration amplitude. The 500 µm-thick organoid slices were separated from the agarose by gentle pipetting. The section from the middle of an organoid were collected, while sections from the top and bottom ends were discarded. The organoid sections were transferred to 6-well plate with differentiation medium supplemented with 1% Matrigel (v/v), left to equilibrate for 1 hr in stationary culture and placed on a CO_2 resistant orbital shaker rotating at 120 rpm in the incubator. After Day 70, the medium was switched to maturation medium and organoids can be maintained for up to a year with medium change every 2 days. Repeated slicing was performed every 4 weeks after initial slicing to prevent disk-shaped SNOs from growing back to spherical or oval shape. During embedding, SNOs were carefully oriented in the agarose mold to ensure that the x-y horizontal plane is parallel to the previous slicing plane, and when necessary, the positions and orientation of SNOs were adjusted under a stereo microscope (Zeiss Discovery V8). After slicing, only one 500 μm-thick section in the middle were collected and cultured following the procedures described above. After Day 35, the time schedule for SNO cultures was followed with a flexibility range of ± 3 days. SNOs were collected using a cut P1000 pipette tip when used for analyses on the indicated age (± 3 days).

5.2.2 - Tissue preparation

Whole organoids were fixed in 4% Paraformaldehyde in Phosphate Buffered Saline (PBS) for 30 mins at room temperature. Organoids were washed 3 times with PBS and then immersed in 30% sucrose solution overnight. Organoids were embedded in tissue freezing medium and sectioned with a cryostat (Leica) at 30 μm thickness unless otherwise specified. The disk-shaped SNOs were oriented carefully in the tissue freezing medium to ensure that the x-y horizontal plane is parallel to the section plane. The first and last 5 sections for each SNO were not used for any immunohistochemistry analysis.

5.2.3 - Immunohistochemistry and microscopy

For immunostaining, cryosectioned slides were washed with PBS before permeabilization with 0.5% Triton-X in PBS for 1 hr. Tissues were blocked with blocking medium consisting of 10% donkey serum in PBS with 0.05% Triton-X (PBST) for 30 mins. Primary antibodies diluted in blocking solution were applied to the sections overnight at 4 ºC. The primary antibodies used and their dilution were summarized in the Key Resource Table. After washing with PBST for a minimum of 5 times, secondary antibodies diluted in blocking solution were applied to the sections for 1-4 hrs at room temperature or overnight at 4 ºC. Finally, sections were washed with PBST for a minimum of 5 times before mounting. Secondary anti-bodies were: AlexaFluor 488, 546, 594, or 647 -conjugated donkey antibodies (Invitrogen) used at 1:500 dilution. Images were captured by a confocal microscope (Zeiss LSM 800). Sample images were prepared in ImageJ (NIH) and Photoshop (Adobe) software.

5.2.4 - Analysis of hypoxia

Detection of hypoxic cells in unsliced organoids and SNOs was performed using Hypoxyprobe Kit (HPI). Pimonidazole HCL was added to culture medium at 200 μM working concentration, and incubated with organoids for 2 hrs before fixation for analysis. Immunochemical detection of hypoxic cells containing pimonidazole was performed following the manufacturer's instructions. SNOs and unsliced organoids were analyzed at Day 60, 110 and 140. All three dates were 2 weeks after a routine slicing for SNOs to ensure consistency. Only the cryosections in the very middle of the organoids were used for this analysis. Images were captured by a confocal microscope (Zeiss LSM 800) using the same acquisition parameters (laser intensity and gain), and "tile"/ "stitching" functions in the Zen software (Zeiss) were used when necessary. To quantify the percentage of hypoxic area in sliced and unsliced organoids, the area labeled by the hypoxyprobe were measured using ImageJ software and divided by the total organoid area marked by DAPI.

5.2.5 - Analyses of cell death

For quantification of necrotic area in SNOs and unsliced organoids, organoid cryosections were immunostained with Cleaved-Caspase-3 (Cas3) and SOX2. Only sections in the middle were analyzed. The entire organoid section was imaged using a confocal microscope, and "tile"/ "stitching" functions in the Zen software (Zeiss) were used when necessary. The necrotic area was defined as the interior portion of the organoid marked by: (1) diffusive non-cell-specific signals of Cas3 immunoreactivity; (2) absence of SOX2$^+$ cells and (3) fragmented nuclei morphology stained by DAPI. The total area and necrotic area of an organoid was manually drawn and measured using ImageJ software. For quantification of the percentage of apoptotic cells, random cortical structures outside the necrotic area were imaged under a confocal microscope at single z-plane. A randomly selected 400x400 µm area containing both the progenitor and neuronal layers was analyzed. The number of cells positive for Cas3 were counted and divided by the total cell number labeled by DAPI using ImageJ software.

5.2.6 - Analyses of Layer thickness

Analyses of progenitor zone thickness, cortical plate/subplate (CP) thickness and total thickness were performed similarly to previously described (Qian et al., 2016). Only cryosections near the middle of each organoid were used for analyses. SNOs and unsliced organoids were immunostained for SOX2, TBR2 and CTIP2. Random cortical structures were imaged under a confocal microscope and 15 µm z-stacks were projected with maximum intensity in ImageJ software. The ventricular zone (VZ) was defined by exclusive SOX2 immunoreactivity and neural tube-like morphology. The outer subventricular zone (oSVZ) was defined by the region containing mixed population of SOX2$^+$, CTIP2$^+$ and TBR2$^+$ nuclei outside the VZ. The CP was defined by the region from the boundary of the oSVZ to the outer surface containing exclusively CTIP2$^+$ nuclei. After defining the boundaries of each layer, the layer thickness was measured in the direction with maximum radial distance from the ventricular (apical) surface to the pial (basal) surface using ImageJ software. For old organoids (typically >120 day) where the VZ shrunk in size and became difficult to define morphologically, the apical surface was defined at the center of the progenitor zone. The progenitor zone thickness was the sum of VZ and oSVZ, and the total thickness was the sum of progenitor zone and CP thickness.

5.2.7 - Progenitor cell proliferation analyses

For quantification of cell proliferation, SNOs and unsliced organoids were immunostained for SOX2 and KI67. Random cortical structures were imaged using a confocal microscope. A fan-shaped region from the apical surfaces of the VZ to the boundary between the oSVZ and CP were cropped for analyses. KI67$^+$ nuclei were counted and divided by the total number of nuclei stained by DAPI in the region.

5.2.8 - EdU labeling and quantification of cell identity

SNOs at Day 70, Day 100 or Day 145 were pulsed with 10 µM EdU for 1 hr. The media was then replaced and SNOs were washed 3 times with fresh media to remove residual EdU. After 7 days, SNOs were fixed for immunohistochemistry and EdU detection using Click-iT® EdU Alexa Fluor® 488 Imaging Kit according to the manufacturer’s manual. Cortical structures were randomly imaged under a confocal microscope at the single z-plane. Each EdU-positive nucleus in the insets were traced in Photoshop software (Adobe), and manually assigned pseudo-colored to indicate whether it expresses SATB2 or CTIP2, or both.

Day 95 SNOs were pulsed with 10 µM EdU for 24 hr and analyzed 3 or 7 days later. The number of EdU$^+$ expressing SOX2, SATB2, and TBR2 were counted in ImageJ software. The positions of all EdU$^+$ nuclei were manually marked using the “Cell Counter” plugin in ImageJ. Their y-coordinates on the image were recorded and normalized to the total thickness from apical to basal surfaces of cortical structures to measure their relative laminar positions. The frequency distributions of the relative vertical positions in 11 evenly divided bins for each marker were calculated and plotted in Prism software (GraphPad).

Day 95 SNOs were pulsed with 10 μM EdU for 24 hr and analyzed 28 days later (Day 123). The organoids were treated with DMSO, IWR or CHIR from Day 103 to Day 123. The number of EdU$^+$ expressing TBR1, SATB2, and co-expressing both were counted in ImageJ software. The ratio of co-expression was calculated by [#TBR1$^+$ SATB2$^+$ EdU$^+$ nuclei / #SATB2$^+$ EdU$^+$ nuclei] and by [#TBR1$^+$ SATB2$^+$ EdU$^+$ nuclei / #EdU$^+$ nuclei]. Each EdU-positive nucleus in the insets were traced in Photoshop software (Adobe), and manually assigned pseudo-colored to indicate whether it expresses SATB2 or TBR1, or both.

5.2.9 - Analyses of cortical neuron distribution

SNOs were immunostained for SATB2 and TBR1 and random cortical structures were imaged on a confocal microscope at the single z-plane. From the pial surface, radial columns of 100 μm width and 200-500 μm length covering the full thickness of the CP layer were cropped for analyses. The positions of all SATB2$^+$, TBR1$^+$ and double-positive nuclei were separately marked using the “Cell Counter” plugin in ImageJ. Their y-coordinates on the image were recorded and normalized to the full thickness of the CP to measure their relative laminar positions in the CP. The frequency distributions of the relative vertical positions in 11 evenly divided bins for each marker were calculated and plotted in Prism software (GraphPad). The ratio of co-expression was calculated by [#TBR1$^+$ SATB2$^+$ nuclei / #SATB2$^+$ nuclei]. For highlighting the differences between the relative cell numbers of SATB2$^+$ nuclei and TBR1$^+$ nuclei within each bin, heatmap was plotted in Prism software to represent [(normalized SATB2$^+$ nuclei #) – (normalized TBR1$^+$ nuclei #)], with red indicating a positive value (more SATB2) and blue indicating a negative value (more TBR1). The analyses for RORB and CTIP2, and additional neuron markers were performed similarly. Kolmogorov-Smirnov tests were performed using a web-based tool (http://www.physics.csbsju.edu/stats/KS-test.n.plot_form.html). The relative locations of all marker$^+$ nuclei were used to plot the cumulative distribution curve and calculate the P-values.

For the β-Catenin agonist/antagonist treatment experiments, CHIR99021 or IWR-1-endo were added to the maturation medium at the specified concentrations to SNOs at Day 100 with medium change every 2 days. After 20 days (Day 120), random SNOs were collected for analysis while the remaining SNOs were washed and cultured in fresh medium without the drugs. The remaining SNOs were collected at Day 150 for analyses.

5.2.10 - Viral infection

For sparse labeling of radial glia cells and astrocytes with GFP, AV-CMV-GFP adenovirus (Vector Biolabs, titer = 1×10^{10} PFU/ml) were added into maturation medium at 1:2000 dilution, and incubated with SNOs for 24 hrs before being washed away. SNOs were analyzed 3- 5 days after exposure to virus, as indicated in figure legends, and immunohistochemistry against GFP was used to enhance the fluorescence signals.

5.2.11 - Single-nucleus RNA-seq and data analysis

Single-nucleus RNA sequencing was performed following the SPLiT-seq method with minor modifications (Rosenberg et al., 2018). Nuclei isolated from fresh organoids was performed as previously described (Su et al., 2017). Briefly, Tissue were minced with a razor blade and homogenized using a tissue grinder in a 1 ml of HB buffer (1 mM DTT), 0.15 mM spermine, 0.5 mM spermidine, EDTA-free protease inhibitor, 0.3% IGEPAL-630, 0.25 M sucrose, 25 mM $MgCl_2$, 20 mM Tricine-KOH) for 5 to 10 strokes, then filtered through a 40 μm strainer, underlayer with a cushion buffer (0.5 mM $MgCl_2$, 0.5 mM DTT, EDTA-free protease inhibitor, 0.88 M sucrose) and centrifuged at 2800g for 10 minutes in a swinging bucket centrifuge at 4 ºC. Nuclei were collected as pellets.

Nuclei were then centrifuged for 3 mins at 500g at 4 ˚C. The pellet was resuspended in 1 ml of cold PBS-RI (1x PBS + 0.05U/μl RNase Inhibitor). The nuclei were passed through a 40 μm strainer. 3 ml of cold 1.33% formaldehyde solution was then added to 1 ml of cells. Nuclei were fixed for 10 mins before adding 160 μl of 5% Triton X-100. Nuclei were then permeabilized for 3 mins and centrifuged at 500g for 3 mins at 4 ˚C. Nuclei were resuspended in 500 μl of PBS-RI before adding 500 μl of cold 100 mM Tris-HCl pH 8. Then, nuclei were spun down at 500g for 3 mins at 4 ˚C and resuspended in 300 μl of cold 0.5 X PBS-RI. Finally, nuclei were again passed through a 40 μm strainer and then counted on a hemocytometer, diluted to 1,000,000 cells/ml.

mRNA from single nuclei were tagged 3 rounds with barcoded primers, with in-cell ligations using T4 DNA ligase. Plates were incubated for 30 mins at 37 ºC with gentle sharking (50 rpm) to allow hybridization and ligation to occur. The ligation products were purified with Dynabeads MyOne Streptavidin C1 beads. After washing beads once with 10 mM Tris and 0.1% Tween-20 solution and once with water, beads were resuspended into a solution containing 110 µl of 2X Kapa HiFi HotStart Master Mix, 8.8 µl of 10 µM stocks of primers BC_0062 and BC_0108, and 92.4 µl of water. PCR thermocycling was performed as follows: 95 °C for 3 mins, then five cycles at 98 °C for 20 seconds, 65 °C for 45 seconds, 72 °C for 3 mins. After these five cycles, Dynabeads beads were removed from PCR solution and EvaGreen dye was added at a 1X concentration. Samples were again placed in a qPCR machine with the following thermocycling conditions: 95 °C for 3 mins, cycling at 98 °C for 20 seconds, 65 °C for 20 seconds, and then 72 °C for 3 mins, followed by a single 5 mins at 72 °C after cycling. Once the qPCR signal began to plateau, reactions were removed.

PCR reactions were purified using a 0.8X ratio of KAPA Pure Beads and cDNA concentration was measured using a qubit. For tagmentation, a Nextera XT Library Prep Kit was used. 600 pg of purified cDNA was diluted in water to a total volume of 5 µl. 10 µl of Nextera TD buffer and 5 µl of Amplicon Tagment enzyme were added to bring the total volume to 20 µl. After mixing by pipetting, the solution was incubated at 55°C for 5 mins. A volume of 5 µl of neutralization buffer was added and the solution was mixed before incubation at room temperature for another 5 minutes. PCR was then performed with the following cycling conditions: 95 °C for 30 seconds, followed by 12 cycles of 95 °C for 10 seconds, 55 °C for 30 seconds, 72 °C for 30 seconds, and 72 °C for 5 mins after the 12 cycles. 40 µl of this PCR reaction was removed and purified with a 0.7X ratio of SPRI beads to generate an Illumina-compatible sequencing library.

Sequencing was performed with 50 bp paired end sequencing by Illumina NextSeq 550. Data processing was preprocessed using Drop-seq-1.13 (Macosko et al.,

2015) with modifications. Briefly, after mapping the reads to the human genome (hg38, Gencode release V28), both exonic and intronic reads mapped to the predicted strands of annotated genes were retrieved for the cell type classification. Uniquely mapped reads were grouped by cell barcode. To digitally count gene transcripts, a list of UMIs in each gene, within each nucleus, was assembled, and UMIs within ED = 1 were merged together. The total number of unique UMI sequences was counted, and this number was reported as the number of transcripts of that gene for a given nucleus. Raw digital expression matrices were generated for the 1 sequencing runs. The raw digital expression matrices were combined and loaded into the R package Seurat (v 2.3.4) (Butler et al., 2018). For normalization, UMI counts for all nuclei were scaled by library size (total UMI counts), multiplied by 10,000 and transformed to log space. As a result, 6888 nuclei were kept for further analysis.

For clustering, the highly variable genes were identified using the function FindVariableGenes with the parameters: x.low.cutoff = 0.01, x.high.cutoff = 3 and y.cutoff = 0.8 in Seurat, resulting in 2,677 highly variable genes. The expression level of 2,677 genes in the nuclei was scaled and centered along each gene, and was conducted to the PCA. We selected different cut-offs of the number of PCs and empirically found that downstream clustering analyses were optimized when using 25-PCs cutoff. First 25 PCs were selected and used for two-dimension t-distributed stochastic neighbor embedding (tSNE), implemented by the Seurat software with default parameters. Based on the tSNE map, 12 clusters were identified using the function FindCluster in Seurat with the resolution parameter of 0.6. To identify marker genes, differential expression analysis was performed by the function FindAllMarkers in Seurat with likelihood-ratio test.

Differentially expressed genes that were expressed in at least 10% cells within the cluster and with a fold change more than 0.5 (log scale) were considered to be marker genes.

To compare cell-type classifications between organoid data and single-cell RNA-seq data of second trimester human fetal prefrontal cortex, we first downloaded the raw UMI count matrix from Zhong et al. 2018 (Zhong et al., 2018). Using identical clustering parameters in Seurat defined above for the organoid analysis, we identified 11 clusters in the human fetal cortex dataset that were annotated based on the expression and enrichment of known biologically-relevant marker genes. Using the R package ClustifyR, we converted the fetal cortex dataset Seurat object into a cluster-specific average expression matrix using the function “use_seurat_comp" and considered only the highly variable genes in the output expression matrix. Using the function clustify in clustifyR with the argument compute_method = “pearson”, we computed the cluster-specific Pearson correlation coefficients between the organoid dataset and the Zhong et al. average expression matrix.

To compare the astroglial cells in SNOs to fetal and postnatal human primary astrocytes, we obtained bulk RNA-seq data sets from a published study (Zhang et al., 2016). Differential Expression analysis was performed using edgeR (v2.15.0), from which we generated two lists of top 50 genes highly expressed by fetal and postnatal astrocytes. The relative expressions of these genes were plotted for the single nuclei in AG cluster from our SNO dataset.

5.2.12 - Whole-cell recording in SNO slices

SNOs were sliced into 200 μm thick section on a vibratome following procedures described above. Slices were placed in maturation medium in the incubator to recover for 30 mins and then transferred into a recordings chamber perfused with ACSF solution consisted of 130 mM NaCl, 3 mM KCl, 1.25 mM NaH_2PO_4, 26 mM $NaHCO_3$, 10 mM glucose, 1 mM $MgCl_2$, and 2 mM $CaCl_2$ (pH 7.2–7.4 when saturated with 95% O_2/5% CO_2). The osmolarity of all solutions was 305–315 mOsm. Slices were viewed using infrared differential interference contrast optics under an upright microscope (Slice Scope Pro, Scientifica) with a 40x water-immersion objective. Whole-cell postsynaptic patch-clamp recordings were made using glass pipettes of 4–8 MΩ resistance, filled with an internal recording solution of the following (in mM):145 K-Gluconate, 2 $MgCl_2$, 0.1 BAPTA, 2.5 KCl, 2.5 NaCl, 10 HEPES, 0.5 GTP. Tris, 2 Mg-ATP, 2 QX-314, pH: 7.2, 280–290 mOsm. In combination with the electrophysiological recordings we added 0.2% biocytin to the internal solution in order to label the patched neurons. Recordings were digitized at 20 kHz with Digidata 150A (AxonInstruments/Molecular Devices UnionCity, CA). Access resistance and leak currents were monitored and data were discarded if either parameter changed by >25% over the course of data acquisition. Spontaneous excitatory postsynaptic potentials currents (sEPSCs) were recorded at a holding potential of -70 mV for 10 mins. Data were analyzed off-line using Clampfit (Molecular Devices) and Prism 7.0 (GraphPad).

5.2.13 - Extracellular recording and analyses

Intact SNOs were transferred from maturation medium to BrainPhys neuronal medium (Bardy et al., 2015) supplemented with SM1, 10 ng/ml GDNF, 10 ng/ml BDNF and 1X Penicillin/Streptomycin and cultured for at least 7 days prior to the recordings. Day 170 ± 5 SNOs were randomly selected and transferred to a Slotted Bath Oocyte Recording Chamber (Warner Instruments) containing BrainPhys medium. Throughout the recording, SNOs were constantly perfused with medium (roughly 2 ml/min) heated using a temperature controller (Warner Instruments) to maintain a constant temperature of 37 ºC (± 2 ºC) in the recording chamber. A 4-shank, 64-channel, Buzsaki style electrode (E-Series, Cambridge NeuroTech; 300 µm electrode coverage, 250 µm shank spacing) was slowly inserted into the SNO using a micromanipulator (Kopf) until all contacts were in the SNO. Wide bandwidth signals from the electrodes were amplified using a headstage (Neuralynx), digitized with a Digital Lynx 4SX control system (Neuralynx) at 32 kHz, and bandpass filtered at 0.1 to 9 kHz with Cheetah acquisition and recording software (Neuralynx). In parallel, electrode sites were artificially grouped into tetrodes and multi-unit activity was visualized on each tetrode online in the Cheetah software. Briefly, signals from each electrode site were filtered from 0.6-6 kHz online using a tap finite impulse response (FIR) filter, and a threshold was set (20-25 µV in our setup) to be just above noise levels in the system. Anytime a signal crossed the user-defined threshold value, the next inflection point in the filtered signal was found and set as the alignment point. A 1 ms recording (comprising of 32 samples) from all 4 electrodes that made up the tetrode was obtained such that the sample alignment point made up the 8th of 32 samples. Once multiunit activity was observed in the Cheetah software, a baseline recording of at least 20 mins was obtained and stored for later analysis.

Single unit clusters were initially isolated from the 1 ms filtered, thresholded recordings using an unsupervised masked expectation-maximization (EM) algorithm that uses principle component analysis of spike features to sort spikes (KlustaKwik) (Kadir et al., 2014). Clusters were further refined by merging or hand-cutting output clusters from KlustaKwik based on differential spike shape between electrodes within a tetrode using SpikeSort3D software (Neuralynx). Once single units were separated, data was imported into Matlab software (MathWorks) or NeuroExplorer software (Plexon) and analyzed using custom and built-in routines. Inter-spike interval histograms (20 bins per decade) and auto-correlograms (bin size = 5 ms) were created to visualize interactions within neurons, and cross-correlograms (bin size = 5 ms) were created to visualize interactions between different neurons.

5.2.14 In vitro induction of cortical folding using ECM factors

The induction of wrinkles in the CP in slice-cultured SNOs was performed following published methods for human cortical slices with some modifications (Long et al., 2018). SNOs at Day 95, 110 or 125 were further sliced into 200 µm thick sections using a vibratome following similar procedures described above. Each section was cut in half at the midline with a scalpel to mimic the shape of an organotypic cortical slice used in the published study (Long et al., 2018). Sections were resuspended in a human collagen I-based hydrogel supplemented with 5 µg/mL recombinant human HAPLN1 and 5 µg/ml recombinant human lumican for the “LHC” condition, the equivalent volume of PBS was added to the hydrogel solution for the control condition. Droplets of hydrogel solution each containing one SNO section was placed on a glass-bottom petri dish (Matek) and incubated in the incubator for 30 mins before 3 ml of maturation medium was added to the dish. The embedded sections were then cultured in the stationary culture for an addition 2 to 4 days before analyses. Fixed sections were cryosectioned in the parallel direction for immunohistochemistry analyses. The CP of SNO sections was imaged using a confocal microscope and the gyrification index was calculated by [inner length/ outer length].

5.2.15 - Transcriptomic analyses of iPSC-derived neurons

Previously published RNA sequencing data from our group (Wen et al., 2014) on cortical neurons derived from the same D2 and C3 iPSC lines used in the current study was re-analyzed to evaluate the differences in the WNT/β-Catenin signaling pathway genes in relatively pure cortical neuron populations. Reads covering gene coding regions were counted with BEDTools and count data were analyzed for differential expression using edgeR (v2.15.0). The list of WNT pathway related genes was obtained from KEGG pathway (https://www.genome.jp/kegg/pathway/hsa/hsa04310.html).

5.2.16 - QUANTIFICATION AND STATISTICAL ANALYSIS

Individual organoids are treated as biological replicates, unless otherwise indicated in the Figure Legends. Data are presented as mean ± S.E.M. or mean ± S.D., unless otherwise indicated in the Figure Legends. Statistical analyses were performed using the Student’s t-test in Excel or Prism software. Significance was defined by P-value < 0.05. Organoid samples were randomly taken from the culture for experiments and analysis. Sample sizes are determined empirically. The sample sizes are designed to account for the variability between organoids and human iPSC cell lines and match current standards in human brain organoid-related studies. Other statistical details of experiments can be found in the Figure Legends. Data analyses comparing control and disease individual-derived organoids were performed blindly. Data analyses comparing sliced and unsliced organoids were not performed blindly because the visual difference between the two group is striking, and blinding is not possible to an informed researcher. No data was excluded.

5.3 - Results

5.3.1 - Slicing Method Resolves Interior Hypoxia and Reduces Cell Death in Cortical Organoids

In order to generate cortical organoids to model late-stage developmental features, such as the formation of distinct upper and deep cortical layers, we aimed to sustain neurogenesis and support the expansion of cortical structures over long-term cultures. We reasoned that the diffusion limit is inevitable if the organoid is cultured as a sphere without functional circulation systems. Therefore, we developed a precisely controlled slicing method to "trim" the organoid into a disk shape and expose the interior to the external culture environment (Figure 9A). We followed our previously established forebrain organoid protocol to Day 45 (Day 0 refers to when human iPSC colonies were detached to form embryoid bodies), when organoids have formed large ventricular structures and organized radial glia scaffolds (Qian et al., 2018). The forebrain organoids were then embedded in low-melting-point agarose and sectioned into 500 μm-thick slices using a vibratome (Figure 9A). Organoid slices came off the agarose after sectioning spontaneously or with gentle pipetting, and were collected and transferred to a 6-well plate and cultured on an orbital shaker. From a spherical organoid with 1.5 mm diameter, the one or two slices in the middle plane were kept for culture. These disk-shaped organoids received oxygen and nutrients by diffusion through the exposed top and bottom surfaces, permitting growth in both horizontal (x-y) and thickness (z) directions while maintaining the organization of cortical structures (Figure 9B-C). To keep the organoid thickness under the diffusion limit over the course of long-term culture, they were repeatedly sliced to 500 µm every 4 weeks in the parallel plane to the first slicing. From Day 60 to Day 140, the slicing method substantially reduced the pronounced interior hypoxia present in unsliced organoids, as revealed by hypoxic cell detection using a pimonidazole-based probe assay (Varia et al., 1998) (Figure 9D-E). The 500 µm section thickness was larger than the diameter of most ventricular structures formed within organoids, allowing the ventricular zone (VZ) to maintain intact adherens junctions at the apical surface (Figure 9F). Compared to unsliced forebrain organoids, these sliced neocortex organoids (hereafter referred to as SNOs) showed a drastically reduced necrotic area size, which did not increase over time. Moreover, this approach also significantly reduced apoptotic cells in the outer (non-necrotic) regions (Figure 9F-G).

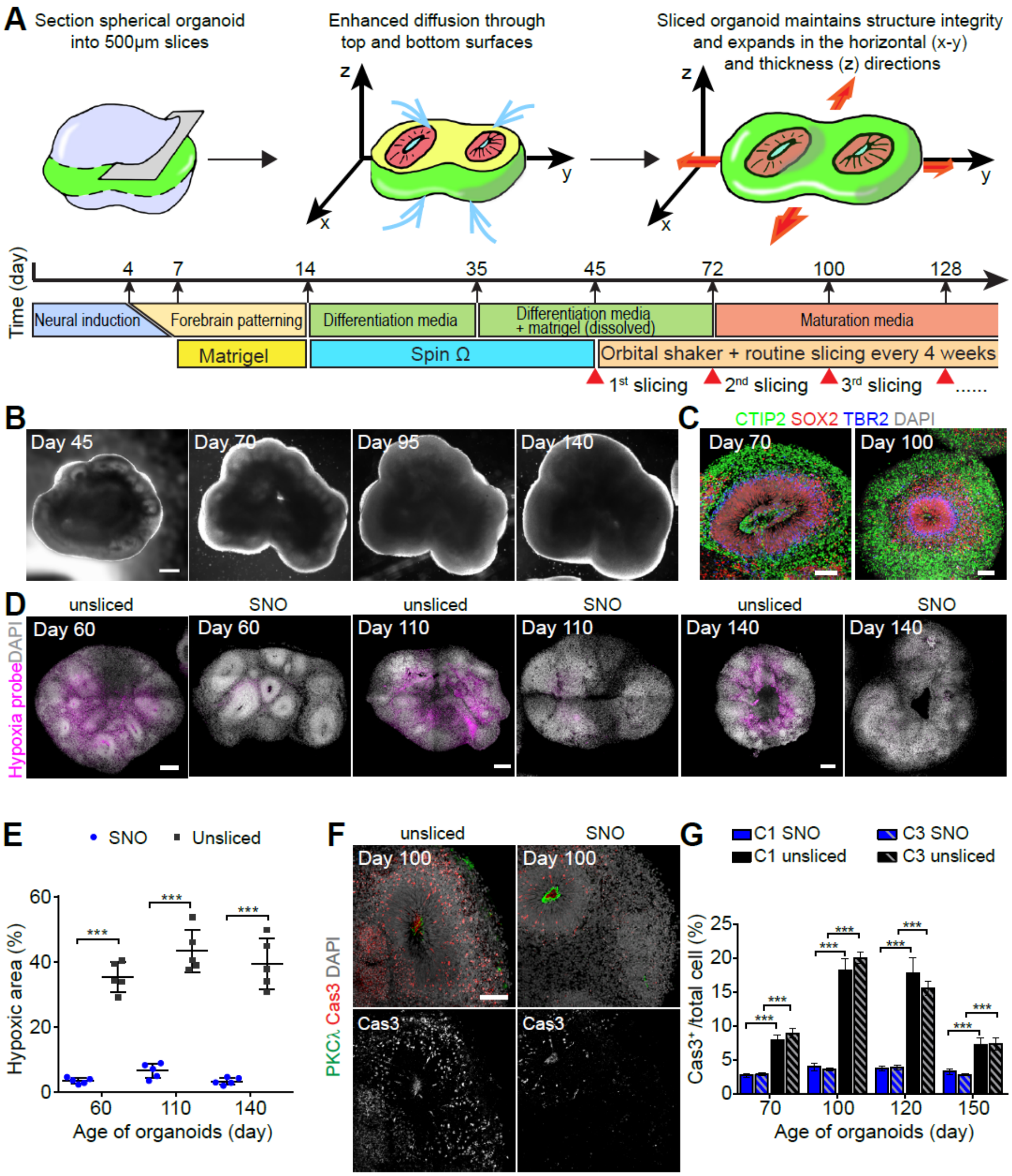
A
Section spherical organoid into 500µm slices
Enhanced diffusion through top and bottom surfaces
Sliced organoid maintains structure integrity and expands in the horizontal (x-y) and thickness (z) directions
z
x
y
Time (day)
4
7
14
35
45
72
100
128
Neural induction
Forebrain patterning
Differentiation media
Differentiation media + matrigel (dissolved)
Maturation media
Matrigel
Spin Ω
Orbital shaker + routine slicing every 4 weeks
1st slicing
2nd slicing
3rd slicing
......
B
Day 45
Day 70
Day 95
Day 140
C
CTIP2 SOX2 TBR2 DAPI
Day 70
Day 100
D
Hypoxia probe DAPI
unsliced
SNO
Day 60
Day 60
Day 110
Day 110
Day 140
Day 140
E
SNO
Unsliced
Hypoxic area (%)
0
20
40
60
***
60
110
140
Age of organoids (day)
F
PKCλ Cas3 DAPI
unsliced
SNO
Day 100
Day 100
Cas3
Cas3
G
C1 SNO
C1 unsliced
C3 SNO
C3 unsliced
Cas3+ /total cell (%)
0
5
10
15
20
25
***
70
100
120
150
Age of organoids (day)

Figure 9. Sliced Neocortical Organoid (SNO) Method Reduces Cell Death by Resolving Interior Hypoxia

(A) *Schematic illustration for the SNO protocol and culture timeline.*

(B) *Sample bright-field images of an SNO captured at Day 45, 70, 95 and 140. Day 0 refers to when iPSC colonies were detached to form embryoid bodies. Scale bar, 500 µm.*

(C) *Sample immunostaining confocal images of SNOs showing the maintenance of cortical structures after slicing. Scale bars, 100 µm.*

(D and E) *Hypoxia assay comparing unsliced organoids and SNOs using a pimonidazole-based hypoxia probe. Sample tiling confocal images for unsliced organoids and SNOs at Day 60, 110 and 140 show hypoxic cells in purple, and DAPI in white (D). Scale bars, 200 µm. Images at the same date are shown at the same scale. Shown in (E) is the quantification of the percentage of hypoxic area over total organoid area. Bar values represent mean ± S.D. (n = 5 organoids; ***p < 0.0005, Student's t test).*

(F and G) *Analyses of apoptotic cell death in SNOs and unsliced organoids. Shown are sample immunostaining confocal images for apoptosis marker cleaved caspase-3 (Cas3) and adherens junction marker PKCλ (F), and quantification of apoptotic cell death within the non-necrotic region (G). Scale bar, 100 µm. Values represent mean ± S.E.M. (n ≥ 10 and 5 organoids for SNOs and unsliced organoids, respectively; ***p < 0.0005, Student's t test).*

5.3.2 - SNO Method Sustains Neurogenesis and Radial Migration of New-born Neurons

Over long-term culture and repeated slicing, SNOs continued to grow. At Days 100 and 150, the oSVZ-like structures contained a large population of HOPX$^+$ oRG-like NPCs with radially aligned basal processes contacting the pial surface, and expanded to several folds larger than the VZ, similar to human embryonic cortex in the second trimester (Lui et al., 2011) (Figure 10A). The oSVZ also contained abundant TBR2$^+$ intermediate progenitor cells (IPCs) committed to glutamatergic neuron neurogenesis (Figure 10B). In contrast, both KI67 and TBR2 were sparsely detected in unsliced organoids by Day 150, suggesting depletion of neurogenic progenitors (Figure 10A-B). Quantitative analysis also showed that progenitor proliferation was sustained steadily in SNOs and substantially increased over unsliced organoids at Days 120 and 150 (Figure 10C). The size of progenitor zones continued increasing in SNOs, unlike the shrinkage seen in unsliced organoids (Figure 10D). Sparse labeling using adenovirus expressing GFP showed that the majority of radial glia cells expressed multiple human oRG markers (Pollen et al., 2015) and exhibited the hallmark unipolar morphology of oRGs (Figure 10E). Birth-dating of newborn cells using 5-ethynyl-2'-deoxyuridine (EdU) pulse-chase labeling for 7 days confirmed sustained production of cortical neurons (Figure 10F). At 3 days post-labeling at Day 95, the majority of EdU$^+$ cells were SOX2$^+$ and located within the oSVZ (Figure 10H-J). At 7 days post-labeling, post-mitotic cells retaining strong EdU reactivity moved up into the CP and expressed cortical neuron marker SATB2, while cycling progenitors expressing SOX2 and TBR2 underwent multiple divisions and their EdU immunoreactivity became undetectable due to dilution (Figure 10H-J). Moreover, many EdU$^+$ cells found within the oSVZ also expressed PRDM8, a marker for migrating neurons in the cerebral cortex (Inoue et al., 2014; Komai et al., 2009). PRDM8 was more abundantly detected in the oSVZ than in the CP, suggesting that the majority of neurons in the CP have completed radial migration and reached their designated laminar positions.

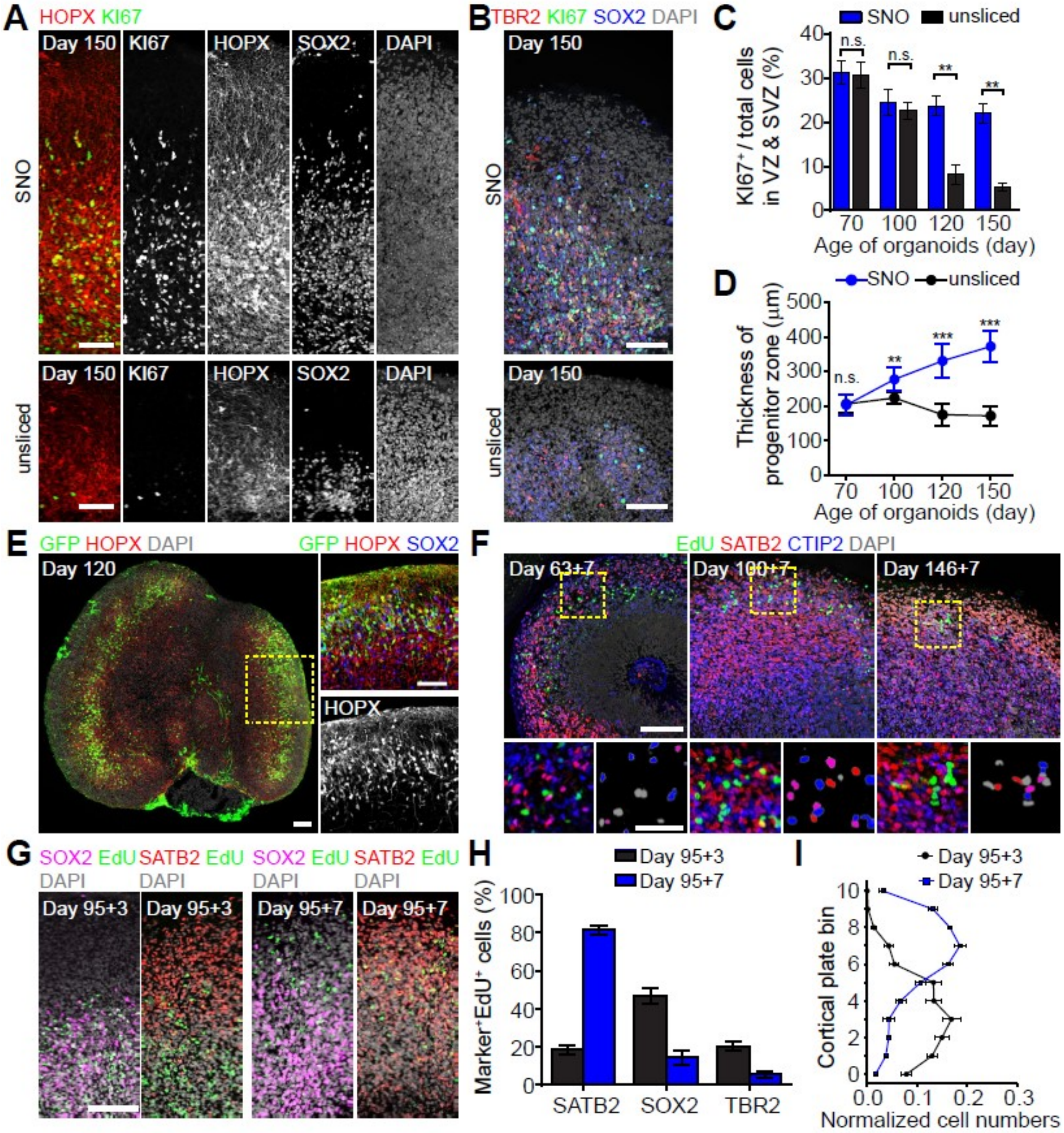
A
HOPX KI67
Day 150
KI67
HOPX
SOX2
DAPI
SNO
unsliced
B
TBR2 KI67 SOX2 DAPI
Day 150
SNO
unsliced
C
SNO
unsliced
KI67⁺ / total cells in VZ & SVZ (%)
0
10
20
30
40
n.s.
n.s.
**
**
70
100
120
150
Age of organoids (day)
D
SNO
unsliced
Thickness of progenitor zone (µm)
0
100
200
300
400
500
n.s.
**
***
***
70
100
120
150
Age of organoids (day)
E
GFP HOPX DAPI
GFP HOPX SOX2
Day 120
HOPX
F
EdU SATB2 CTIP2 DAPI
Day 63+7
Day 100+7
Day 146+7
G
SOX2 EdU DAPI
SATB2 EdU DAPI
SOX2 EdU DAPI
SATB2 EdU DAPI
Day 95+3
Day 95+3
Day 95+7
Day 95+7
H
Day 95+3
Day 95+7
Marker⁺EdU⁺ cells (%)
0
20
40
60
80
100
SATB2
SOX2
TBR2
I
Day 95+3
Day 95+7
Cortical plate bin
0
2
4
6
8
10
0.0
0.1
0.2
0.3
Normalized cell numbers

Figure 10. Sustained Neurogenesis and Radial Migration of New-born Neurons in SNOs

(A and B) *Sample tiling confocal images showing the oSVZ of Day 150 SNOs (top) and unsliced (bottom) organoids, immunostaining for proliferation marker KI67, general NPC marker SOX2, oRG marker HOPX (A), and IPC marker TBR2 (B). HOPX^{+}Ki67^{+} cells are proliferating oRGs, and TBR2^{+}Ki67^{+} cells are transient-amplifying IPCs. Scale bars, 100 µm.*

(C) *Quantification of the percentage of KI67^{+} cells in the progenitor zones (VZ and oSVZ) within SNOs and unsliced organoids at different time points. Values represent mean ± S.E.M. (n = 5 organoids; n.s.: $p > 0.05$, **$p < 0.005$, Student's t test).*

(D) *Quantification of the size of the proliferative progenitor zones in SNOs and unsliced organoids. Values represent mean ± S.D. (n ≥ 20 and 10 organoids for SNOs and unsliced organoids from 2 iPSC lines, respectively; n.s.: $p > 0.05$, **$p < 0.005$, ***$p < 0.0005$, Student's t test).*

(E) *Adenovirus expressing GFP preferentially infects oRG-like cells with unipolar morphologies and basal processes contacting the pial surface. Shown on the left is a sample tiling confocal image for a Day 120 SNO with two large oSVZ structures. The inset shows magnified view with a 90-degree counter-clockwise rotation. Scale bars, 100 µm.*

(F) *Sample confocal images for 7-day EdU pulse-chase experiments, with newborn neurons labeled double-positive for EdU and neuron marker CTIP2 or SATB2 in SNOs at Day 70, 107 and 152. Scale bars, 100 µm and 50 µm in insets. EdU^{+} nuclei in the insets (bottom right panels) are pseudo-colored to indicate their marker expression: Grey (SATB2^{-}, CTIP2^{-}); Red (SATB2^{+}, CTIP2^{-}); Blue (SATB2^{-}, CTIP2^{+}); Purple (SATB2^{+}, CTIP2^{+}).*

(G) *Sample confocal images for 3- and 7-day EdU pulse-chase experiments, showing that EdU^{+} cells migrated from the SOX2-enriched progenitor zones to the SATB2-enriched CP from Day 98 to Day 102. Scale bar, 100 µm.*

(H) *Quantification of the percentage of EdU^{+} cells expressing neuron marker SATB2, NPC marker SOX2, or IPC marker TBR2, at 3 and 7 days post-EdU labeling on Day 95. Values represent mean ± S.E.M. (n = 5 organoids for each marker).*

(I) *Quantifications of the localization of EdU^{+} cells at 3 and 7 days post-EdU labeling, showing a shift towards the basal direction. The cortical structure from apical surface to basal surface is evenly divided into bins 0-10. Shown are curves representing the normalized abundance within each bin, calculated as [# of EdU^{+} cell in a bin/# of total EdU^{+} cells]. Values represent mean ± S.E.M. (n = 10 organoids). Same samples as in (H).*

5.3.3 - Layer Expansion Persists in SNOs over Long-term Culture

With improved cell viability and sustained neurogenesis, the laminar structures of SNOs continuously expand over long-term cultures, while maintaining the organization of progenitor zones and neuronal layers (Figure 11A). From Day 70 to Day 150, the cortical structures of SNOs displayed well-defined VZ, oSVZ and CP layers. The VZ was marked by densely packed SOX2$^+$ NPCs at the apical side; the oSVZ contained mixed populations of NPCs, IPCs and CTIP2$^+$ migrating neurons; and the CP at the basal side was exclusively populated by neurons forming condensed layers. We measured the total layer thickness of cortical structures by the distance between the apical (ventricular) surface to the basal (pial) surface. While the viable thickness in unsliced organoids was restricted to 300-400 µm and stopped increasing soon after Day 70, SNOs could consistently expand far beyond this limit (Figure 11B-C). At Day 150, the total layer thickness could reach 700 µm and the CP thickened to over 300 µm on average (Figure 11B-C).

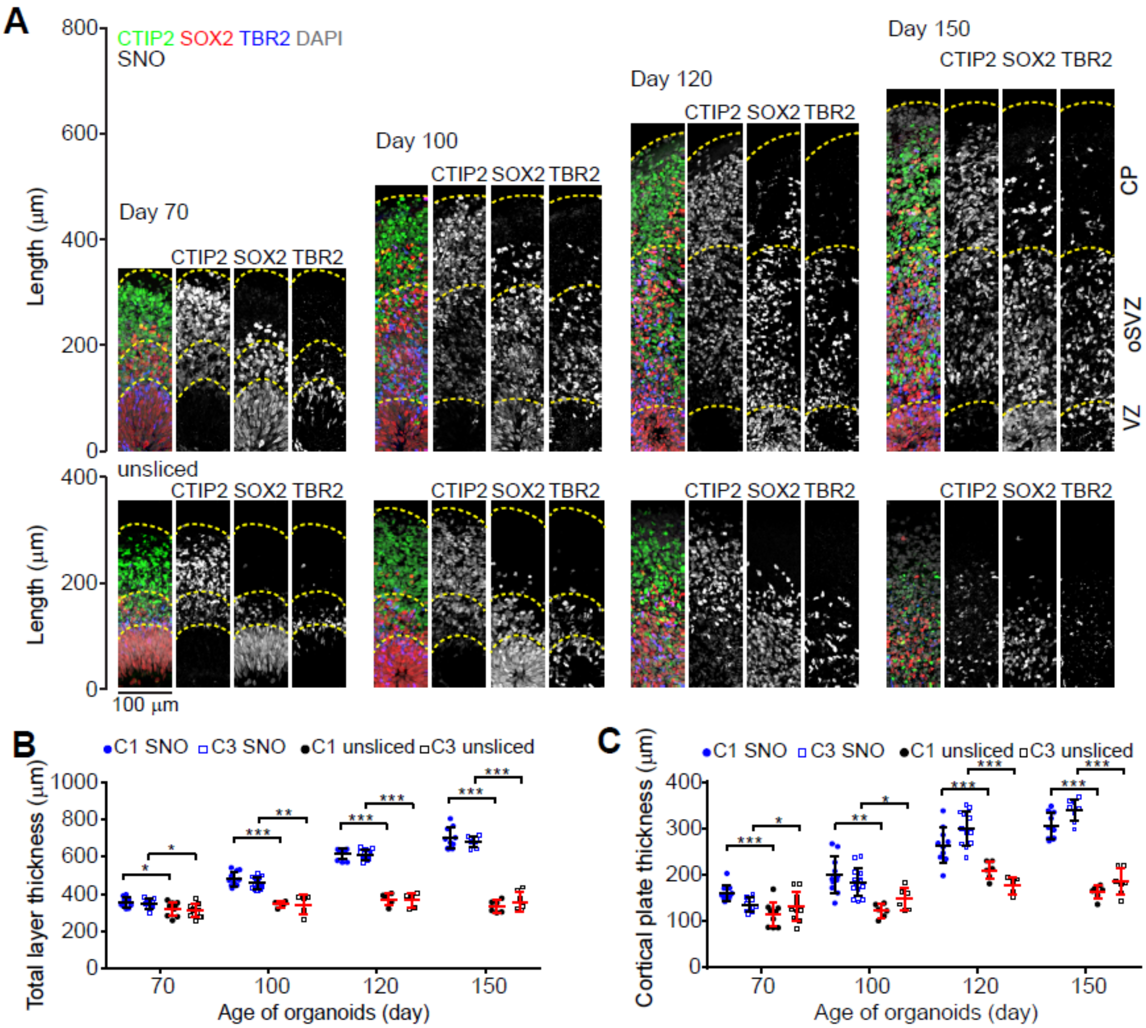
A
CTIP2 SOX2 TBR2 DAPI
SNO
Day 70
Day 100
Day 120
Day 150
CTIP2 SOX2 TBR2
CP
oSVZ
VZ
unsliced
Length (µm)
800
600
400
200
0
100 µm
B
●C1 SNO □C3 SNO ●C1 unsliced □C3 unsliced
Total layer thickness (µm)
1000
800
600
400
200
0
70
100
120
150
Age of organoids (day)
*
**
***
C
Cortical plate thickness (µm)
400
300
200
100
0

Figure 11. Layer Expansion in SNOs over Long-term Cultures

(A) *Sample tiling confocal images of cortical structures in SNOs (top) and unsliced organoids (bottom), for immunostaining of CTIP2, SOX2 and TBR2 at Day 70, 100, 120 and 150. Dashed lines mark the pial surfaces and the boundaries the ventricular zone (VZ), outer subventricular zone (oSVZ) and cortical plate (CP). The laminar structures in Day 120 and 150 unsliced organoids are disorganized, the thus not marked by dashed lines. Scale bar: 100 μm.*

(B and C) *Quantifications of the total thickness (B) and CP thickness (C) in SNOs and unsliced organoids. Values represent mean ± S.D. (n ≥ 10 and 5 organoids for SNOs and unsliced organoids for each cell line, respectively; *p < 0.05, **p < 0.005, ***p < 0.0005, Student's t test).*

5.5.4 - SNOs Form Distinct Upper and Deep Cortical Layers

We next investigated whether improved cell viability and sustained CP expansion lead to the formation of separated cortical layers. Previously, we reported that the CP in unsliced forebrain organoids contained cortical neurons expressing upper and deep layer markers, but they did not separate into distinguishable layers, reminiscent of developing human cortex around gestational weeks (GW) 14 to 18 (Hevner, 2007; Qian et al., 2016). Similar to unsliced organoids, the CP of Days 70 and 100 SNOs contained both upper layer intracortical (callosal) projection neuron marker SATB2 and deep layer subcortical projection neuron marker TBR1 without layer preferences (Figure 12A). In contrast, when SNOs were cultured to Day 120 and beyond, the laminar distribution of the markers became layer specific. At Days 120 and 150, the upper layers were populated exclusively by SATB2$^+$/TBR1$^-$ neurons, whereas the deep layers were dominated by TBR1$^+$/SATB2$^-$ neurons, separated by a defined boundary (Figure 12A). We divided the thickness of the CP into 11 equally-sized bins to quantitatively analyze the laminar expression patterns of SATB2 and TBR1 (Figure 12B). At Days 70 and 100, the distributions of the two markers overlapped with each other, but at Days 120 and 150, they exhibited two separated peaks representing the upper and deep layers (Figure 12B).

Importantly, we observed a sharp decrease in the percentage of neurons co-expressing SATB2 and TBR1 over time: while 90.3 ± 4.7% of SATB2$^+$ neurons co-expressed TBR1 at Day 70, this percentage dropped to 10.7 ± 1.2% at Day 150 (Figure 12C), suggesting post-mitotic fate specification of existing cortical neurons during the establishment of separated laminar expression domains. In some cases, the CP in Day

150 SNOs could be subdivided further to resemble the marker distribution and cytoarchitecture of Layers I to VI in the perinatal frontal cortex (Saito et al., 2011). These dynamic progressions in layer-specific marker expression and localization closely resemble the human neocortex in the third trimester (Saito et al., 2011). In addition, analyses for another pair of markers, RORB and CTIP2 (Nakagawa and O'Leary, 2003), depicted very similar establishment of laminar expression patterns specific to the upper and deep cortical layers after Day120 (Figure 12D-E). The ratio of co-expression between RORB and CTIP2 also decreased steeply over time (Figure 12F). We further analyzed the laminar distribution of additional known markers for cortical neuron subtypes (Lake et al., 2016), among which CUX1 and LAMP5 displayed exclusive localization in the superficial layers at Day 150, similar to their distribution in the adult human neocortex.

In the rodent embryonic cortex, expression of SATB2 and CTIP2 directly controls axonal projection of cortical neurons (Britanova et al., 2008). Visualized by a general axon marker SMI312 (Ulfig et al., 1998), the CTIP2$^+$ deep layer contained mostly vertically-oriented axons and the SATB2$^+$ upper layer was filled by tangentially-oriented axons circling the organoids at Day 150. The boundary delineated by the tangential and vertical axonal patterns coincided with the boundary between SATB2 and CTIP2 enriched domains, which is consistent with the notion that their projection patterns are controlled by the expression of neuronal subtype-specific transcription factors**.**

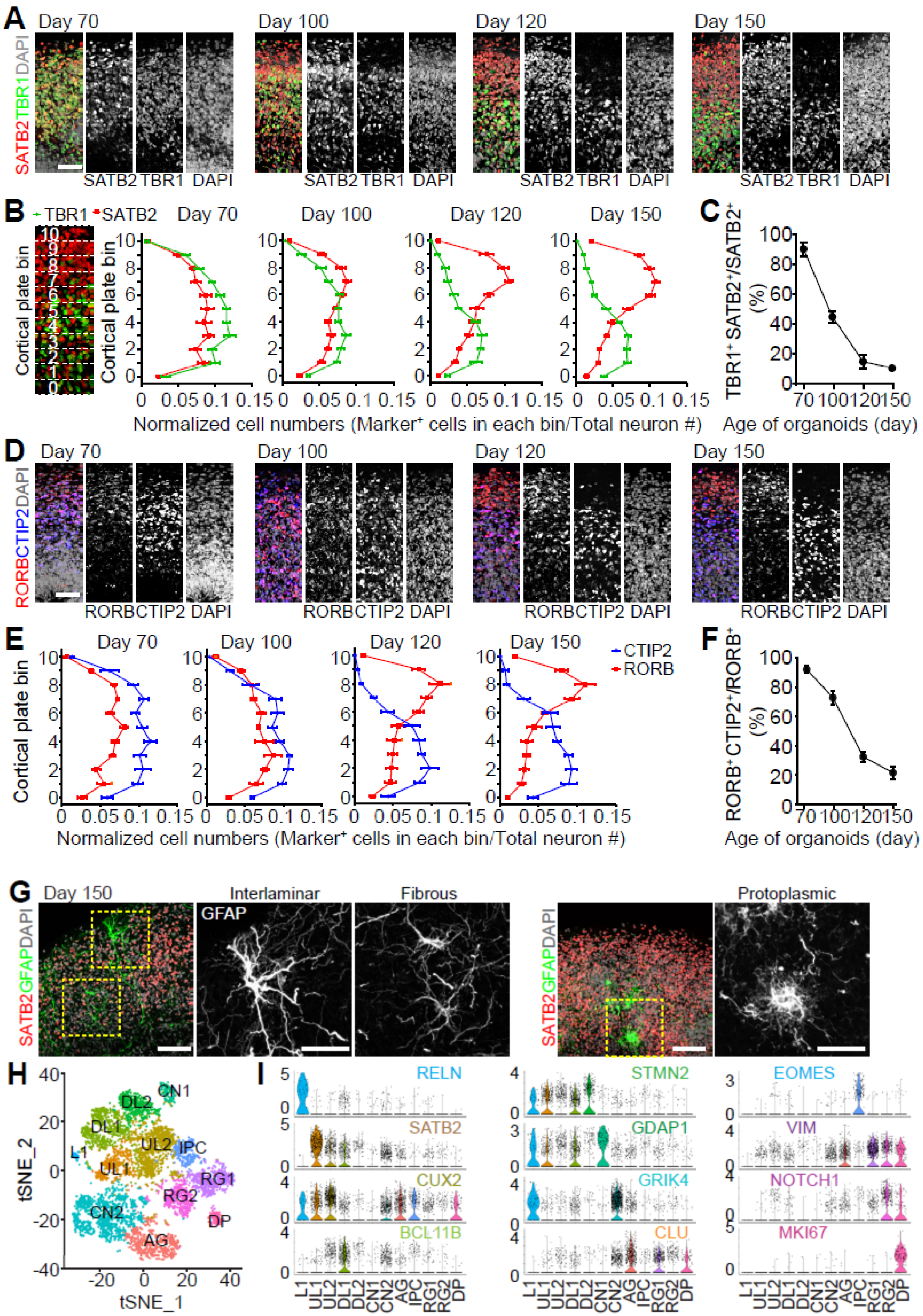
A
Day 70
Day 100
Day 120
Day 150
SATB2TBR1DAPI
SATB2 TBR1 DAPI
B
TBR1
SATB2
Cortical plate bin
Normalized cell numbers (Marker+ cells in each bin/Total neuron #)
C
TBR1+SATB2+/SATB2+ (%)
Age of organoids (day)
D
RORBCTIP2DAPI
RORB CTIP2 DAPI
E
CTIP2
RORB
F
RORB+CTIP2+/RORB+ (%)
G
Day 150
Interlaminar
Fibrous
Protoplasmic
GFAP
SATB2GFAPDAPI
H
tSNE_1
tSNE_2
L1
UL1
UL2
DL1
DL2
CN1
CN2
IPC
RG1
RG2
AG
DP
I
RELN
SATB2
CUX2
BCL11B
STMN2
GDAP1
GRIK4
CLU
EOMES
VIM
NOTCH1
MKI67

Figure 12. Establishment of Separated Upper and Deep Cortical Layers and Specification of Cortical Neuron Subtypes

(A) *Sample immunostaining confocal images of the CP of SNOs for callosal projection neuron marker SATB2, and subcortical projection neuron marker TBR1 at Day 70, 100, 120 and 150. Shown are cropped 100 x 300 µm columns in the CP, and the pial surface is at the top. Scale bar, 50 µm.*

(B) *Quantifications of the distribution of SATB2*$^+$ *and TBR1*$^+$ *neurons in the CP. The CP is evenly divided into 11 bins, bins 0-10 follow apical-to-basal direction. Shown are curves representing the normalized abundance within each bin, calculated as [# of marker*$^+$ *cell in a bin/# of total neurons]. Values represent mean ± S.E.M. (n = 10 organoids from C1 and C3 iPSC lines).*

(C) *Quantification of the ratio of co-expression of TBR1 and SATB2 over SATB2*$^+$ *cells in the CP. Same samples as in (B). Values represent mean ± S.D.*

(D) *Sample immunostaining confocal images of the CP of SNOs for upper layer neuron marker RORB, and deep layer neuron marker CTIP2 at Day 70, 100, 120 and 150. Shown are cropped 100 x 300 µm columns in the CP, and the pial surface is at the top. Scale bar, 50 µm.*

(E) *Quantification of the distribution of RORB*$^+$ *and CTIP2*$^+$ *neurons in the CP. Similar to (B). Values represent mean ± S.E.M.*

(F) *Quantification of the ratio of co-expression of RORB and CTIP2 over RORB*$^+$ *cells in the CP. Same samples as in (E). Values represent mean ± S.D.*

(G) *Sample confocal images of morphologically distinct GFAP*$^+$ *astrocytes in Day 150 SNOs. Scale bars, 100 µm. Note localization of interlaminar astrocyte cell body near the pia surface and protoplasmic astrocytes in the SATB2*$^+$ *upper layer.*

(H) *Graph-based clustering of cells from Day 150 SNOs by single-nuclei RNA-seq (n = 6,888 nuclei). L1, Layer I; UL, Upper layer; DL, Deep layer; CN, Cortical neuron; AG, Astrocyte/glia; IPC, Intermediate progenitor cells; RG, Radial glia; DP, Dividing progenitors. Cell population identities were determined by gene enrichment analysis using cell type and layer-specific marker gene sets obtained from the Allen Brain Atlas (Hawrylycz et al., 2012) (*http://human.brain-map.org/*) and published datasets of single-cell RNA-seq of the developing and adult human cerebral cortex (Fan et al., 2018; Lake et al., 2016; Nowakowski et al., 2017; Pollen et al., 2015).*

(I) *The expression of selected cluster-specific marker genes used for cell type classification. Shown are violin plots overlaid on the scatter plots, where the proportion of cells expressing a given gene is the highest. The color coding for the gene names indicates the cluster in which the gene is most enriched.*

5.5.5 - SNOs Contain Diverse Cell Types

In addition to excitatory neurons, various subtypes of GABAergic neurons were also sparsely detected in SNOs, including neurons expressing Somatostatin (SST), Calretinin (CR), nNOS, NPY, ChAT and Parvalbumin (PV). Moreover, immunostaining for GFAP revealed the presence of three morphologically distinct astrocyte subtypes, which displayed the hallmarks of the protoplasmic astrocytes, fibrous astrocytes and the primate/human-specific interlaminar astrocytes found in the human cerebral cortex (Figure 12G) (Hodge et al., 2019; Oberheim et al., 2009). In Day 150 SNOs, the subtype-dependent laminar distributions of astrocytes also resemble that in the human cerebral cortex. The cell body of interlaminar-like astrocytes reside exclusively in the Layer I/Marginal zone and extended long descending processes into the CP, while the protoplasmic and fibrous-like astrocytes were located in the CP (Figure 12G). Sustained proliferation allowed for generation of oligodendrocyte precursor cells (OPC) and oligodendrocytes, the late-born cell types in the forebrain NPC lineage.

To characterize the full repertoire of cell type diversity within SNOs, we performed single-nuclei RNA-seq analysis. Following the recently published SPiLT-seq method (Rosenberg et al., 2018), we analyzed 6,888 single nuclei from Day 150 SNOs. Unsupervised clustering of single cells was achieved by principal component analysis using highly variable genes, and was visualized on two-dimensional t-distributed stochastic neighbor embedding (tSNE) plot, from which we obtained 12 well-defined clusters (Figure 12H). Known layer- or subtype-specific cortical neuron markers, such as RELN (Cluster L1), SATB2 (Cluster UL1), CUX2 (Cluster UL2), BCL11B (CTIP2, Cluster DL1), were specifically enriched in distinct clusters and EOMES (TBR2) was exclusively expressed in the IPC cluster (Figure 12I). Radial glia cell marker VIM and dorsal forebrain NPC marker PAX6 were expressed in the radial glia cell clusters (RG1, RG2 and DP) (Figure 12I). The dividing progenitor (DP) cluster is specifically enriched with MKI67 and other mitotic genes, and differential expression of NOTCH1 distinguishes RG1 and RG2 clusters (Figure 12I), as inhibition of Notch is an indicator for the differentiation state of oRGs (Hansen et al., 2010). *In situ* hybridization images of the adult human cortex obtained from the Allen Brain Atlas (http://human.brain-map.org/) validated the layer-dependent expression patterns of selected marker genes used in the analyses. We compared SNO cells with embryonic human prefrontal cortex cells from a published scRNA-seq dataset to assess SNO's similarity with the human fetal brain (Zhong et al., 2018). Pearson Correlation analyses between all SNO and fetal cell clusters showed SNO cell types most highly correlated to the corresponding endogenous cell types, indicating that their transcriptional profiles were similar to endogenous cells in the developing human prefrontal cortex. Because the fetal human dataset we obtained lacked a distinct astrocyte cluster, we separately compared the Astroglia (AG) cluster to another published dataset of bulk RNA-seq of human fetal and postnatal primary astrocytes (Zhang et al., 2016). Surprisingly, the astrocytes in Day 150 SNOs showed higher similarity to human postnatal astrocytes than to fetal astrocytes, suggesting astrocyte maturation may be accelerated in the SNO culture.

To characterize the functional properties of neurons in SNOs, we performed electrophysiological analysis with whole-cell recording in slices acutely prepared from SNOs and detected spontaneous synaptic currents. Biocytin labeling after recording revealed the complex morphology of neurons with dendritic spine structures and long tangentially-oriented axons extending for millimeters with branches into multiple regions in the CP , consistent with the axonal patterns revealed by the SMI312 immunostaining. At the circuitry level, extracellular recording of intact SNOs using a four-shank multi-electrode laminar probe revealed spontaneous firing of action potential and coordinated burst patterns, indicative of network activities across long distances both vertically and horizontally. Among sets of coordinated single neurons detected several hundred micrometers apart, the order of single neuron recruitment and burst durations showed a repeatable temporal pattern, suggesting the presence of stably established connectivity.

5.5.6 - WNT/β-Catenin Signaling Regulates Post-Mitotic Fate Specification of Cortical Neurons

We next applied our SNO system to investigate molecular mechanisms regulating human neocortical development. The fate of cortical neurons is partially determined cell-autonomously during neurogenesis, but the post-mitotic fate specification that refines neuronal subtype identity and establishes layer-specific gene expression is synergistically regulated by cell non-autonomous signaling (Fame et al., 2011; Greig et al., 2013; Molyneaux et al., 2007; Shepherd, 2013; Telley et al., 2019). The mechanisms regulating cortical neuron fate specification in humans have remained largely unclear due to the lack of an accessible and representative model. The WNT/β-Catenin pathway genes, including WNT7B, are specifically enriched in the deep layer and subplate in the human embryonic cortex during the late second trimester (Abu-Khalil et al., 2004; Miller et al., 2014). The WNT/β-Catenin signaling regulates the specification of subplate neurons into deep layer neurons by suppressing callosal projection fate and promoting the alternative subcortical projection fate in a layer-specific manner (Ozair et al., 2018). Similar to its localization *in vivo*, WNT7B was enriched in the deep CP layers of SNOs, and progressively established mutually exclusive domains with the SATB2$^+$ upper layer from Day 100 to Day 150 (Figure 13A). Notably, the deep layer-specific enrichment of WNT7B was already apparent at Day 100, preceding the establishment of separated cortical layers, suggesting that WNT7B expression could regulate, but is not the result of cortical layer specification (Figure 13A).

To investigate the functional role of WNT/β-Catenin signaling in cortical neuron fate specification, we treated Day 100 SNOs with either β-Catenin inhibitor IWR-1-endo (IWR) or β-Catenin activator CHIR99021 (CHIR) for 20 days between Day 100 to Day 120, a time window with rapid changes in the laminar expression patterns of upper and deep layer markers (Figure 12A-F). SNOs treated with IWR showed an increase in SATB2 expression in the lower cortical bins, resulting in comparable abundance between SATB2$^+$ neurons and TBR1$^+$ neurons in the deep layers at Day 120 (Figure 13B-C). On the contrary, CHIR-treated SNOs showed a decrease in SATB2 expression, accompanied by substantial increase of TBR1 across the entire CP (Figure 13B-C). As a result, the expression patterns of SATB2 and TBR1 were overlapping and lost their respective preferences to upper and deep layers in drug-treated SNOs (Figure 13C-D). Interestingly, both IWR and CHIR treatments resulted in a significant increase in the percentage of neurons co-expressing TBR1 and SATB2, suggesting an impairment in neuronal fate specification (Figure 13E). Similarly, the drug treatment altered the laminar expression patterns of RORB and CTIP2 (Figure 13C). Elevation of RORB induced by IWR in the deep layer and elevation of CTIP2 induced by CHIR in the upper layer both disrupted the respective layer-specificity of the two markers, concurring with an increased proportion of double-positive cells (Figure 13C and 13F).

To determine whether the drug treatments affected postmitotic neurons or neurogenesis, we performed EdU-pulse chase labeling to specifically label neurons birth-dated at Day 95. On Day 103 (8 days post-labeling), DMSO, IWR or CHIR were added to the culture medium. At 20 days after drug treatment, the ratio of co-expression between SATB2 and TBR1 among EdU$^+$ neurons was elevated in both IWR and CHIR treated SNOs . Because EdU is diluted in cycling cells, cells retaining EdU after 28 days of pulse-chase are predominantly postmitotic neurons born within a few days after Day 95, providing direct evidence that WNT/ β-Catenin controls post-mitotic fate specification of cortical neurons. Following the withdrawal of drug treatment at Day 120, the IWR-induced effects persisted, indicating that Day 100 to Day 120 may be a decisive time window for neuronal subtype fate specification. Together, these results showed that similar to the developing human cerebral cortex, SNOs rely on self-maintained layer-dependent signaling to regulate the distinct laminar expression of neuron subtype markers, which are sensitive to manipulations and perturbations, resulting in robust changes.

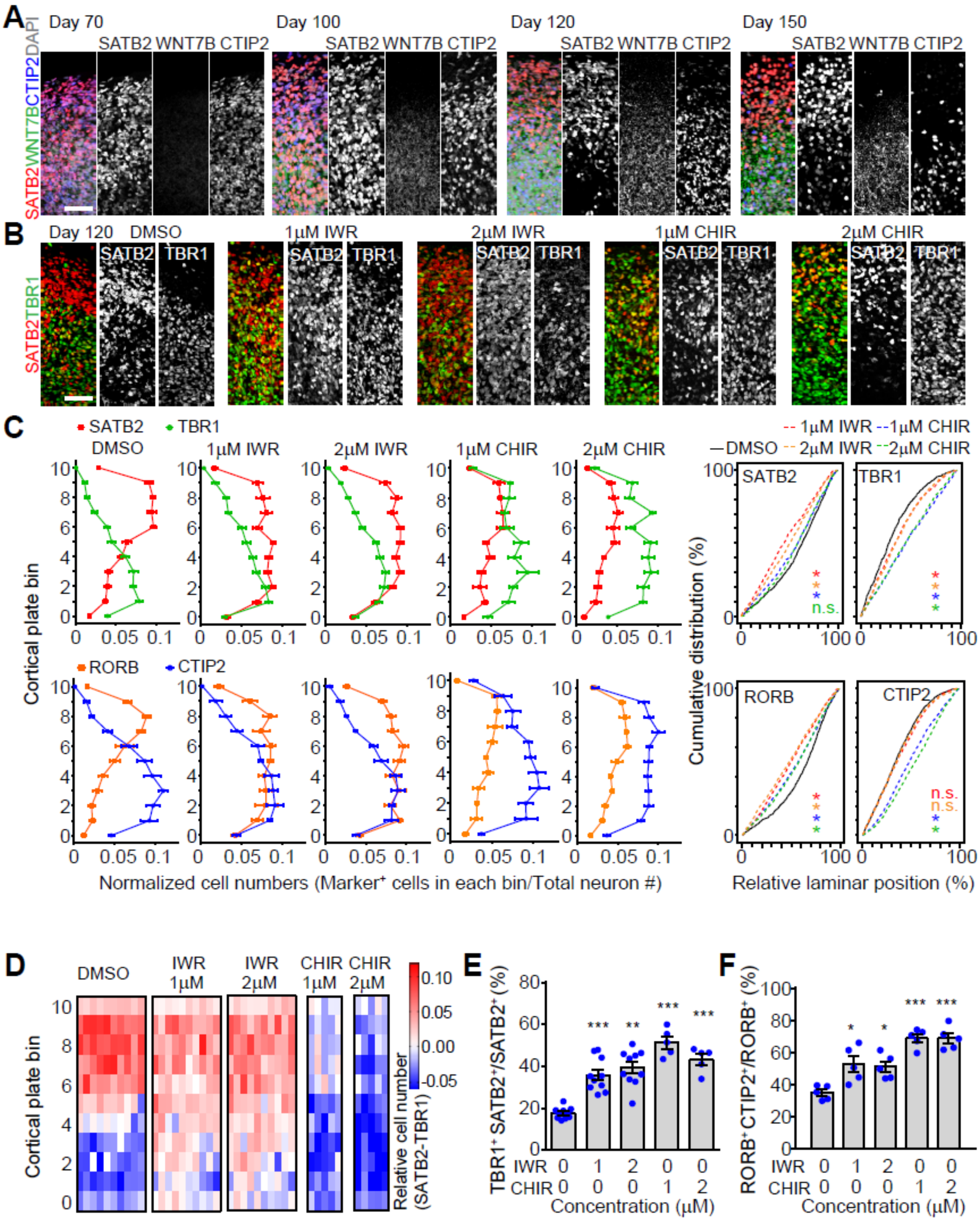
A
SATB2WNT7BCTIP2DAPI
Day 70
Day 100
Day 120
Day 150
SATB2 WNT7B CTIP2
B
Day 120 DMSO
1μM IWR
2μM IWR
1μM CHIR
2μM CHIR
SATB2TBR1
SATB2 TBR1
C
SATB2
TBR1
DMSO
1μM IWR
2μM IWR
1μM CHIR
2μM CHIR
RORB
CTIP2
Cortical plate bin
Normalized cell numbers (Marker⁺ cells in each bin/Total neuron #)
1μM IWR
1μM CHIR
DMSO
2μM IWR
2μM CHIR
Cumulative distribution (%)
Relative laminar position (%)
n.s.
D
DMSO
IWR 1μM
IWR 2μM
CHIR 1μM
CHIR 2μM
Cortical plate bin
0.10
0.05
0.00
-0.05
Relative cell number (SATB2-TBR1)
E
TBR1⁺SATB2⁺/SATB2⁺ (%)
IWR 0 1 2 0 0
CHIR 0 0 0 1 2
Concentration (μM)
*** ** *** ***
F
RORB⁺CTIP2⁺/RORB⁺ (%)
IWR 0 1 2 0 0
CHIR 0 0 0 1 2
Concentration (μM)
* * *** ***

Figure 13. Regulation of Cortical Neuron Fate Specification by WNT/β-Catenin Signaling

(A) *Sample confocal images of the CP of SNO at Day 70, 100, 120 and 150, immunostaining for SATB2, CTIP2 and secreted WNT signaling protein WNT7B. WNT7B progressively establishes enriched domains that is exclusive with SATB2, but overlapping with CTIP2. Scar bars, 100 µm.*

(B) *Sample confocal images showing the effects of β-Catenin antagonist (IWR-1-endo, IWR) and agonist (CHIR9902, CHIR) on the expression patterns of SATB2 and TBR1 neurons in the CP. Compounds were added into culture medium at the indicated concentrations from Day 100 to Day 120 and the analysis was performed at Day 120. Shown are cropped 100 x 300 µm columns from sample immunostaining confocal images of the CP for TBR1 and CTIP2. Scale bar, 50 µm.*

(C) *Quantifications of the distribution of SATB2*$^+$*, TBR1*$^+$ *and RORB*$^+$*, CTIP2*$^+$ *neurons in the CP of SNOs treated with compounds. Shown on the left are curves representing the normalized abundance within each bin, similar to Figure 12B. Values represent mean ± S.E.M. (n = 10 organoids from 2 iPSC lines for DMSO and IWR treatments; n = 5 organoids for CHIR treatments). Shown on the right are cumulative distribution curves of marker positive neurons. Kolmogorov-Smirnov tests were performed for the drug treated conditions, indicated by the corresponding color, against DMSO (n.s.: $p > 0.05$, *$p < 0.05$, Kolmogorov-Smirnov tests).*

(D) *Heatmap plots for the differential abundance between SATB2*$^+$ *and TBR1*$^+$ *in the CP of drug treated SNOs. Each row represents one of the 11 CP bins and each column represents individual SNO analyzed. The differences between the abundance of SATB2*$^+$ *nuclei and TBR1*$^+$ *nuclei within each bin is calculated as [(normalized SATB2*$^+$ *nuclei #) – (normalized TBR1*$^+$ *nuclei #)]. Red on the heatmap indicates a positive value (more SATB2) and blue indicates a negative value (more TBR1). The compound treatments resulted in the loss of the "top-red, bottom-blue" pattern found in DMSO-treated SNOs.*

(E and F) *Quantifications of the ratio of co-expression between TBR1 and SATB2 over SATB2*$^+$ *cells (E) and between RORB and CTIP2 over RORB*$^+$ *cells (F) in compound-treated SNOs. Same samples as in (C). Values represent mean ± S.E.M. (*$p < 0.05$, **$p < 0.005$, ***$p < 0.0005$, Student's t test).*

5.5.7 - Psychiatric Disorder Patient iPSC-derived SNOs Exhibit Cortical Neuron Fate Specification Deficits

Disorganization of cortical lamination has been hypothesized to contribute to the etiology of neurodevelopmental disorders (Kana et al., 2011; Zikopoulos and Barbas, 2013). For instance, *in situ* hybridization analyses revealed frequent patches of aberrant laminar expression patterns of cortical layer markers in frontal lobes of children with autism spectrum disorders (Stoner et al., 2014). The SNO system provides a platform to test the possibility that the developmental origins of other major psychiatric disorders could also involve similar abnormalities. Mutations of the *DISC1* gene have been associated with schizophrenia, major depression and autism (Brandon and Sawa, 2011; Sachs et al., 2005). In NPCs and neurons, DISC1 protein inhibits GSK3β activity through direct physical interaction, resulting in the stabilization of β-catenin, and DISC1 loss-of-function consequently impairs WNT/β-catenin signaling (Mao et al., 2009; Singh et al., 2011). Previously, we derived iPSCs from fibroblasts of psychiatric disorder patients with a heterozygous 4 base-pair (bp) frameshift deletion at the DISC1 carboxy(C) terminus and reported that the mutant DISC1 (mDISC1) causes an 80% reduction of wild-type DISC1 (wtDISC1) protein levels in iPSC-derived cortical neurons (Chiang et al., 2011; Wen et al., 2014). Differential expression analyses of RNA-seq data comparing mDISC1 and control cortical neurons showed a significant downregulation of WNT/β-Catenin pathway genes.

We generated SNOs using mDISC1 iPSCs derived from two patients with psychiatric disorder and carrying the *DISC1* mutation (D2 and D3) to compare with control SNOs using iPSCs derived from a member of the same family without the *DISC1* mutation (C3) and a control iPSC line from outside of the family (C1) (Chiang et al., 2011; Wen et al., 2014). The mDISC1 SNOs did not exhibit differences in differentiation and growth compared to controls. They showed normal levels of apoptotic and necrotic cell death, formed organized progenitor zones and CP, and the layer size expansion closely mirrored control SNOs at all time points examined, further supporting the reproducibility of the SNO method.

The CP of mDISC1 SNOs resembled control SNOs at Days 70 and 100, when the distributions of SATB2 and TBR1 were intermingled without noticeable segregation (Figure 14A-C). However, unlike the control, the laminar expression of SATB2, TBR1, RORB and CTIP2 in Day 120 mDISC1 SNOs from both patient lines lost layer-specificity and remained intermingled, a deficit that persisted at Day 150 and therefore was unlikely due to a temporary delay in differentiation (Figure 14A-H). Quantitative analyses revealed that SATB2 and RORB expression patterns were not restricted to the upper cortical bins, but instead spanned the entire CP in mDISC1 SNOs (Figure 14B and 14E). The SATB2$^+$ neurons outnumbered TBR1$^+$ neurons in both the upper and deep layers, preventing the establishment of mutually exclusive expression domains between the two markers (Figure 14G-H).

Co-expression between SATB2 and TBR1, and between RORB and CTIP2 were increased in mDISC1 SNOs, and the majority of double positive neurons were located in the lower part of the CP (Figure 15A-B). These deficits of aberrant laminar distribution and elevated marker co-expression phenocopied control SNOs treated with the β-Catenin antagonist IWR (Figure 13C-F). Curiously, CUX1 and LAMP5 remained exclusively expressed in the upper layer in mDISC1 SNOs similar to control SNOs, indicating that the laminar expression abnormalities did not universally affect all cortical neuron subtypes and that LAMP5 and CUX1 expressions were possibly controlled independently of SATB2 and RORB. These results point to the model that the cortical disorganization observed in mDISC1 SNOs is not caused by a failure of cortical layer formation, but due to specifically dysregulated cortical neuron subtype fate specification.

We previously generated isogenic iPSC lines from the D3 line via genomic editing, in which the 4-bp deletion of *DISC1* was corrected (D3R iPSC line) (Wen et al., 2014). At Day 120, the laminar expression patterns of SATB2, TRB1, RORB and CTIP2 were rescued in D3R SNOs, and their layer-specific distribution depicted a clear boundary between the upper and deep cortical layers (Figure 15C-D and 15F-G). The ratio of marker co-expression was also restored to the normal level (Figure 15E and 15H). These results provide evidence that the 4-bp deletion mutation is indeed responsible for the fate specification deficits observed in mDISC1 SNOs.

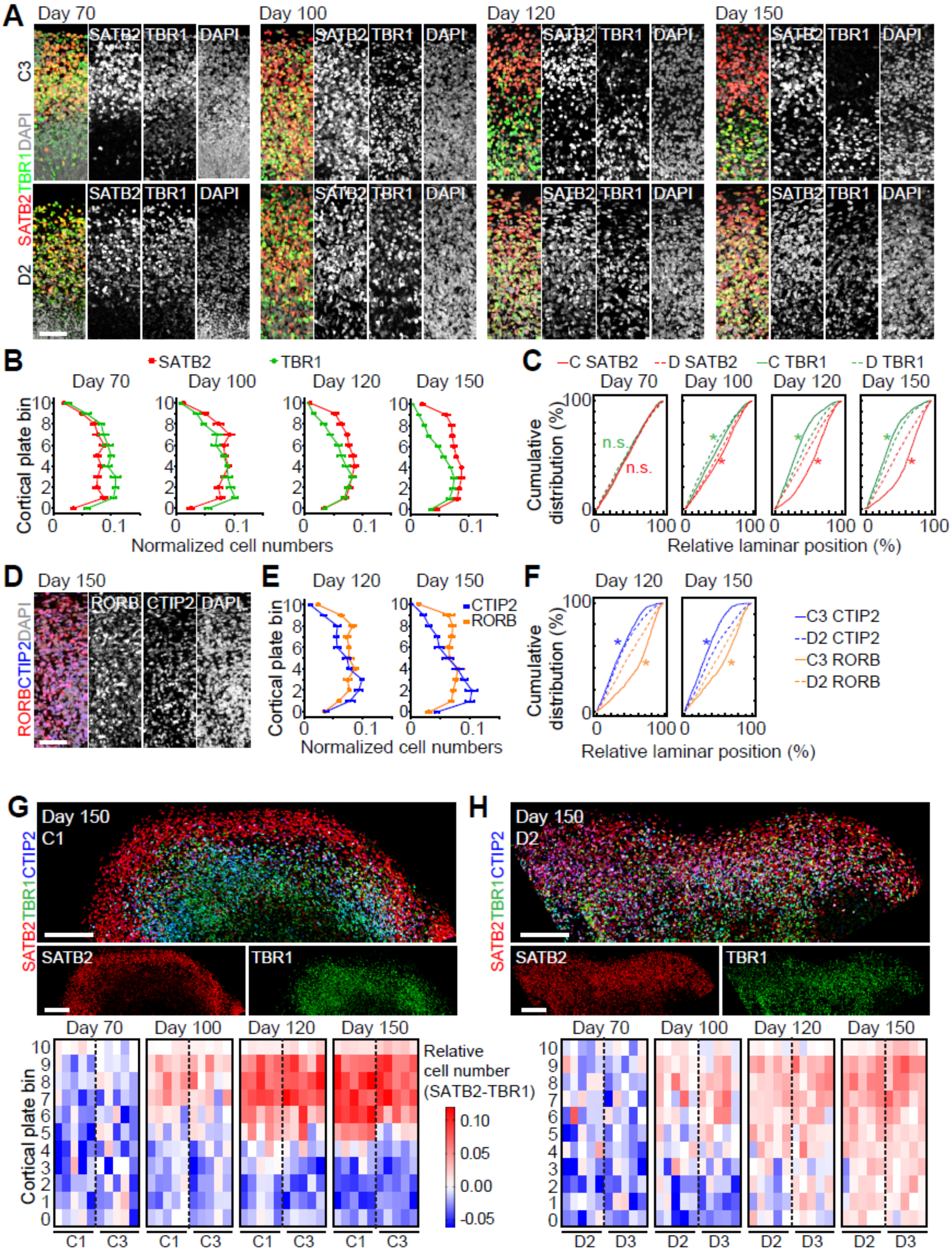
A
Day 70
Day 100
Day 120
Day 150
SATB2 TBR1 DAPI
C3
D2
SATB2 TBR1 DAPI
B
SATB2
TBR1
Cortical plate bin
Normalized cell numbers
C
C SATB2
D SATB2
C TBR1
D TBR1
n.s.
n.s.
*
Cumulative distribution (%)
Relative laminar position (%)
D
Day 150
RORB CTIP2 DAPI
E
Day 120
Day 150
CTIP2
RORB
Cortical plate bin
Normalized cell numbers
F
Day 120
Day 150
C3 CTIP2
D2 CTIP2
C3 RORB
D2 RORB
Cumulative distribution (%)
Relative laminar position (%)
G
Day 150
C1
SATB2 TBR1 CTIP2
SATB2
TBR1
H
Day 150
D2
SATB2 TBR1 CTIP2
SATB2
TBR1
Day 70
Day 100
Day 120
Day 150
Cortical plate bin
C1
C3
Relative cell number (SATB2-TBR1)
0.10
0.05
0.00
-0.05
D2
D3

Figure 14. Aberrant Laminar Expression Patterns of Cortical Layers in mDISC1 SNOs

(A) *Sample confocal images of the CP of Control (top) and mDISC1 (bottom) SNOs for SATB2 and TBR1 at Day 70, 100, 120 and 150. mDISC1 SNOs displayed extensive overlap between the laminar expression patterns of SATB2 and TBR1. Scale bar, 50 µm.*

(B and C) *Quantifications of the distribution of SATB2$^+$ and TBR1$^+$ neurons in mDISC1 SNOs, to be compared with Figure 12B. Values represent mean ± S.E.M. (n = 10 organoids from D2 and D3 iPSC lines). Also shown in (C) are cumulative distribution curves of marker positive neurons at each time point. Kolmogorov-Smirnov tests were performed between Control (C) and mDISC1 (D) SNOs for SATB2 (red) and TBR1 (green) (*$p < 0.05$, Kolmogorov-Smirnov tests). Same samples as in (B) and Figure 12B.*

(D-F) *The laminar distribution of RORB and CTIP2 were similarly disorganized in mDISC1 SNOs. Shown in (D) are 100 x 300 µm columns from sample confocal images at Day 150. Scale bar, 50 µm. Shown in (E) are quantifications of marker distribution at Day 120 and Day 150, to be compared with Figure 12E. Values represent mean ± S.E.M. (n = 5 organoids). Shown in (F) are cumulative distribution curves of marker positive neurons at each time point. Kolmogorov-Smirnov tests were performed between Control* ***(C)*** *and mDISC1 (D) SNOs for RORB (orange) and CTIP2 (blue) (n.s.: $p > 0.05$, *$p < 0.05$, Kolmogorov-Smirnov tests). Same samples as in (E) and Figure 12E.*

(G and H) *Comparison of cortical layers between the control SNO and mDISC1 SNO. Shown at top are sample tiling confocal images of the CP in Day 150 SNOs. Scale bars, 200 µm. Shown at bottom are heatmap plots for the differential abundance between SATB2$^+$ and TBR1$^+$ in control (E) and in mDISC1 (F) SNOs, similar to Figure 13D. Same sample as in (B) and Figure 12B.*

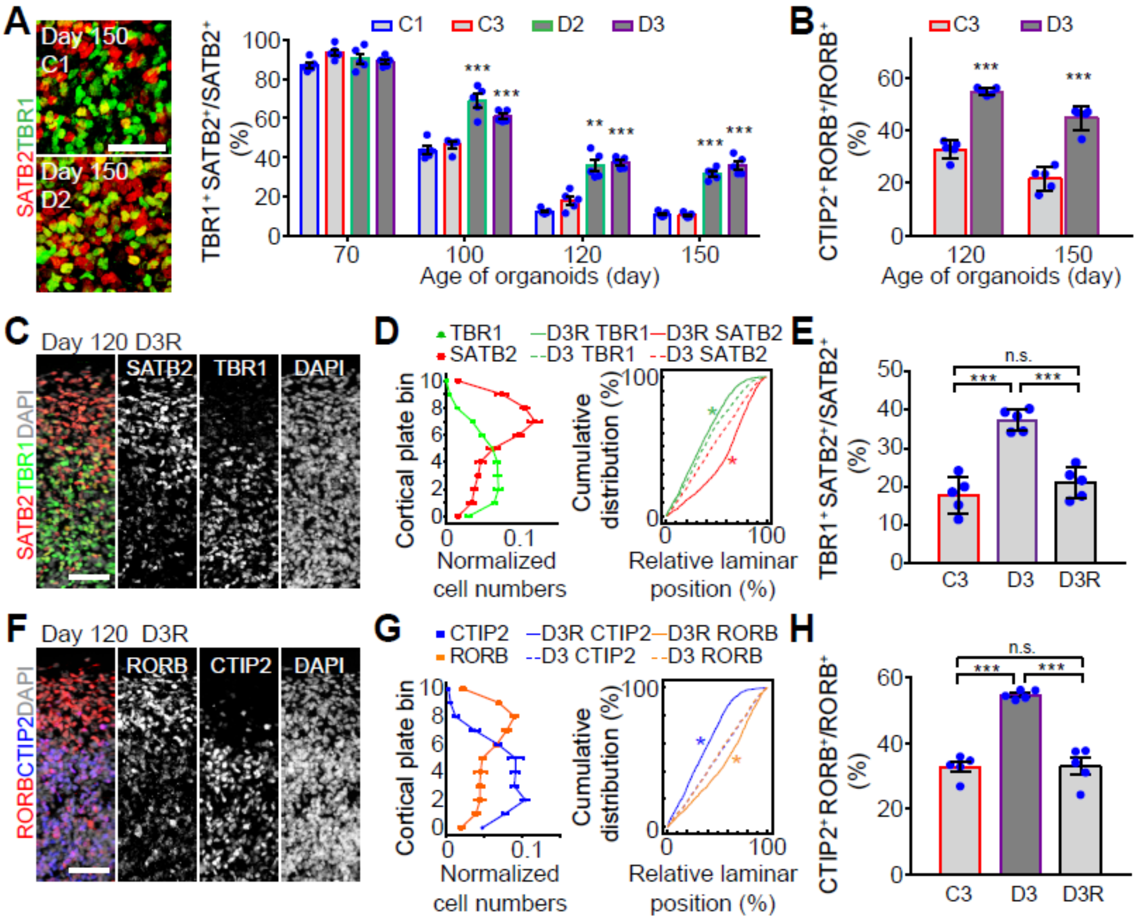
A
Day 150
C1
Day 150
D2
SATB2TBR1
C1
C3
D2
D3
TBR1⁺SATB2⁺/SATB2⁺ (%)
100
80
60
40
20
0
***
***
**
***
***
***
70
100
120
150
Age of organoids (day)
B
C3
D3
CTIP2⁺RORB⁺/RORB⁺ (%)
60
40
20
0
***
***
120
150
Age of organoids (day)
C
Day 120 D3R
SATB2TBR1DAPI
SATB2
TBR1
DAPI
D
TBR1
SATB2
D3R TBR1
D3R SATB2
D3 TBR1
D3 SATB2
Cortical plate bin
10
8
6
4
2
0
0
0.1
Normalized cell numbers
Cumulative distribution (%)
100
0
*
*
0
100
Relative laminar position (%)
E
TBR1⁺SATB2⁺/SATB2⁺ (%)
50
40
30
20
10
0
n.s.
***
***
C3
D3
D3R
F
Day 120 D3R
RORBCTIP2DAPI
RORB
CTIP2
DAPI
G
CTIP2
RORB
D3R CTIP2
D3R RORB
D3 CTIP2
D3 RORB
Cortical plate bin
10
8
6
4
2
0
0
0.1
Normalized cell numbers
Cumulative distribution (%)
100
0
*
*
0
100
Relative laminar position (%)
H
CTIP2⁺RORB⁺/RORB⁺ (%)
60
40
20
0
n.s.
***
***
C3
D3
D3R

Figure 15. Cortical Neuron Fate Specification Deficits Caused by the DISC1 Mutation.

(A)** mDISC1 SNOs showed elevated co-expression between SATB2 and TBR1. Shown on the left are sample confocal images at the boundary between upper and deep layers, double-positive cells are marked in yellow. Scale bar, 50 µm. Shown on the right is the quantification of the ratio of SATB2 and TBR1 co-expression over SATB2$^+$ neurons. Same sample as in Figure 14B. Values represent mean ± S.E.M. ($p < 0.0005$, Student's t test).*

(B)** mDISC1 SNOs also showed elevated co-expression ratio between RORB and CTIP2 at Day 150. Same sample as in Figure 14E. Values represent mean ± S.E.M. ($p < 0.0005$, Student's t test).*

***(C and D)** The layer-specific expression patterns of SATB2 and TBR1 were restored in Day 120 SNOs derived from the isogenic D3R iPSC line, in which the DISC1 mutation was corrected. Shown in (C) are 100 x 300 µm columns from sample confocal image. Scale bar, 50 µm. Shown in (D, left) is the quantification for marker distribution in the CP. Values represent mean ± S.E.M. ($n = 5$ organoids). Shown in (D, right) are cumulative distribution curves. Kolmogorov-Smirnov tests were performed between D3R and D3 SNOs for SATB2 (red) and TBR1 (green) (*$p < 0.05$, Kolmogorov-Smirnov tests).*

(E)** The ratio of co-expression between SATB2 and TBR1 was restored to normal level in D3R SNOs. Same samples as in (D). Values represent mean ± S.D. ($p < 0.0005$, Student's t test).*

***(F and G)** The layer-specific expression patterns of RORB and CTIP2 were restored in Day 120 SNOs derived from the isogenic D3R iPSC line. Shown in (F) are 100 x 300 µm columns from sample confocal image. Scale bar, 50 µm. Shown in (G, left) is the quantification for marker distribution in the CP. Values represent mean ± S.E.M. ($n = 5$ organoids). Shown in (G, right) are cumulative distribution curves. Kolmogorov-Smirnov tests were performed between D3R and D3 SNOs for RORB (orange) and CTIP2 (blue) (*$p < 0.05$, Kolmogorov-Smirnov tests).*

(H)** The ratio of co-expression between RORB and CTIP2 was restored to the normal level in D3R SNOs. Same samples as in (G). Values represent mean ± S.D. ($p < 0.0005$, Student's t test).*

5.4 – Discussion

The most remarkable feature of brain organoids over conventional *in vitro* 2D monolayer or 3D neurosphere models is the ability to recapitulate the elaborate architecture of the embryonic human brain via self-organization, which serves as the prerequisite for proper maintenance of the neural stem cell niche, neuronal migration, cell-cell interactions and circuitry development. Previously published cortical organoid systems are generally most representative of early-to-mid gestation human brain development and very useful for modeling diseases that are characterized by striking structural malformations that manifest early, such as microcephaly and lissencephaly (Bershteyn et al., 2017; Qian et al., 2016). However, because no published cortical organoid systems to date have consistently shown the formation of distinct cortical layers, their utility for investigating late-stage human brain development and disorders is uncertain.

Using a precisely-controlled slicing method to overcome the diffusion barrier and prevent interior hypoxia, we address the fundamental limiting factor that has prohibited cortical organoids from mimicking the architecture of late-stage human cortical development. By exposing progenitor zones to the external culture environment while maintaining their structural integrity, the disk-shaped SNOs grow more healthily than traditional spherical brain organoids, allowing significantly larger cortical structures to emerge. A very recent study reported the use of liquid-air interface culture for cerebral organoids, where the additional surface exposure to the external environment led to significantly improved neuronal survivability (Giandomenico et al., 2019). While the liquid-air interface culture accelerates neuronal maturation and promotes formation of aligned axonal tracks, it also resulted in flattening of the tissue and the VZ and SVZ structures were not preserved. In contrast, because we perform the slicing after the establishment of VZ and aligned radial glia scaffold, and subsequently return the organoid to a 3D suspension culture, this procedure does not disrupt the architectural integrity of the progenitor and neuronal layers. Importantly, the radial scaffold provides the guiding substrate for neuronal migration to reach the designated laminar location in the CP, synergizing with sustained neurogenesis to successfully achieve the formation of distinct upper and deep cortical layers in SNOs at later stages. The laminar distributions of cortical neuron markers as well as morphologically distinct astrocyte subtypes in Day 150 SNOs closely resemble their localization in the adult human cerebral cortex and properly reflect species-associated differences between human and rodents (Lake et al., 2016). Moreover, the dramatic reduction in the number of neurons co-expressing upper and deep layer markers over time suggests SNOs can recapitulate the human/primate-specific process of post-mitotic fate specification, which cannot be modeled in rodents.

We showed that the SNO method is reproducible and generates consistent outcomes that can be reliably quantified for multiple iPSC lines. The protocol is simple to follow and is compatible for scaling-up. The method may also be applied to organoid protocols for other brain regions or other organs as a universal approach to improve cell viability and sustain tissue expansion in 3D suspension cultures. Although generation of late-stage SNOs is relatively time-consuming, it parallels the natural developmental timeline of the human brain as we harness the intrinsic potential, without extensive biochemical interference to accelerate its development. By performing systematic characterizations of SNOs at fixed time points from Day 70 to Day 150, we demonstrate that the developmental dynamics of SNOs match *in vivo* corticogenesis at the second and early third trimester, and the age of the SNO is a reliable predictor for the corresponding maturation stage. The approach does have the caveat of repeated slicing (once per month), which may cause some damages to axons and dendrites. However, we keep fairly thick sections (500 μm) and long-distance axonal process and synaptic connections could be maintained in the SNO system. Furthermore, our extracellular recording experiments demonstrated repeatable temporal patterns of recruitment and burst durations among neurons across long distance in the CP, suggesting that local connectivity remained intact despite of repeated slicing. The robust synchronization of spontaneous firing observed in SNO highlights its utility for the investigation of network properties in normal and disease-related conditions.

Because the establishment of distinct cortical layers and specification of neuron fate occur late in cortical development, the SNO method provides a unique platform to investigate phenotypes that cannot be modeled by other current organoid systems. We demonstrated the applicability of our system by identifying the critical role of WNT/β-Catenin signaling in the regulation of postmitotic cortical neuron subtype identities and discovering potentially disease-relevant phenotypes in psychiatric disorder patient-derived organoids. Via suppression of SATB2 and RORB expression, WNT/β-Catenin signaling controls the fate specification process pivotal for the establishment of layer-specific laminar expression patterns. As WNT/β-Catenin signaling is exclusively enriched in the deep cortical layers, the resulting SATB2 repression instructs neurons in the deep layers, which initially co-express TBR1 and SATB2, to convert into

TBR1^{+}/SATB2^{-} deep layer subcortical projection neurons. This fate specification process is similarly impaired in both SNOs treated with a β-Catenin inhibitor and in the mDISC1 SNOs, as indicated by the persistent high level of co-expression between SATB2/TBR1 and RORB/CTIP2 at Day 120 and Day 150. It remains difficult to determine the extent to which our findings mirror the deficits in the patient brains, but it is possible that the dysregulation of the laminar expression of neuronal subtype marker genes, as recently observed in the brains from children with autism (Stoner et al., 2014), is a novel mechanism for abnormal neuronal connectivity and functionality contributing to impaired cognitive functions.

Collectively, the SNO method in the present study delivers a significant advance to brain organoid technologies, and provides a platform for systematic and mechanistic studies to interrogate late-stage embryonic human brain development that is otherwise difficult to address in human fetal tissues or animal models. Laminar structural organization, a hallmark of the adult human cortex, is essential for brain functions and its dysregulation is implicated in various brain disorders. The formation of distinct cortical layers and recapitulation of cortical neuron fate specification in our organoid system opens new avenues for the investigation of neuronal organization and circuitry formation during normal and disease-related human brain development

6 - Conclusions and perspectives

Tremendous breakthroughs have been made in brain organoid technologies in the past few years. While these brain organoids faithfully recapitulate a number of key features of the human brain, they are not perfect replica, and overcoming current limitations to engineer "better" organoids will greatly expand our ability to investigate human brain development and disorders. The definition of "better" organoids may vary based on specific applications, but the benchmark is to make organoids that more faithfully recapitulate features of the human brain. Therefore, continued systematic characterization of human fetal and postnatal brain tissue is fundamental. Despite the difficulty in collecting human brain samples with consistent quality, analyses of these samples have continued to expand our knowledge of normal and diseased human brains (Calvet et al., 2016; Hansen et al., 2010; Moore et al., 2017; Nowakowski et al., 2016; Ozair et al., 2018; Pollen et al., 2015; Stoner et al., 2014). Remarkably, large-scale single-cell transcriptome profiling has resulted in unprecedented resolution revealing the extent of cellular diversity and molecular identities of the embryonic human brain (Nowakowski et al., 2017; Zhong et al., 2018). Pioneered by The Allen Institute for Brain Science, the eventual establishment of a comprehensive human brain atlas containing immunohistology, *in situ* hybridization, and transcriptomics data will provide an invaluable resource for organoid engineers (Ding et al., 2017).

The fact that brain organoids dynamically mimic the temporal progression of human brain development is both an advantage and disadvantage for researchers. On the one hand, brain organoids of different ages recapitulate their corresponding *in vivo* embryogenesis periods, offering researchers a versatile platform to probe different developmental stages. On the other hand, from a practical point of view, brain organoids take a long time to grow and mature, raising the cost and hindering the efficiency of experiments. Methods for speeding up the maturation process thus need to be explored. For instance, the use of NOTCH inhibitors is very effective in accelerating neuronal differentiation *in vitro* and could be applied to brain organoids. But this poses a dilemma because such an intervention could interfere with the intrinsic program of neural differentiation, making the resulting organoids no longer representative of their *in vivo* counterparts (Borghese et al., 2010). Furthermore, to faithfully model age-dependent neurodegenerative diseases requires inducing aging in organoids by pharmacological or genetic methods (Studer et al., 2015). One such strategy for inducing aging-related features in human iPSC-derived organoids, used to model PD, involves the expression of progerin, a truncated form of Lamin A associated with premature aging (Miller et al., 2013). Telomere shortening induced via downregulation of telomerase has also been shown to result in age-related and disease-relevant phenotypes in human iPSC-derived neurons (Vera et al., 2016). However, whether these "induced" aging events accurately reflect the aging process that occurs naturally *in vivo* remains to be determined.

The introduction of fused organoids or "assembloid" systems opens a path to a modular design approach to investigate inter-brain-region and inter-organ crosstalk. Assembly of cortical organoids and organoids with subcortical identities, such as the thalamus, may offer insights into the development of corticofugal projections of deep layer cortical neurons (Pasca, 2018). More complex assembloid systems composed of three or more brain regions are feasible, and the ultimate goal is the assembly of a whole-brain organoid for comprehensive modeling of brain development and function. The combination of organoids from different tissue types could also capture the interface between the nervous system and other organs. Such is the case for the recently reported hPSC-derived intestinal organoids containing neural crest cells, which self-organize to resemble the enteric nervous system and produce rhythmic waves to regulate contraction of the organoids (Workman et al., 2017). Moreover, oncogene manipulation using CRISPR/Cas9 can be applied to initiate tumorigenesis in human brain organoids as an innovative approach to model brain tumors (Bian et al., 2018; Ogawa et al., 2018). Alternatively, brain tumor organoids can be generated from primary glioblastoma specimens from patients that are dissected into smaller pieces and cultured in 3D environment (Hubert et al., 2016). The subsequent fusion of these tumor organoids with normal brain organoids may create a scalable *in vitro* model for cancer metastasis, giving the means to screen for therapies that specifically block cancer cells' invasion into surrounding tissue.

Lastly, it should be noted that organoid differentiation protocols that rely on the self-organization of hPSCs, and stochasticity in their spontaneous differentiation, lead to inherently variable outcomes. Therefore, unlike organs that arise from the precisely controlled process of *in vivo* organogenesis, no two organoids are identical. To improve the quality control, variables in the system should be eliminated wherever possible (Jabaudon and Lancaster, 2018). Feeder-dependent hPSC cultures are more technique-dependent, and the properties of each hPSC line are sometimes inconsistent. A shift to using feeder-free hPSC culture is likely to significantly improve the reproducibility across laboratories and cell lines (Lancaster et al., 2017; Nakagawa et al., 2014; Yoon et al., 2019). The use of variable ingredients, such as animal-derived ECM (Matrigel), in culture protocols should also be minimized, and recombinant growth factors should be replaced by small molecules whenever applicable (Cruz-Acuna et al., 2017; Gjorevski et al., 2016). Furthermore, newly developed organoid generation methods need to be quantitatively characterized to show consistent results with multiple cell lines and independent batches before they are ready for publication. The development of a miniaturized multi-well spinning bioreactor has enabled efficient optimization of organoid protocols and scalable organoid production (Qian et al., 2016), but current methods for organoid characterization are labor-intensive and prevent scaling-up of organoid experiments. Moving forward, the development of systems with automated read-outs for high-throughput analyses will be instrumental to transform organoid models into high-throughput platforms suitable for compound screening and drug discovery.

Together, the rapid advances in brain organoid technologies have opened up new avenues for gaining a better understanding of human brain development, function, evolution and disorders. The brain organoid field has made exciting steps to empower researchers with new tools to address questions that are difficult to address in other model systems, but there remains a long way to go towards obtaining a more faithful *in vitro* representation of the developing human brain. It is important to keep in mind that no model is perfect. Only through synergy across different model systems can we truly gain knowledge that will light the path to overcoming neurological diseases.

References

Abu-Khalil, A., Fu, L., Grove, E.A., Zecevic, N., and Geschwind, D.H. (2004). Wnt genes define distinct boundaries in the developing human brain: implications for human forebrain patterning. J Comp Neurol *474*, 276-288.

Alsio, J.M., Tarchini, B., Cayouette, M., and Livesey, F.J. (2013). Ikaros promotes early-born neuronal fates in the cerebral cortex. Proc Natl Acad Sci U S A *110*, E716-725.

Amiri, A., Coppola, G., Scuderi, S., Wu, F., Roychowdhury, T., Liu, F., Pochareddy, S., Shin, Y., Safi, A., Song, L.*, et al.* (2018). Transcriptome and epigenome landscape of human cortical development modeled in organoids. Science *362*.

Bae, B.I., and Walsh, C.A. (2013). Neuroscience. What are mini-brains? Science *342*, 200-201.

Bardy, C., van den Hurk, M., Eames, T., Marchand, C., Hernandez, R.V., Kellogg, M., Gorris, M., Galet, B., Palomares, V., Brown, J.*, et al.* (2015). Neuronal medium that supports basic synaptic functions and activity of human neurons in vitro. Proc Natl Acad Sci U S A *112*, E2725-2734.

Ben-Ari, Y., and Spitzer, N.C. (2004). Nature and nurture in brain development. Trends Neurosci *27*, 361.

Bershteyn, M., and Kriegstein, A.R. (2013). Cerebral organoids in a dish: progress and prospects. Cell *155*, 19-20.

Bershteyn, M., Nowakowski, T.J., Pollen, A.A., Di Lullo, E., Nene, A., Wynshaw-Boris, A., and Kriegstein, A.R. (2017). Human iPSC-Derived Cerebral Organoids Model Cellular Features of Lissencephaly and Reveal Prolonged Mitosis of Outer Radial Glia. Cell Stem Cell *20*, 435-449 e434.

Birey, F., Andersen, J., Makinson, C.D., Islam, S., Wei, W., Huber, N., Fan, H.C., Metzler, K.R.C., Panagiotakos, G., Thom, N.*, et al.* (2017). Assembly of functionally integrated human forebrain spheroids. Nature *545*, 54-59.

Blackshaw, S., Scholpp, S., Placzek, M., Ingraham, H., Simerly, R., and Shimogori, T. (2010). Molecular pathways controlling development of thalamus and hypothalamus: from neural specification to circuit formation. J Neurosci *30*, 14925-14930.

Brandon, N.J., and Sawa, A. (2011). Linking neurodevelopmental and synaptic theories of mental illness through DISC1. Nat Rev Neurosci *12*, 707-722.

Britanova, O., de Juan Romero, C., Cheung, A., Kwan, K.Y., Schwark, M., Gyorgy, A., Vogel, T., Akopov, S., Mitkovski, M., Agoston, D.*, et al.* (2008). Satb2 is a postmitotic determinant for upper-layer neuron specification in the neocortex. Neuron *57*, 378-392.

Butler, A., Hoffman, P., Smibert, P., Papalexi, E., and Satija, R. (2018). Integrating single-cell transcriptomic data across different conditions, technologies, and species. Nat Biotechnol *36*, 411-420.

Byerly, M.S., and Blackshaw, S. (2009). Vertebrate retina and hypothalamus development. Wiley Interdiscip Rev Syst Biol Med *1*, 380-389.

Bystron, I., Blakemore, C., and Rakic, P. (2008a). Development of the human cerebral cortex: Boulder Committee revisited. Nature reviewsNeuroscience *9*, 110-122.

Bystron, I., Blakemore, C., and Rakic, P. (2008b). Development of the human cerebral cortex: Boulder Committee revisited. Nat Rev Neurosci *9*, 110-122.

Calvet, G., Aguiar, R.S., Melo, A.S., Sampaio, S.A., de Filippis, I., Fabri, A., Araujo, E.S., de Sequeira, P.C., de Mendonca, M.C., de Oliveira, L.*, et al.* (2016). Detection and sequencing of Zika virus from amniotic fluid of fetuses with microcephaly in Brazil: a case study. Lancet Infect Dis.

Cauchemez, S., Besnard, M., Bompard, P., Dub, T., Guillemette-Artur, P., Eyrolle-Guignot, D., Salje, H., Van Kerkhove, M.D., Abadie, V., Garel, C.*, et al.* (2016). Association between Zika virus and microcephaly in French Polynesia, 2013-15: a retrospective study. Lancet.

CDC (2016). Zika virus (Atlanta, GA: US Department of Health and Human Services, CDC).

Chambers, S.M., Fasano, C.A., Papapetrou, E.P., Tomishima, M., Sadelain, M., and Studer, L. (2009). Highly efficient neural conversion of human ES and iPS cells by dual inhibition of SMAD signaling. Nature biotechnology *27*, 275-280.

Chambers, S.M., Tchieu, J., and Studer, L. (2013). Build-a-brain. Cell Stem Cell *13*, 377-378.

Chiang, C.H., Su, Y., Wen, Z., Yoritomo, N., Ross, C.A., Margolis, R.L., Song, H., and Ming, G.L. (2011). Integration-free induced pluripotent stem cells derived from schizophrenia patients with a DISC1 mutation. Mol Psychiatry *16*, 358-360.

Chung, S., Hedlund, E., Hwang, M., Kim, D.W., Shin, B.S., Hwang, D.Y., Kang, U.J., Isacson, O., and Kim, K.S. (2005). The homeodomain transcription factor Pitx3 facilitates differentiation of mouse embryonic stem cells into AHD2-expressing dopaminergic neurons. Molecular and cellular neurosciences *28*, 241-252.

Cugola, F.R., Fernandes, I.R., Russo, F.B., Freitas, B.C., Dias, J.L., Guimaraes, K.P., Benazzato, C., Almeida, N., Pignatari, G.C., Romero, S.*, et al.* (2016). The Brazilian Zika virus strain causes birth defects in experimental models. Nature *534*, 267-271.

Dale, J.K., Vesque, C., Lints, T.J., Sampath, T.K., Furley, A., Dodd, J., and Placzek, M. (1997). Cooperation of BMP7 and SHH in the induction of forebrain ventral midline cells by prechordal mesoderm. Cell *90*, 257-269.

Danjo, T., Eiraku, M., Muguruma, K., Watanabe, K., Kawada, M., Yanagawa, Y., Rubenstein, J.L., and Sasai, Y. (2011). Subregional specification of embryonic stem cell-derived ventral telencephalic tissues by timed and combinatory treatment with extrinsic signals. J Neurosci *31*, 1919-1933.

Dehay, C., Kennedy, H., and Kosik, K.S. (2015). The outer subventricular zone and primate-specific cortical complexification. Neuron *85*, 683-694.

Driggers, R.W., Ho, C.Y., Korhonen, E.M., Kuivanen, S., Jaaskelainen, A.J., Smura, T., Rosenberg, A., Hill, D.A., DeBiasi, R.L., Vezina, G.*, et al.* (2016). Zika Virus Infection with Prolonged Maternal Viremia and Fetal Brain Abnormalities. N Engl J Med.

Fame, R.M., MacDonald, J.L., and Macklis, J.D. (2011). Development, specification, and diversity of callosal projection neurons. Trends Neurosci *34*, 41-50.

Fan, X., Dong, J., Zhong, S., Wei, Y., Wu, Q., Yan, L., Yong, J., Sun, L., Wang, X., Zhao, Y.*, et al.* (2018). Spatial transcriptomic survey of human embryonic cerebral cortex by single-cell RNA-seq analysis. Cell Res *28*, 730-745.

Faria, N.R., Azevedo, R.D., Kraemer, M.U., Souza, R., Cunha, M.S., Hill, S.C., Theze, J., Bonsall, M.B., Bowden, T.A., Rissanen, I.*, et al.* (2016). Zika virus in the Americas: Early epidemiological and genetic findings. Science.

Fjell, A.M., Grydeland, H., Krogsrud, S.K., Amlien, I., Rohani, D.A., Ferschmann, L., Storsve, A.B., Tamnes, C.K., Sala-Llonch, R., Due-Tonnessen, P.*, et al.* (2015). Development and aging of cortical thickness correspond to genetic organization patterns. Proc Natl Acad Sci U S A *112*, 15462-15467.

Ganguly, K., Schinder, A.F., Wong, S.T., and Poo, M. (2001). GABA itself promotes the developmental switch of neuronal GABAergic responses from excitation to inhibition. Cell *105*, 521-532.

Giandomenico, S.L., Mierau, S.B., Gibbons, G.M., Wenger, L.M.D., Masullo, L., Sit, T., Sutcliffe, M., Boulanger, J., Tripodi, M., Derivery, E.*, et al.* (2019). Cerebral organoids at the air-liquid interface generate diverse nerve tracts with functional output. Nat Neurosci *22*, 669-679.

Goodwin, T.J., Schroeder, W.F., Wolf, D.A., and Moyer, M.P. (1993). Rotating-wall vessel coculture of small intestine as a prelude to tissue modeling: aspects of simulated microgravity. Proc Soc Exp Biol Med *202*, 181-192.

Greig, L.C., Woodworth, M.B., Galazo, M.J., Padmanabhan, H., and Macklis, J.D. (2013). Molecular logic of neocortical projection neuron specification, development and diversity. Nature reviewsNeuroscience *14*, 755-769.

Hansen, D.V., Lui, J.H., Parker, P.R., and Kriegstein, A.R. (2010). Neurogenic radial glia in the outer subventricular zone of human neocortex. Nature *464*, 554-561.

Hawrylycz, M.J., Lein, E.S., Guillozet-Bongaarts, A.L., Shen, E.H., Ng, L., Miller, J.A., van de Lagemaat, L.N., Smith, K.A., Ebbert, A., Riley, Z.L.*, et al.* (2012). An anatomically comprehensive atlas of the adult human brain transcriptome. Nature *489*, 391-399.

Heukelbach, J., Alencar, C.H., Kelvin, A.A., De Oliveira, W.K., and Pamplona de Goes Cavalcanti, L. (2016). Zika virus outbreak in Brazil. J Infect Dev Ctries *10*, 116-120.

Hevner, R.F. (2007). Layer-specific markers as probes for neuron type identity in human neocortex and malformations of cortical development. J Neuropathol Exp Neurol *66*, 101-109.

Heymann, D.L., Hodgson, A., Sall, A.A., Freedman, D.O., Staples, J.E., Althabe, F., Baruah, K., Mahmud, G., Kandun, N., Vasconcelos, P.F.*, et al.* (2016). Zika virus and microcephaly: why is this situation a PHEIC? Lancet.

Hodge, R.D., Bakken, T.E., Miller, J.A., Smith, K.A., Barkan, E.R., Graybuck, L.T., Close, J.L., Long, B., Johansen, N., Penn, O.*, et al.* (2019). Conserved cell types with divergent features in human versus mouse cortex. Nature *573*, 61-68.

Huang da, W., Sherman, B.T., and Lempicki, R.A. (2009). Systematic and integrative analysis of large gene lists using DAVID bioinformatics resources. Nat Protoc *4*, 44-57.

Inoue, M., Kuroda, T., Honda, A., Komabayashi-Suzuki, M., Komai, T., Shinkai, Y., and Mizutani, K. (2014). Prdm8 regulates the morphological transition at multipolar phase during neocortical development. PLoS One *9*, e86356.

Ip, B.K., Bayatti, N., Howard, N.J., Lindsay, S., and Clowry, G.J. (2011). The corticofugal neuron-associated genes ROBO1, SRGAP1, and CTIP2 exhibit an anterior to posterior gradient of expression in early fetal human neocortex development. Cereb Cortex *21*, 1395-1407.

Jaffe, A.E., Shin, J., Collado-Torres, L., Leek, J.T., Tao, R., Li, C., Gao, Y., Jia, Y., Maher, B.J., Hyde, T.M., *et al.* (2015). Developmental regulation of human cortex transcription and its clinical relevance at single base resolution. Nat Neurosci *18*, 154-161.

Jakovcevski, I., Mayer, N., and Zecevic, N. (2011). Multiple origins of human neocortical interneurons are supported by distinct expression of transcription factors. Cereb Cortex *21*, 1771-1782.

Jessup, J.M., Goodwin, T.J., and Spaulding, G. (1993). Prospects for use of microgravity-based bioreactors to study three-dimensional host-tumor interactions in human neoplasia. J Cell Biochem *51*, 290-300.

Jo, J., Xiao, Y., Sun, A.X., Cukuroglu, E., Tran, H.D., Goke, J., Tan, Z.Y., Saw, T.Y., Tan, C.P., Lokman, H., *et al.* (2016). Midbrain-like Organoids from Human Pluripotent Stem Cells Contain Functional Dopaminergic and Neuromelanin-Producing Neurons. Cell Stem Cell *19*, 248-257.

Kadir, S.N., Goodman, D.F., and Harris, K.D. (2014). High-dimensional cluster analysis with the masked EM algorithm. Neural Comput *26*, 2379-2394.

Kadoshima, T., Sakaguchi, H., Nakano, T., Soen, M., Ando, S., Eiraku, M., and Sasai, Y. (2013a). Self-organization of axial polarity, inside-out layer pattern, and species-specific progenitor dynamics in human ES cell-derived neocortex. Proc Natl Acad Sci U S A *110*, 20284-20289.

Kadoshima, T., Sakaguchi, H., Nakano, T., Soen, M., Ando, S., Eiraku, M., and Sasai, Y. (2013b). Self-organization of axial polarity, inside-out layer pattern, and species-specific progenitor dynamics in human ES cell-derived neocortex. Proceedings of the National Academy of Sciences of the United States of America *110*, 20284-20289.

Kana, R.K., Libero, L.E., and Moore, M.S. (2011). Disrupted cortical connectivity theory as an explanatory model for autism spectrum disorders. Phys Life Rev *8*, 410-437.

Kelava, I., and Lancaster, M.A. (2016). Stem Cell Models of Human Brain Development. Cell Stem Cell *18*, 736-748.

Kinch, C.D., Ibhazehiebo, K., Jeong, J.H., Habibi, H.R., and Kurrasch, D.M. (2015). Low-dose exposure to bisphenol A and replacement bisphenol S induces precocious hypothalamic neurogenesis in embryonic zebrafish. Proceedings of the National Academy of Sciences of the United States of America *112*, 1475-1480.

Komai, T., Iwanari, H., Mochizuki, Y., Hamakubo, T., and Shinkai, Y. (2009). Expression of the mouse PR domain protein Prdm8 in the developing central nervous system. Gene Expr Patterns *9*, 503-514.

Kriks, S., Shim, J.W., Piao, J., Ganat, Y.M., Wakeman, D.R., Xie, Z., Carrillo-Reid, L., Auyeung, G., Antonacci, C., Buch, A.*, et al.* (2011). Dopamine neurons derived from human ES cells efficiently engraft in animal models of Parkinson's disease. Nature *480*, 547-551.

Kundakovic, M., Gudsnuk, K., Franks, B., Madrid, J., Miller, R.L., Perera, F.P., and Champagne, F.A. (2013). Sex-specific epigenetic disruption and behavioral changes following low-dose in utero bisphenol A exposure. Proceedings of the National Academy of Sciences of the United States of America *110*, 9956-9961.

Lake, B.B., Ai, R., Kaeser, G.E., Salathia, N.S., Yung, Y.C., Liu, R., Wildberg, A., Gao, D., Fung, H.L., Chen, S.*, et al.* (2016). Neuronal subtypes and diversity revealed by single-nucleus RNA sequencing of the human brain. Science *352*, 1586-1590.

Lancaster, M.A., Corsini, N.S., Wolfinger, S., Gustafson, E.H., Phillips, A.W., Burkard, T.R., Otani, T., Livesey, F.J., and Knoblich, J.A. (2017). Guided self-organization and cortical plate formation in human brain organoids. Nat Biotechnol *35*, 659-666.

Lancaster, M.A., and Knoblich, J.A. (2014a). Generation of cerebral organoids from human pluripotent stem cells. Nat Protoc *9*, 2329-2340.

Lancaster, M.A., and Knoblich, J.A. (2014b). Organogenesis in a dish: modeling development and disease using organoid technologies. Science *345*, 1247125.

Lancaster, M.A., and Knoblich, J.A. (2014c). Organogenesis in a dish: modeling development and disease using organoid technologies. Science (New York, NY) *345*, 1247125.

Lancaster, M.A., Renner, M., Martin, C.A., Wenzel, D., Bicknell, L.S., Hurles, M.E., Homfray, T., Penninger, J.M., Jackson, A.P., and Knoblich, J.A. (2013). Cerebral organoids model human brain development and microcephaly. Nature *501*, 373-379.

Lee, J.E., Wu, S.F., Goering, L.M., and Dorsky, R.I. (2006). Canonical Wnt signaling through Lef1 is required for hypothalamic neurogenesis. Development *133*, 4451-4461.

Liu, H., and Zhang, S.C. (2011). Specification of neuronal and glial subtypes from human pluripotent stem cells. Cell Mol Life Sci *68*, 3995-4008.

Long, K.R., Newland, B., Florio, M., Kalebic, N., Langen, B., Kolterer, A., Wimberger, P., and Huttner, W.B. (2018). Extracellular Matrix Components HAPLN1, Lumican, and Collagen I Cause Hyaluronic Acid-Dependent Folding of the Developing Human Neocortex. Neuron *99*, 702-719 e706.

Lu, F., Kar, D., Gruenig, N., Zhang, Z.W., Cousins, N., Rodgers, H.M., Swindell, E.C., Jamrich, M., Schuurmans, C., Mathers, P.H., *et al.* (2013). Rax is a selector gene for mediobasal hypothalamic cell types. J Neurosci *33*, 259-272.

Lui, J.H., Hansen, D.V., and Kriegstein, A.R. (2011). Development and evolution of the human neocortex. Cell *146*, 18-36.

Macosko, E.Z., Basu, A., Satija, R., Nemesh, J., Shekhar, K., Goldman, M., Tirosh, I., Bialas, A.R., Kamitaki, N., Martersteck, E.M., *et al.* (2015). Highly Parallel Genome-wide Expression Profiling of Individual Cells Using Nanoliter Droplets. Cell *161*, 1202-1214.

Malik, S., Vinukonda, G., Vose, L.R., Diamond, D., Bhimavarapu, B.B., Hu, F., Zia, M.T., Hevner, R., Zecevic, N., and Ballabh, P. (2013). Neurogenesis continues in the third trimester of pregnancy and is suppressed by premature birth. J Neurosci *33*, 411-423.

Mao, Y., Ge, X., Frank, C.L., Madison, J.M., Koehler, A.N., Doud, M.K., Tassa, C., Berry, E.M., Soda, T., Singh, K.K., *et al.* (2009). Disrupted in schizophrenia 1 regulates neuronal progenitor proliferation via modulation of GSK3beta/beta-catenin signaling. Cell *136*, 1017-1031.

Mariani, J., Coppola, G., Zhang, P., Abyzov, A., Provini, L., Tomasini, L., Amenduni, M., Szekely, A., Palejev, D., Wilson, M., *et al.* (2015). FOXG1-Dependent Dysregulation of GABA/Glutamate Neuron Differentiation in Autism Spectrum Disorders. Cell *162*, 375-390.

Marin-Padilla, M. (1992). Ontogenesis of the pyramidal cell of the mammalian neocortex and developmental cytoarchitectonics: a unifying theory. J Comp Neurol *321*, 223-240.

Mathisen, G.H., Yazdani, M., Rakkestad, K.E., Aden, P.K., Bodin, J., Samuelsen, M., Nygaard, U.C., Goverud, I.L., Gaarder, M., Loberg, E.M., *et al.* (2013). Prenatal exposure to bisphenol A interferes with the development of cerebellar granule neurons in mice and chicken. International journal of developmental neuroscience : the official journal of the International Society for Developmental Neuroscience *31*, 762-769.

Merkle, F.T., Maroof, A., Wataya, T., Sasai, Y., Studer, L., Eggan, K., and Schier, A.F. (2015). Generation of neuropeptidergic hypothalamic neurons from human pluripotent stem cells. Development *142*, 633-643.

Miller, J.A., Ding, S.L., Sunkin, S.M., Smith, K.A., Ng, L., Szafer, A., Ebbert, A., Riley, Z.L., Royall, J.J., Aiona, K., *et al.* (2014). Transcriptional landscape of the prenatal human brain. Nature *508*, 199-206.

Mlakar, J., Korva, M., Tul, N., Popovic, M., Poljsak-Prijatelj, M., Mraz, J., Kolenc, M., Resman Rus, K., Vesnaver Vipotnik, T., Fabjan Vodusek, V.*, et al.* (2016a). Zika Virus Associated with Microcephaly. N Engl J Med *374*, 951-958.

Mlakar, J., Korva, M., Tul, N., Popovic, M., Poljsak-Prijatelj, M., Mraz, J., Kolenc, M., Resman Rus, K., Vesnaver Vipotnik, T., Fabjan Vodusek, V.*, et al.* (2016b). Zika Virus Associated with Microcephaly. N Engl J Med.

Molyneaux, B.J., Arlotta, P., Menezes, J.R., and Macklis, J.D. (2007). Neuronal subtype specification in the cerebral cortex. Nat Rev Neurosci *8*, 427-437.

Muguruma, K., Nishiyama, A., Kawakami, H., Hashimoto, K., and Sasai, Y. (2015). Self-organization of polarized cerebellar tissue in 3D culture of human pluripotent stem cells. Cell Rep *10*, 537-550.

Nakagawa, Y., and O'Leary, D.D. (2003). Dynamic patterned expression of orphan nuclear receptor genes RORalpha and RORbeta in developing mouse forebrain. Dev Neurosci *25*, 234-244.

Nowakowski, T.J., Bhaduri, A., Pollen, A.A., Alvarado, B., Mostajo-Radji, M.A., Di Lullo, E., Haeussler, M., Sandoval-Espinosa, C., Liu, S.J., Velmeshev, D.*, et al.* (2017). Spatiotemporal gene expression trajectories reveal developmental hierarchies of the human cortex. Science *358*, 1318-1323.

Oberheim, N.A., Takano, T., Han, X., He, W., Lin, J.H., Wang, F., Xu, Q., Wyatt, J.D., Pilcher, W., Ojemann, J.G.*, et al.* (2009). Uniquely hominid features of adult human astrocytes. J Neurosci *29*, 3276-3287.

Owens, D.F., and Kriegstein, A.R. (2002). Is there more to GABA than synaptic inhibition? Nat Rev Neurosci *3*, 715-727.

Ozair, M.Z., Kirst, C., van den Berg, B.L., Ruzo, A., Rito, T., and Brivanlou, A.H. (2018). hPSC Modeling Reveals that Fate Selection of Cortical Deep Projection Neurons Occurs in the Subplate. Cell Stem Cell *23*, 60-73 e66.

Pasca, A.M., Sloan, S.A., Clarke, L.E., Tian, Y., Makinson, C.D., Huber, N., Kim, C.H., Park, J.Y., O'Rourke, N.A., Nguyen, K.D.*, et al.* (2015). Functional cortical neurons and astrocytes from human pluripotent stem cells in 3D culture. Nat Methods *12*, 671-678.

Pasca, S.P. (2018). The rise of three-dimensional human brain cultures. Nature *553*, 437-445.

Petanjek, Z., Berger, B., and Esclapez, M. (2009). Origins of cortical GABAergic neurons in the cynomolgus monkey. Cereb Cortex *19*, 249-262.

Petros, T.J., Tyson, J.A., and Anderson, S.A. (2011). Pluripotent stem cells for the study of CNS development. Front Mol Neurosci *4*, 30.

Pollen, A.A., Nowakowski, T.J., Chen, J., Retallack, H., Sandoval-Espinosa, C., Nicholas, C.R., Shuga, J., Liu, S.J., Oldham, M.C., Diaz, A.*, et al.* (2015). Molecular Identity of Human Outer Radial Glia during Cortical Development. Cell *163*, 55-67.

Qian, X., Jacob, F., Song, M.M., Nguyen, H.N., Song, H., and Ming, G.L. (2018). Generation of human brain region-specific organoids using a miniaturized spinning bioreactor. Nat Protoc *13*, 565-580.

Qian, X., Nguyen, H.N., Song, M.M., Hadiono, C., Ogden, S.C., Hammack, C., Yao, B., Hamersky, G.R., Jacob, F., Zhong, C.*, et al.* (2016). Brain-Region-Specific Organoids Using Mini-bioreactors for Modeling ZIKV Exposure. Cell *165*, 1238-1254.

Qian, X., Song, H., and Ming, G.L. (2019). Brain organoids: advances, applications and challenges. Development *146*.

Quadrato, G., Nguyen, T., Macosko, E.Z., Sherwood, J.L., Min Yang, S., Berger, D.R., Maria, N., Scholvin, J., Goldman, M., Kinney, J.P.*, et al.* (2017). Cell diversity and network dynamics in photosensitive human brain organoids. Nature *545*, 48-53.

Rakic, P. (2009). Evolution of the neocortex: a perspective from developmental biology. Nat Rev Neurosci *10*, 724-735.

Roost, M.S., van Iperen, L., Ariyurek, Y., Buermans, H.P., Arindrarto, W., Devalla, H.D., Passier, R., Mummery, C.L., Carlotti, F., de Koning, E.J.*, et al.* (2015). KeyGenes, a Tool to Probe Tissue Differentiation Using a Human Fetal Transcriptional Atlas. Stem Cell Reports *4*, 1112-1124.

Rosenberg, A.B., Roco, C.M., Muscat, R.A., Kuchina, A., Sample, P., Yao, Z., Graybuck, L.T., Peeler, D.J., Mukherjee, S., Chen, W.*, et al.* (2018). Single-cell profiling of the developing mouse brain and spinal cord with split-pool barcoding. Science *360*, 176-182.

Sachs, N.A., Sawa, A., Holmes, S.E., Ross, C.A., DeLisi, L.E., and Margolis, R.L. (2005). A frameshift mutation in Disrupted in Schizophrenia 1 in an American family with schizophrenia and schizoaffective disorder. Mol Psychiatry *10*, 758-764.

Saito, T., Hanai, S., Takashima, S., Nakagawa, E., Okazaki, S., Inoue, T., Miyata, R., Hoshino, K., Akashi, T., Sasaki, M.*, et al.* (2011). Neocortical layer formation of human developing brains and lissencephalies: consideration of layer-specific marker expression. Cereb Cortex *21*, 588-596.

Sakaguchi, H., Kadoshima, T., Soen, M., Narii, N., Ishida, Y., Ohgushi, M., Takahashi, J., Eiraku, M., and Sasai, Y. (2015). Generation of functional hippocampal neurons from self-organizing human embryonic stem cell-derived dorsomedial telencephalic tissue. Nat Commun *6*, 8896.

Samuelsen, G.B., Larsen, K.B., Bogdanovic, N., Laursen, H., Graem, N., Larsen, J.F., and Pakkenberg, B. (2003). The changing number of cells in the human fetal Forebrain and its subdivisions: A stereological analysis. Cerebral Cortex *13*, 115-122.

Sasai, Y. (2013). Next-generation regenerative medicine: organogenesis from stem cells in 3D culture. Cell Stem Cell *12*, 520-530.

Sato, T., and Clevers, H. (2013). Growing self-organizing mini-guts from a single intestinal stem cell: mechanism and applications. Science *340*, 1190-1194.

Saurat, N., Andersson, T., Vasistha, N.A., Molnar, Z., and Livesey, F.J. (2013). Dicer is required for neural stem cell multipotency and lineage progression during cerebral cortex development. Neural Dev *8*, 14.

Shepherd, G.M. (2013). Corticostriatal connectivity and its role in disease. Nat Rev Neurosci *14*, 278-291.

Shi, Y., Inoue, H., Wu, J.C., and Yamanaka, S. (2017). Induced pluripotent stem cell technology: a decade of progress. Nat Rev Drug Discov *16*, 115-130.

Shimogori, T., Lee, D.A., Miranda-Angulo, A., Yang, Y., Wang, H., Jiang, L., Yoshida, A.C., Kataoka, A., Mashiko, H., Avetisyan, M.*, et al.* (2010). A genomic atlas of mouse hypothalamic development. Nat Neurosci *13*, 767-775.

Singh, K.K., De Rienzo, G., Drane, L., Mao, Y., Flood, Z., Madison, J., Ferreira, M., Bergen, S., King, C., Sklar, P.*, et al.* (2011). Common DISC1 polymorphisms disrupt Wnt/GSK3beta signaling and brain development. Neuron *72*, 545-558.

Stoner, R., Chow, M.L., Boyle, M.P., Sunkin, S.M., Mouton, P.R., Roy, S., Wynshaw-Boris, A., Colamarino, S.A., Lein, E.S., and Courchesne, E. (2014). Patches of disorganization in the neocortex of children with autism. N Engl J Med *370*, 1209-1219.

Su, Y., Shin, J., Zhong, C., Wang, S., Roychowdhury, P., Lim, J., Kim, D., Ming, G.L., and Song, H. (2017). Neuronal activity modifies the chromatin accessibility landscape in the adult brain. Nat Neurosci *20*, 476-483.

Takahashi, K., Tanabe, K., Ohnuki, M., Narita, M., Ichisaka, T., Tomoda, K., and Yamanaka, S. (2007). Induction of pluripotent stem cells from adult human fibroblasts by defined factors. Cell *131*, 861-872.

Takebe, T., Sekine, K., Enomura, M., Koike, H., Kimura, M., Ogaeri, T., Zhang, R.R., Ueno, Y., Zheng, Y.W., Koike, N.*, et al.* (2013). Vascularized and functional human liver from an iPSC-derived organ bud transplant. Nature *499*, 481-484.

Takebe, T., Zhang, R.R., Koike, H., Kimura, M., Yoshizawa, E., Enomura, M., Koike, N., Sekine, K., and Taniguchi, H. (2014). Generation of a vascularized and functional human liver from an iPSC-derived organ bud transplant. Nat Protoc *9*, 396-409.

Tang, H., Hammack, C., Ogden, S.C., Wen, Z., Qian, X., Li, Y., Yao, B., Shin, J., Zhang, F., Lee, E.M*., et al.* (2016). Zika Virus Infects Human Cortical Neural Progenitors and Attenuates Their Growth. Cell Stem Cell.

Taverna, E., Gotz, M., and Huttner, W.B. (2014). The cell biology of neurogenesis: toward an understanding of the development and evolution of the neocortex. Annu Rev Cell Dev Biol *30*, 465-502.

Telley, L., Agirman, G., Prados, J., Amberg, N., Fievre, S., Oberst, P., Bartolini, G., Vitali, I., Cadilhac, C., Hippenmeyer, S*., et al.* (2019). Temporal patterning of apical progenitors and their daughter neurons in the developing neocortex. Science *364*.

Thomsen, E.R., Mich, J.K., Yao, Z., Hodge, R.D., Doyle, A.M., Jang, S., Shehata, S.I., Nelson, A.M., Shapovalova, N.V., Levi, B.P*., et al.* (2015). Fixed single-cell transcriptomic characterization of human radial glial diversity. Nat Methods.

Ulfig, N., Nickel, J., and Bohl, J. (1998). Monoclonal antibodies SMI 311 and SMI 312 as tools to investigate the maturation of nerve cells and axonal patterns in human fetal brain. Cell Tissue Res *291*, 433-443.

Varia, M.A., Calkins-Adams, D.P., Rinker, L.H., Kennedy, A.S., Novotny, D.B., Fowler, W.C., Jr., and Raleigh, J.A. (1998). Pimonidazole: a novel hypoxia marker for complementary study of tumor hypoxia and cell proliferation in cervical carcinoma. Gynecol Oncol *71*, 270-277.

Ventura, C.V., Maia, M., Bravo-Filho, V., Gois, A.L., and Belfort, R., Jr. (2016). Zika virus in Brazil and macular atrophy in a child with microcephaly. Lancet *387*, 228.

Wang, L., Meece, K., Williams, D.J., Lo, K.A., Zimmer, M., Heinrich, G., Martin Carli, J., Leduc, C.A., Sun, L., Zeltser, L.M*., et al.* (2015). Differentiation of hypothalamic-like neurons from human pluripotent stem cells. J Clin Invest *125*, 796-808.

Wang, W., and Lufkin, T. (2000). The murine Otp homeobox gene plays an essential role in the specification of neuronal cell lineages in the developing hypothalamus. Dev Biol *227*, 432-449.

Watanabe, M., Buth, J.E., Vishlaghi, N., de la Torre-Ubieta, L., Taxidis, J., Khakh, B.S., Coppola, G., Pearson, C.A., Yamauchi, K., Gong, D*., et al.* (2017). Self-Organized Cerebral Organoids with Human-Specific Features Predict Effective Drugs to Combat Zika Virus Infection. Cell Rep *21*, 517-532.

Wataya, T., Ando, S., Muguruma, K., Ikeda, H., Watanabe, K., Eiraku, M., Kawada, M., Takahashi, J., Hashimoto, N., and Sasai, Y. (2008). Minimization of exogenous signals in ES cell culture induces rostral hypothalamic differentiation. Proc Natl Acad Sci U S A *105*, 11796-11801.

Wen, Z., Christian, K.M., Song, H., and Ming, G.L. (2016). Modeling psychiatric disorders with patient-derived iPSCs. Curr Opin Neurobiol *36*, 118-127.

Wen, Z., Nguyen, H.N., Guo, Z., Lalli, M.A., Wang, X., Su, Y., Kim, N.S., Yoon, K.J., Shin, J., Zhang, C.*, et al.* (2014). Synaptic dysregulation in a human iPS cell model of mental disorders. Nature *515*, 414-418.

Yin, X., Mead, B.E., Safaee, H., Langer, R., Karp, J.M., and Levy, O. (2016). Engineering Stem Cell Organoids. Cell Stem Cell *18*, 25-38.

Yoon, K.J., Nguyen, H.N., Ursini, G., Zhang, F., Kim, N.S., Wen, Z., Makri, G., Nauen, D., Shin, J.H., Park, Y.*, et al.* (2014). Modeling a genetic risk for schizophrenia in iPSCs and mice reveals neural stem cell deficits associated with adherens junctions and polarity. Cell Stem Cell *15*, 79-91.

Yu, X., and Zecevic, N. (2011). Dorsal radial glial cells have the potential to generate cortical interneurons in human but not in mouse brain. J Neurosci *31*, 2413-2420.

Zhang, Y., Sloan, S.A., Clarke, L.E., Caneda, C., Plaza, C.A., Blumenthal, P.D., Vogel, H., Steinberg, G.K., Edwards, M.S., Li, G.*, et al.* (2016). Purification and Characterization of Progenitor and Mature Human Astrocytes Reveals Transcriptional and Functional Differences with Mouse. Neuron *89*, 37-53.

Zhong, S., Zhang, S., Fan, X., Wu, Q., Yan, L., Dong, J., Zhang, H., Li, L., Sun, L., Pan, N.*, et al.* (2018). A single-cell RNA-seq survey of the developmental landscape of the human prefrontal cortex. Nature *555*, 524-528.

Zikopoulos, B., and Barbas, H. (2013). Altered neural connectivity in excitatory and inhibitory cortical circuits in autism. Front Hum Neurosci *7*, 609.

Curriculum Vitae

(Last updated: 2019-10-28)

Xuyu Qian

qianxuyu@gmail.com (508)373-3500

Date of Birth: Aug 15, 1992 Place of Birth: Nanjing, China

Perelman School of Medicine, University of Pennsylvania
Clinical Research Building, Suite 105
415 Curie Boulevard, Philadelphia, PA 19104

EDUCATION

2013-present	**Johns Hopkins University, School of Medicine,** Baltimore, MD, USA **Ph.D.** in *Biomedical Engineering*, expected graduation: November 2019 **Advisor: Dr. Hongjun Song**
2010-2013	**Worcester Polytechnic Institute,** Worcester, MA, USA **B.S.** in *Biomedical Engineering*, graduation with High Distinction **GPA: 4.0/4.0**

RESEARCH EXPERIENCE

Graduate Student, Johns Hopkins University (PI: Hongjun Song, PhD)

2014-present

- Developed a system to generate brain region-specific organoid from human pluripotent stem cells using miniaturized multi-well spinning bioreactor, patent application pending.
- Investigated the effects of Zika virus infection in human NPCs and organoids and discovered the first experimental evidence for causality between Zika and neurological birth defects.
- Developed methods to generate cortical organoids with expanded laminar structures and specified cortical layers representative of late fetal development.
- Investigated the developmental mechanisms of psychiatric disorders using patient-derived organoids.
- Resulted in 11 publications, 4 first author (*Cell, Nature Protocols, Development*), 1 co-first author (*Cell Stem Cell*), and one first author publication in review.

PUBLICATIONS

1. Jacob F, Salinas RD, Zhang DY, Nguyen PTT, Schnoll JG, Wong SZH, Thokala R, Sheikh S, Saxena D, Prokop S, Liu DA, **Qian X**, Petrov D, Lucas T, Chen HI, Dorsey JF, Christian KM, Binder ZA, Nasrallah M, Brem S, O'Rourke DM, Ming GL, Song H. A patient-derived glioblastoma organoid model and biobank recapitulates inter- and intra-tumoral heterogeneity. **Cell.** 2020; *In press.*

2. **Qian X**, Song H, Ming GL. Brain organoids: advances, applications and challenges. **Development.** 2019; 146(8). PubMed PMID: 30992274.

3. **Qian X***, Jacob F*, Song MM, Nguyen HN, Song H, Ming GL. Generation of human brain region-specific organoids using a miniaturized spinning bioreactor. **Nat Protoc**. 2018;13(3):565-80. PubMed PMID: 29470464. *Cover image.*

4. Ye F, Kang E, Yu C, **Qian X**, Jacob F, Yu C, Mao M, Poon RYC, Kim J, Song H, Ming GL, Zhang M. DISC1 Regulates Neurogenesis via Modulating Kinetochore Attachment of Ndel1/Nde1 during Mitosis. **Neuron**. 2017;96(5):1041-54 e5. PubMed PMID: 29103808.

5. Yoon KJ, Song G, **Qian X**, Pan J, Xu D, Rho HS, Kim NS, Habela C, Zheng L, Jacob F, Zhang F, Lee EM, Huang WK, Ringeling FR, Vissers C, Li C, Yuan L, Kang K, Kim S, Yeo J, Cheng Y, Liu S, Wen Z, Qin CF, Wu Q, Christian KM, Tang H, Jin P, Xu Z, Qian J, Zhu H, Song H, Ming GL. Zika-Virus-Encoded NS2A Disrupts Mammalian Cortical Neurogenesis by Degrading Adherens Junction Proteins. **Cell Stem Cell**. 2017;21(3):349-58 e6. PubMed PMID: 28826723.

6. **Qian X**, Nguyen HN, Jacob F, Song H, Ming GL. Using brain organoids to understand Zika virus-induced microcephaly. **Development**. 2017;144(6):952-7. PubMed PMID: 28292840.

7. Xu M, Lee EM, Wen Z, Cheng Y, Huang WK, **Qian X**, Tcw J, Kouznetsova J, Ogden SC, Hammack C, Jacob F, Nguyen HN, Itkin M, Hanna C, Shinn P, Allen C, Michael SG, Simeonov A, Huang W, Christian KM, Goate A, Brennand KJ, Huang R, Xia M, Ming GL, Zheng W, Song H, Tang H. Identification of small-molecule inhibitors of Zika virus infection and induced neural cell death via a drug repurposing screen. **Nat Med**. 2016;22(10):1101-7. PubMed PMID: 27571349. *Cover image.*

8. Zhang F, Hammack C, Ogden SC, Cheng Y, Lee EM, Wen Z, **Qian X**, Nguyen HN, Li Y, Yao B, Xu M, Xu T, Chen L, Wang Z, Feng H, Huang WK, Yoon KJ, Shan C, Huang L, Qin Z, Christian KM, Shi PY, Xu M, Xia M, Zheng W, Wu H, Song H, Tang H, Ming GL, Jin P. Molecular signatures associated with ZIKV exposure in human cortical neural progenitors. **Nucleic Acids Res**. 2016;44(18):8610-20. PubMed PMID: 27580721.

9. Nguyen HN, **Qian X**, Song H, Ming GL. Neural stem cells attacked by Zika virus. **Cell Res**. 2016;26(7):753-4. PubMed PMID: 27283801.

10. Schiffhauer ES, Luo T, Mohan K, Srivastava V, **Qian X**, Griffis ER, Iglesias PA, Robinson DN. Mechanoaccumulative Elements of the Mammalian Actin Cytoskeleton. **Curr Biol**. 2016;26(11):1473-9. PubMed PMID: 27185555.

11. **Qian X***, Nguyen HN*, Song MM, Hadiono C, Ogden SC, Hammack C, Yao B, Hamersky GR, Jacob F, Zhong C, Yoon KJ, Jeang W, Lin L, Li Y, Thakor J, Berg DA, Zhang C, Kang E, Chickering M, Nauen D, Ho CY, Wen Z, Christian KM, Shi PY, Maher BJ, Wu H, Jin P, Tang H, Song H, Ming GL. Brain-Region-Specific Organoids Using Mini-bioreactors for Modeling ZIKV Exposure. **Cell**. 2016;165(5):1238-54. PubMed PMID: 27118425.

12. Tang H*, Hammack C*, Ogden SC*, Wen Z*, **Qian X***, Li Y, Yao B, Shin J, Zhang F, Lee EM, Christian KM, Didier RA, Jin P, Song H, Ming GL. Zika Virus Infects Human Cortical Neural Progenitors and Attenuates Their Growth. **Cell Stem Cell**. 2016;18(5):587-90.

PubMed PMID: 26952870 (***co-first authors**). *Cover image.*

PRESENTATIONS

1. **Qian X,** Song H, Ming GL. Sliced Human Cortical Organoids for Modeling Distinct Cortical Neuronal Layer Formation. Oral presentation delivered at New York Stem Cell Foundation Conference, New York, NY, USA, 2019.

2. **Qian X,** Song H, Ming GL. Human Sliced Neocortical Organoids Establish Specified Upper and Deep Cortical Layers. **Poster presentation** delivered at International Society for Stem Cell Research Annual Meeting, San Diego, CA, USA, 2019.

3. **Qian X,** Song H, Ming GL. Modeling Human Brain Development and Disorders Using hiPSC-derived Organoids. **Invited oral presentation** delivered at International Young Scholar’s Forum at Nanjing Medical University, Nanjing, Jiangsu, China, 2018.

4. **Qian X,** Song H, Ming GL. Modeling neurodevelopmental etiology of psychiatric disorders in human forebrain organoids. **Oral presentation** delivered at Society for Neuroscience meeting, San Diego, CA, USA, 2018.

5. **Qian X,** Song H, Ming GL. Engineering Forebrain Organoids to Model Zika Virus-Induced Microcephaly. **Invited lecture delivered** at Tsinghua University McGovern Institute for Brain Research lecture series, Beijing, China, 2016.

6. **Qian X,** Song H, Ming GL. Engineering Forebrain Organoids to Model Zika Virus-Induced Microcephaly. **Invited oral presentation** delivered at “Hot Topics in Stem Cell Biology” Symposium at Society for Neuroscience meeting, San Diego, CA, USA, 2016.

7. **Qian X**, Nguyen HN, Song MM, Ogden SC, Hammack C, Wen Z, Tang H, Song H, Ming GL. Forebrain Organoids Generated Using Mini-bioreactors For Modeling Zika Virus Exposure and Microcephaly. Society for Neuroscience abstract: 8702. **Poster presentation** delivered at Society for Neuroscience meeting, San Diego, CA, USA, 2016.

8. **Qian X**, Nguyen HN, Tang H, Song H, Ming GL. Studying Zika-induced Birth Defects with "Mini-brains". **Oral presentation** delivered at Neuroscience 2016 Press Conference: Zika at Society for Neuroscience meeting, San Diego, CA, USA, 2016.

9. **Qian X**, Gornet M, Song H, Ming GL. Engineering Mini-Brains to Understand Zika Virus-Induced Microcephaly. **Invited lecture** delivered at Johns Hopkins University Partnering Toward Discovery lecture series, Baltimore, MD, USA, 2016.

10. **Qian X**, Nguyen HN, Song MM, Ogden SC, Hammack C, Wen Z, Tang H, Song H, Ming GL. Forebrain Organoids Generated Using Mini-bioreactors For Modeling Zika Virus Exposure and Microcephaly. **Poster presentation** at Maryland Stem Cell Research Symposium, Bethesda, MD, USA 2016.

11. **Qian X**, Ming GL, Song H. Generation of Cerebral Cortex Organoids from Human Induced Pluripotent Stem Cells. **Oral presentation** delivered at Johns Hopkins Neuroscience Department seminar, Baltimore, MD, USA, 2016.

12. **Qian X**, Yamajala P, Ambady S, Wen Q. Real-time Analysis of Cell Traction Force in vitro on Deformable Hydrogels. **Poster presentation** at Annual Northeast Bioengineering Conference, Syracuse, NY, USA, 2013.

PATENTS

Song H, Ming G, Song MM, Hadiono C, Jeang W, Nguyen NH, Qian X. Cell culture system and method of use thereof. U.S. Patent Application US20180334646A1, filed November 2016. Patent Pending.

TEACHING EXPERIENCE

Johns Hopkins University, Department of Biomedical Engineering

Teaching assistant, Cellular Engineering, 2016.

Teaching assistant, Molecules and Cells, 2016.

HONORS AND AWARDS

2010-2013	Presidential Scholarship, Worcester Polytechnic Institute
2010-2013	International Scholarship, Worcester Polytechnic Institute
2011	Charles O. Thompson Scholar Award (5%), Worcester Polytechnic Institute
2012	Undergraduate Research Fellowship, Worcester Polytechnic Institute
2013	Provost's Major Qualifying Project Award, Worcester Polytechnic Institute
2013	B.S. awarded with high honors (10%), Worcester Polytechnic Institute
2016	National Institute of Neurological Disorders and Stroke Travel Award
2017	Bae Gyo Jung Young Investigator Award, Johns Hopkins University
2019	Chinese National Award for Outstanding Self-Financed Students Abroad, Ministry of Education of the People's Republic of China